Trinity College Dublin

Doctoral Thesis

PhD in Physics

Athermalisation and Characterisation of High-Order Surface Grating Lasers for Optical Communications

Student:
Dovydas Mickus
14313389

Project Supervisor:
Prof. John F. Donegan

June 28, 2023

Trinity College Dublin
Coláiste na Tríonóide, Baile Átha Cliath
The University of Dublin

Declaration of authorship

I, Dovydas Mickus, have read and I understand the plagiarism provisions in the General Regulations of the University Calendar for the current year, found at: http://www.tcd.ie/calendar.

I have completed the Online Tutorial in avoiding plagiarism 'Ready, Steady, Write', located at: http://tcd-ie.libguides.com/plagiarism/ready-steady-write.

Signed :

_____

Date :

_____

Abstract

The semiconductor laser allows for the vast quantities of data that are transmitted over optical fibre each day. A simple device has transformed our lives. This transformation will continue in the coming decade where the rapid growth of high-speed data transmission services is increasing the demand for bandwidth and continual industry innovation is needed to meet this challenge. For the optical access networks, next generation passive optical networks version 2 (NGPON2) is an ambitious ITU standard developed to drive such innovation. Time and wavelength division multiplexing (TWDM) has been chosen for the NGPON2 standard. These NGPON2 transmitters will be used in fibre-to-the-x (FTTx), including fibre-to-the-home (FTTH) systems and hence are to be deployed to every customers premises. Such wide network deployment places an extremely high level of importance on transceiver cost reduction – which can be achieved through the simplification of the manufacturing process. Currently, distributed feedback (DFB) lasers and distributed Bragg reflector (DBR) lasers with buried low order gratings are the focus of TWDM research. However, fabrication of these lasers requires complex regrowth steps and precise e-beam lithography which invariably drives yield down and costs up. Previous research in the Trinity College Dublin semiconductor photonics group has yielded low-cost laser designs based on high-order surfaced etched slots for the devices grating structure, which can forgo regrowth steps and use inexpensive optical lithography. The research presented in this thesis builds upon the work previously performed on these devices.

In addition to low cost requirements, there is a significant reduction of channel spacing, which in turn requires increased wavelength stability of transmitters. This is challenging to achieve since the emission wavelength of lasers is inherently temperature sensitive, and many applications use lasers in a variable high-temperature environment such as in data centres. Similarly, for pumping resonators for broadband comb generation, wavelength stability versus temperature is critical. Currently, thermoelectric coolers (TEC) are used to maintain a stable device temperature however, their energy efficiency

and tuning precision are relatively low. Furthermore, their addition increases packaging costs and reduces package lifetime. Instead, semiconductor lasers can be athermalised, making their lasing wavelength insensitive to changes in ambient temperature by varying injection currents across laser sections, which would allow the removal of the TEC, improving overall energy efficiency, reducing packaging costs and increasing package lifetime. There has been significant athermalisation research stemming from our group and else where, and this work significantly builds upon it. First, extensive characterisation of our existing devices is performed in steady state conditions with the aim of choosing a device which is capable of wide range athermalisation. Results from this yields that 700 μm long devices that have a Bragg peak which is misaligned with the gain peak by approximately +20 to 25 nm yield would yield the best results. The chosen device is then continuously athermalised over a range of 5 to 106 ^{o}C, while maintaining a frequency stability of $\pm$0.4 GHz and SMSR above 30 dB. This athermalisation scheme was then extended to multiples wavelengths from the same device, with thorough analysis of device parameter change over the athermal path versus wavelength. As a natural consequence of these measurements, a new method to measure thermal impedance of all-active active devices has been developed, measuring the thermal impedance length product of our devices as 29.3$\pm$2.1 ^{o}C μm/mW for the gain section and 39.33$\pm$2.8 ^{o}C μm/mW for the grating section.

TWDM transmitters must also be capable of pulsed mode operation, meeting the same requirements mentioned above. This requirement is challenging to meet due to the large, time dependent thermal frequency drift which occurs during pulses which is caused by the laser self-heating. The devices under this research have not been extensively tested under transient conditions and thus pulsed mode characterisation has been performed. It was found that 700 μm devices were best suited for the TWDM standard, due to the lowest exhibited frequency drift (2.5 GHz) within the time-frame of interest. Several schemes for compensating thermal wavelength drift have been proposed in literature, while some were not feasible to test, such as using external heaters, which our devices did not contain, others were tested on our devices. It was found that a sub-threshold heating approach yielded a

6 GHz improvement in overall wavelength drift, across all pulse amplitudes, and as a consequence of some of these tests, a new pulse shaping method was developed. This new pulse-shaping method reduces the settling time of the optical frequency, in some cases by a factor of 3. Then, as the frequency change was expected to be due to thermal effects, we employed transient thermal imaging to get a better understanding of the lasers thermal performance. Our results seem to be relatively inline with wavelength based measurements, further solidifying that a thermal based theory for these devices operation is correct.

Keywords : surface grating, athermalisation, pulsed mode, optical networks.

Acknowledgements

Firstly, and most importantly, I would like to express my utmost thanks to Professor John Donegan for providing me with this wonder opportunity to learn about the world of photonics. His invaluable guidance, constructive advice, ideas and moral support were all readily available and I thank him for this. The supervision style employed allowed for great freedom allowing me to pursue my own research interest, which I have thoroughly enjoyed. I would also like to acknowledge Science Foundation Ireland, without whom this work would not be possible.

I would also like to thank Dr Robert McKenna and Dr Gaurav Jain for their teachings of the lab basics and for their continued support while I write this thesis! A big thank you to Dr Caolan Murphy for his many discussions and feedback on all of the work throughout the PhD, without which this work would have been much more challenging. I would also like to thank Dr Simon Corbett for building the transient CCD-TR setup and spending extensive time training me on it. In addition, I would like to thank all other group members, namely, Michael McDermott and Dr Haizhong Weng for discussion and various engagements during our weekly meetings. Overall, I express my sincerest gratitude to all members of the TCD Semiconductor Photonics Group for their various discussions and just overall fun times!

I would also like to express my gratitude to our collaborators, from whom I garnered significant amounts of expertise. Namely, the optical communications group in Dublin City University run by Professor Liam Barry, who not only provided me with amazing guidance, but also supplied some of the equipment necessary to complete this work. In the same regard, I would also like to thank Dr Colm Browning for his expert advice. Similarly, I would like to thank Pilot Photonics, and in particular Ankit Sharma for his continued assistance.

Then, I would like to thank those who, while not directly associated with the research, it would not been possible. Firstly, my father Arturas Mickus and mother Daiva Mickiene, for providing me with constant support, both financial and moral. Without them continually looking out for me, particularly

during the tough times of the COVID-19 pandemic, this research would have been much more difficult. Secondly, I would like to thank those who while not family, in my eyes have become so, namely, in no particularly order, Gaurav, Devika, Ross, Adam ,Killian, David, Oisin, Brian, Jack, Michael, Carolyn, Jorge, Anais, Eric, Maggie, Daire, Katarzyna, Katja, Simon and Mahshid. I sincerely thank you all for looking out for me and for pushing me on to do my best! Thirdly, I would also like to thank the people in the Westland Row office for putting up with me, i.e. Carolyn, Jack, Oisin, Julia and Stephen,it has been a wild ride, and I hope it continues in the same way!

Contents

List of Publications

1. **D. Mickus**, R. Mckenna, C. Murphy, and J. F. Donegan, "Wide range thermal and athermal operation of slotted surface grating lasers," Optics Express, vol. 29, pp. 16893–16903, May 2021. Publisher: Optica Publishing Group.

2. **D. Mickus**, C. Murphy, R. Mckenna, and J. F. Donegan, "Method to measure thermal impedance for all-active lasers using the athermalisation condition," Optics Continuum, vol. 1, pp. 556–564, Mar. 2022. Publisher: Optica Publishing Group.

3. **D. Mickus**, R. McKenna, C. Murphy, and J. Donegan, "Multi-channel wide range athermal operation of slotted surface grating lasers for athermal DWDM," Optics Continuum, vol. 1, pp. 345–354, Feb. 2022. Publisher: Optica Publishing Group.

4. **D. Mickus**, G. Jain, S. Naimi, R. McKenna, C. Murphy, and J. F. Donegan, "Athermal Operation of Multi-Section Surface Grating Lasers for Applications including Burst-Mode for TWDM-PONs," in Conference on Lasers and Electro-Optics (2020), paper STu4M.1, p. STu4M.1, Optica Publishing Group, May 2020.

5. **D. Mickus**, R. McKenna, and J. F. Donegan, "Large Range Athermalisation of Multi-Section Surface Grating Lasers for DWDM-PONs," in 2021 Conference on Lasers and Electro-Optics (CLEO), pp. 1–2, May 2021. ISSN: 2160-8989.

6. **D. Mickus**, C. Murphy, R. McKenna, and J. Donegan, "A New Method to Measure Thermal Impedance for All-Active Semiconductor Lasers using the Athermalisation Condition," in Conference on Lasers and Electro- Optics (2022), paper JTh3A.35, p. JTh3A.35, Optica Publishing Group, May 2022.

7. R. McKenna, **D. Mickus**, S. Naimi, C. Murphy, M. McDermott, S. Corbett, D. McCloskey, D. McCloskey, D. McCloskey, D. McCloskey,

J. F. Donegan, J. F. Donegan, J. F. Donegan, and J. F. Donegan, "Spatially resolved self-heating and thermal impedance of laser diodes using CCD-TR imaging," OSA Continuum, vol. 4, pp. 1271–1281, Apr. 2021. Publisher: Optica Publishing Group.

8. M. McDermott, R. McKenna, C. Murphy, **D. Mickus**, H.-Z. Weng, S. Naimi, Q. Lu, W.-H. Guo, M. Wallace, N. Abad´ıa, and J. F. Donegan, "1.3 μm wavelength tunable single-mode laser arrays based on slots," Optics Express, vol. 29, pp. 15802–15812, May 2021. Publisher: Optica Publishing Group.

9. R. McKenna, S. Corbett, S. T. Naimi, **D. Mickus**, D. McCloskey, and J. F. Donegan, "Thermoreflectance Imaging of Semiconductor Lasers With a Numerical Thermal Model," IEEE Journal of Selected Topics in Quantum Electronics, vol. 28, pp. 1–6, Jan. 2022. Conference Name: IEEE Journal of Selected Topics in Quantum Electronics.

List of Figures

List of Tables

List of Abbreviations

AR - Anti Reflection

ASE - Amplified Spontaneous Emission

BL - Bitrate Length Product

C-band - Conventional Band

CCD - Charged Coupled Device

DBR- Distributed Bragg Reflector

DFB - Distributed Feedback.

DNC - Date Centre Network

DWDM - Dense Wavelength Division Multiplexing

EDFA - Erbium Doped Fibre Amplifier

FSR - Free Spectral Range

FTTH - Fibre to the home.

FTTx - Fibre to the x.

HR - High Reflection

ICP - Inductively Coupled Plasma

Laser - Light Amplification by Stimulated Emission of Radiation

LED - Light Emitting Diode

Maser - Microwave Amplification by Stimulated Emission of Radiation

MOCVD - Metal Organic Chemical Vapour Deposition

NGPON2 - Next Generation Passive Optical Networks version 2.

O-band - Original Band

ONU - Optical Network Unit

OSA - Optical Spectrum Analyser

PAM - Pulse Amplitude Modulation

PIC - Photonic Integrated Circuit

PON - Passive Optical Network

PSK - Phase Shift Keying

QAM - Quadrature Amplitude Modulation

QW - Quantum Well

Rx - Receiver

SCH-QW - Separate Confinement Heterostructure Quantum Well

SCH-MQW - Separate Confinement Heterostructure Multiple Quantum Well

SDM - Space Division Multiplexing

SMSR - Side Mode Suppression Ratio

SOA - Semiconductor Optical Amplifier

TEC - Thermoelectric Cooler

TDM - Time Division Multiplexing

TI - Thermal Impedance

TR - Thermoreflectance

TWDM - Time and Wavelength Division Multiplexing.

Tx - Transmitter

WDM - Wavelength Division Multiplexing

YAG - Yttrium Aluminium Garnet

Chapter 1

Introduction

1.1 History of Lasers

The journey for coherent light started in late 1900 with Max Planck proposing that black body radiation is quantised, and not part of a continuum [1]. This was a big breakthrough, as it was a significant leap from classical physics, however, arguably an even more important proposition occurred when Albert Einstein postulated that this fact did not apply to just local oscillators but all electromagnetic radiation. This famously resulted in Einstein being able to explain the photoelectric effect [2], where a photon can cause an emission of an electron. Similarly, he predicted that another key interaction can occur, where a photon can induce an atom to release another photon of identical properties, in a process now known as stimulated emission, which forms the basis of laser operation. However, it was not until 1953 that this concept was put into practical use, when Charles Townes developed the first maser (Microwave Amplification by Stimulated Emission of Radiation) [3] which used ammonia as a gain medium to produce microwave radiation. Unbeknownst to Townes, Nicolay Basov and Alexsandr Prokhorov in the USSR had independently made the same discovery, with the trio being awarded the 1964 Nobel Prize in Physics for their findings. As a consequence of their work, the first laser (Light Amplification by Stimulated Emission of Radiation) was then discovered by Theodore Maiman in 1960, using Ruby as a gain

medium, and emitting light at 694.3 nm, just about in the visible regime [4]. Lasers using other gain media, such as He-Ne gas [5], neodymium glass [6] and yttrium aluminium garnet (YAG) [7] were discovered shortly after.

As seen above, the 1960s saw the emergence of many lasers, with many gain media, however, arguably the most important development was the discovery of the semiconductor laser diode in 1962, made independently but almost simultaneously by researchers in IBM and General Electric. The first of these lasers was developed by Robert N. Hall [8]. This laser incorporated a GaAs p-n homo-junction, operating at approximately 840-850 nm, capable of only functioning in pulsed mode operation at $\approx$ 70 K, thus requiring further research to be usable in commercial systems. Room temperature operation was required, and it would not be long until the postulation of the heterostructure in 1963 [9, 10], but it would not be until 1970 that the first double heterostructure semiconductor laser would be built by Alferov [11]. This structure was capable of operating at room temperature, and at relatively low threshold current at the time, resulting in the possibility of CW operation at room temperature. This technology was enabled due to the development of liquid phase epitaxy. Following the double heterostructure, a quantum well laser was postulated by Charles H. Henry in 1972 and was later developed in 1978 by Dupuis et al [12], demonstrating significantly reduced threshold current due to improved carrier confinement when compared to double heterostructure lasers. The manufacturing of these lasers was made possible due to development in metalorganic chemical vapour deposition (MOCVD). Further advancements in the field were made due to increased precision of epitaxial techniques, which in turn resulted in the development of strained quantum well lasers by Alf Adams at the University of Surrey in 1986 [13]. Strained quantum well structures result in a reduction of density of states at the top of the valance band, resulting in significantly lower threshold currents. Additionally, the lattice mismatch results in a changed band-structure, allowing a shift in lasing wavelength which would not be possible with lattice matched materials. Then, due to their flexible emission wavelength, low threshold, electrical tunability and small footprint, semiconductor lasers have become key components in modern optical communication

systems.

1.2 Emergence of Optical Networks and their Evolution

Alongside the development of semiconductor lasers in the 1960s, there were also other developments within the communications networks space, which led to the emergence of optical communications networks. While semiconductor lasers would later be used as the transmitters in these networks, a suitable transmission medium was needed to carry the optical signal. A breakthrough in this aspect came in 1966 with a demonstration of silica optical fibres, which did have large losses (1000 dB/km), however it was also proposed that these losses may be reduced with the reduction of impurities [14]. By 1970, Corning Glassworks Inc had developed optical fibres which had attenuation of 20 dB/km, which were low enough for optical communications purposes.

The combination of efficient transmitters and a suitable transport medium resulted in a boom within the optical communications space, with the first trials of these networks seeing deployment in 1977 by AT&T, at the bitrate of 45 MBit/s operating at 850 nm. The fibre loss for these wavelengths at the time was $\approx$ 3dB/km, requiring signal regeneration every 10 km or so, using electrical repeaters. This was a major breakthrough at the time, as it was far superior to the previously used coaxial technology which required repeaters every 1 km or so, resulting in reduced costs for these networks. Commercial systems began rolling out in 1980, typically operated around 1310 nm wavelength (original or O-band), which benefited from lower chromatic dispersion and fibre loss, and by 1984 the first submarine fibres had been deployed by the British Telecom PLC, requiring a repeater spacing of $\approx$ 50 km.

While the repeater spacing was relatively large and sufficient for short reach networks, it was still very costly to deploy for long-haul networks. In the late 1980s, the development of Erbium doped fibre amplifiers (EDFA) [15, 16] revolutionised optical communication systems, allowing transmission without need for signal regeneration. This was previously a large barrier

for long-haul networks, however as EDFAs operated in the 1530-1565 nm range (conventional or C-band), a shift to this wavelength was required and significant research was put into the development of laser diodes which can operate within this window.

Alongside EDFAs, wavelength division multiplexing (WDM) was developed and significantly boosted capacity per fibre. WDM combines many different wavelengths from many transmitters (Tx) using a multiplexer into one fibre and then separates the different wavelengths at the receiver end (Rx) using a demultiplexer, which drastically increases data throughput per fibre. An example system is shown in figure 1.1.

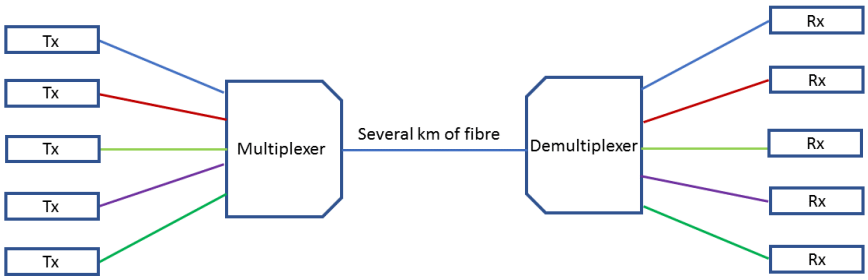

Figure 1.1: Example WDM system.

Modern long haul systems have implemented a variant of this system called Dense Wavelength Division Multiplexing (DWDM), which reduces the channel spacing, increasing spectral efficiency.

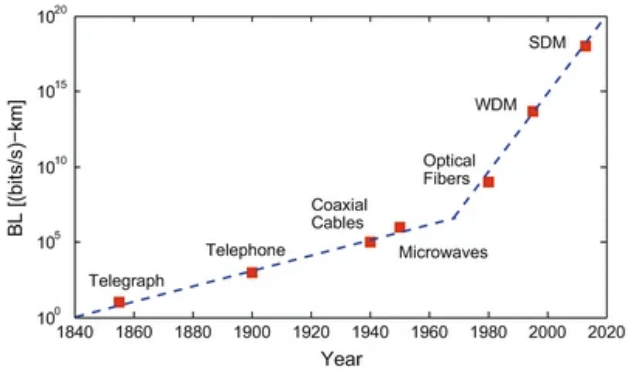

Figure 1.2: Change in BL product since the conception of telecommunications. Notice the large jump with the invention of optical communications. Source : [17]

Another advancement that was made in 2010 is space division multiplexing (SDM) for which the light is spatially separated within multi-core fibres. Commercially deployed systems have demonstrated data rates of up to 100 TB/s [18], which form the basis of our current optical communications systems. The massive growth of telecommunication systems can be illustrated with the bit rate-distance product, BL, where B is the bit rate and L is the repeater spacing. Figure 1.2 shows how this product varied since the conception of data transmission over distances, and the massive jump optical communication networks have induced. A new up and coming system is termed time and wavelength division multiplexing (TWDM), which superimposes a time division multiplex (TDM) grid, onto a WDM grid. TDM uses pulsed mode transmitters (better known as burst mode/BM transmitters) and synchronised delays, so pulses can be timed in such a way as to not interfere but be right next to each other. This allows multiple users to use a single wavelength channel and significantly improves network efficiency. Then, maximum channel/network (through TDM) and spectral efficiency (through WDM) can be achieved. A sample timing diagram for TDM is shown in figure 1.3.

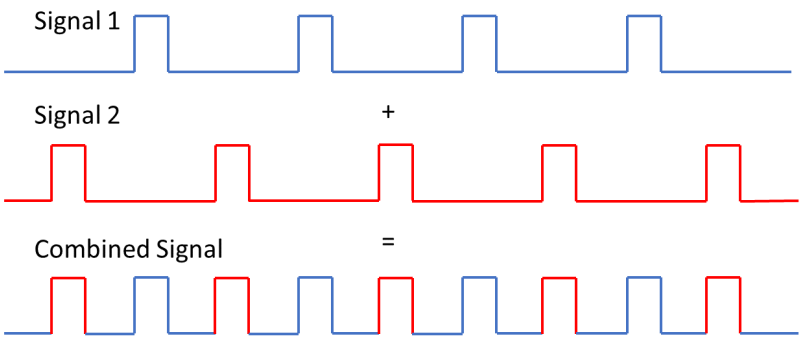

Figure 1.3: Example of TDM synchronised timing for two signals on one wavelength channel.

1.3 Network Architecture

The aforementioned networks, particularly in the modern day, have a rather complex architecture, however for the purposes of this thesis, this architecture can be effectively split into two branches based on their transmission distance, one being short haul networks and the other being long haul networks. An example structure is shown in figure 1.4 [19]. Each of these posing their own challenges, with their descriptions given in the following sections.

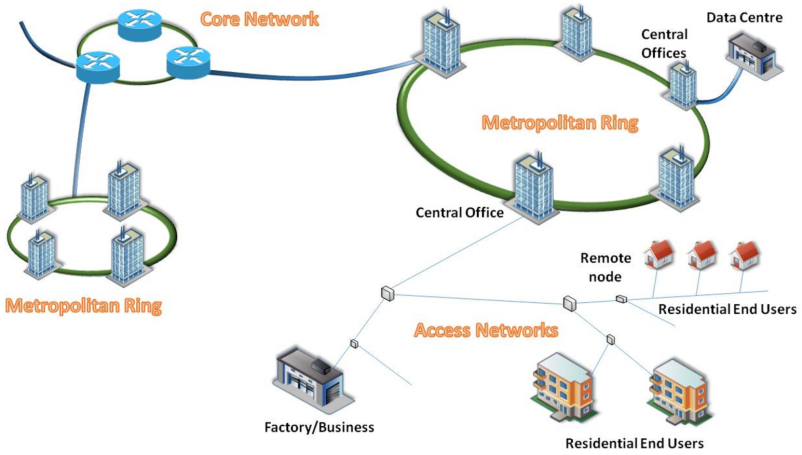

Figure 1.4: Example of Optical Network Architecture. Source : [19]

1.3.1 Long Reach Networks

Long haul networks include the metro and the core, and are the backbone of global optical communication networks. Transmission distances consist of hundreds, if not thousands of kilometres, often times over fibre that's laid down over a submarine link. These systems handle data from millions of users and are expensive to implement, so system robustness is paramount. In particular, transmitter cost and power consumption are not as big of a concern when compared to short-haul networks, with maximisation of spectral efficiency to make optimal use of existing architecture being the focus of current research. Namely, advanced modulation formats are currently being implemented, which are just different ways of encoding more data into a single wavelength channel. Namely, formats using amplitude modulation such

as 4 or 8 level, pulse amplitude modulation (PAM4 or PAM8) [20], and phase based modulation such as Phase-Shift Keying (PSK) and 16-quadrature amplitude modulation (QAM) formats have been the focus of research [21, 22].

1.3.2 Short Reach Networks

Short reach networks include the access networks which connect the end-user to the metro and the core. They typically transmit data on the order of 10s of kilometres. In recent years, short reach networks have undergone a major push to avoid active components in favour of passive components, resulting in passive optical networks (PONs). This primarily constitutes the removal of repeaters or amplifiers from active networks. WDM-PONs are widely implemented to achieve large data throughput, with DWDM-PONs seeing widespread deployment with an even further shrinkage of channel spacing. The reduced channel spacing poses a risk of inter-channel crosstalk, thus, increasingly wavelength stable transmitters are required. Particularly, thermally-induced wavelength drift has become a challenge for these systems. A typically solution has been to deploy transmitters alongside thermoelectric coolers, however these are energy inefficient and limit transmitter package lifetime. The deployment of TWDM requires each costumer to have an optical network unit (ONU) on their premises, and considering that there would be millions/billions of users, transmitter costs become a concern as well.

Another aspect of short reach networks is that of inter-data centre and intra-data centre networks (DNCs), which has seen a major switch to optical networking in recent times to increase capacity. Typically data centres have size constraints, and thus the spatial footprint of optical components becomes a factor. A solution of this is to use monolithic, photonic integrated circuits (PICs), which have a small spatial footprint, however due to tight integration may result in degradation in thermal performance. Thus, considerable effort is being put into PIC research and their thermal management.

1.4 Challenges and Thesis Scope

1.4.1 Challenges

As optical communication systems evolve, consumer demand has also seen a continual growth. This is due to invention of data hungry devices such as personal computers, smartphones, and also due to internet of things services such as online video streaming and gaming. The past growth is shown in figure 1.5, clearly indicating close to exponential growth of users.

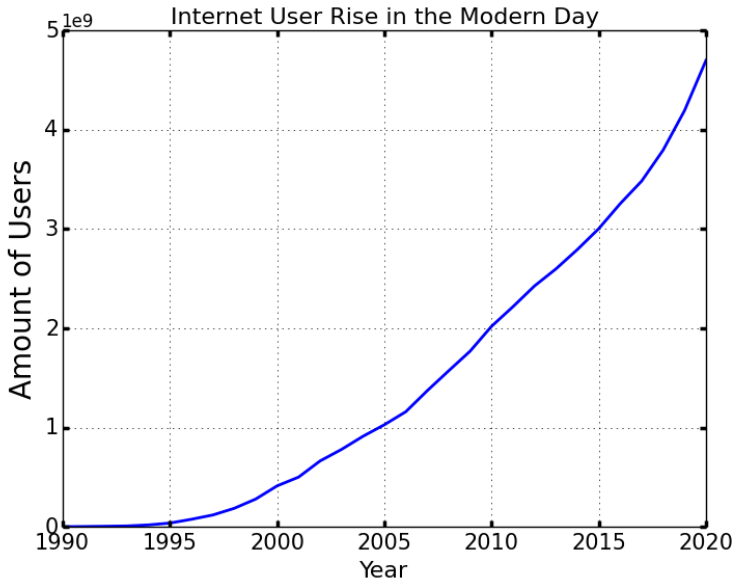

Figure 1.5: Growth of internet traffic over the years. Source : [23]

To meet increased demand, TWDM-PONs have been deployed as a standard solution. This innovative standard requires deployment of transmitters to every customers premises, thus it is vital that transmitter package costs are low. Most commonly used laser diodes are Distributed Feedback [24] and Distributed Bragg Reflector [25] lasers, which typically make use of buried, low-order Bragg gratings to achieve single mode operation. However these require precise e-beam lithography and complex regrowth steps to fabricate which drives yield down and costs up. It is thus of significant interest to make use of devices that have simpler structures for such wide network de-

ployment. High order, all-active surface grating lasers have shown great promise in such applications, and have the added bonus of simple fabrication due to their large feature size, allowing inexpensive optical lithography [26] for the patterning steps and no requirement for regrowth steps. These have been previously shown to have good output power, side mode suppression ratio (SMSR) and linewidth [27–29].

An additional strict requirement of such systems is that each devices wavelength must remain within its intended channel, only given $\pm$12.5 GHz (0.1 nm) of spectral excursion from the channel centre for 50 GHz spaced TWDM. Laser diodes based on InP material have an average wavelength drift of $\pm$12.5 GHz (0.1 nm)/^{o}C , and thus must employ some sort of temperature stabilisation method to maintain the devices wavelength. Traditionally, TECs have been included in laser packages to solve this issue, however these typically use more electrical power than the laser diode itself [30, 31] and are prone to failure [32] which leads to energy inefficient packages with reduced lifetime. One solution is then to remove the temperature sensitivity of the laser diodes wavelength in response to changing ambient temperature. This process is known as athermalisation. One method to achieve athermalisation is by varying injection currents across device sections, and thus changing the refractive index of these devices sections to offset any changes to their refractive index due to variation in ambient temperature. However, this may present its own problems as varying injection currents can lead to changes in other device parameters such as output power and SMSR. It is thus of strong interest to investigate devices which resist these changes.

For TWDM, laser diodes must be capable of operating in pulsed mode. For this type of operation, TECs are far too slow to compensate for the fast thermal transients that can occur. This is of particular concern for all-active devices as these cannot make use of fast carrier induced effects to compensate for thermally induced wavelength changes. Then, it would be of significant interest to characterise the thermal effects which effect these devices in the temporal regime, and investigate compensation techniques.

1.4.2 Scope

With the above challenges in mind, the research within this thesis focuses on simple to fabricate, all-active surface grating devices, based on laser designs previously developed by the Trinity College Dublin semiconductor photonics (TCDSP) group. Recent research within the group on such devices demonstrated tunable laser arrays, capable of covering the C-band [29] and achieving good SMSR and linewidth performance. Research based on multiple period arrays yielded increased range of operation with respect to temperature and improved SMSR [33]. Widely tunable lasers based on the Vernier effect have also been demonstrated, achieving a tuning range in excess of 50 nm and SMSR above 30 dB for the majority of the tuning range [34]. Athermal operation of such devices has also been demonstrated [35, 36] on a three section DBR design of such simple structure with continuous (mode-hop free) athermal range spanning 8-47 ^{o}C and on a master-slave configured PIC from 10-60^{o}C [37]. While these ranges are significant in their own right, expansion to wider range athermalisation for such devices is desirable.

As mentioned in section 1.4.1, transient thermal drift may be a significant challenge to overcome for these devices. While experimental data is available for DFB devices [38], little to no transient characterisation of slotted devices is available. In particular, transient characterisation with respect to wavelength change, and potential mitigation techniques are of interest.

Thus, with the above in mind, the goals of this thesis are to:

- Further develop athermalisation theory.
- Experimentally characterise devices which may be suitable for wide range athermalisation and choose an optimal device for this mode of operation.
- Continuously athermalise the chosen device over a wide temperature range while recording any changes in properties over the athermal range. Simultaneously, demonstrate that this same mechanism can be applied to multiple wavelengths spanning across the DWDM grid.

- Develop a method to measure thermal impedance, as a natural consequence of the athermalisation condition for all-active devices.
- Perform transient characterisation and compensation of these devices, both in terms of wavelength change and temperature change.

Chapter 2

Semiconductor Laser Theory

2.1 Introduction

All lasers require three basic attributes, which are,

- A gain medium.
- A pump source.
- A feedback mechanism.

The gain medium is required for amplification of light within the laser structure. For this to be possible, electrons need to be present in the higher energy state, which can be achieved via a pumping source (which could be either optical or electrical). When electrons exist in the higher energy state, they can be relaxed to a lower energy state by a photon, emitting another photon with identical properties of the initial photon, resulting in gain. This is known as stimulated emission. However, lasers may also incur losses, such as light being absorbed by the gain material or light escaping the laser cavity. For lasing to occur, the losses must be overcome by the gain. To achieve this, a feedback mechanism is required. Typically, two partially transparent mirrors, along the propagation direction of the light are used. This forms a laser cavity within which light is mostly confined longitudinally. Due to the confinement of the light, it passes through the gain material a multitude

of times, resulting in an increased amount of stimulated recombination and thus larger gain. As the gain overcomes the cavity losses, lasing will occur and for semiconductor lasers this is generally possible for a multitude of wavelengths, better known as modes. Typically, single mode operation is desired and thus wavelength selectivity is built into one or both of the mirrors, which is normally achieved using a Bragg grating structure. This structure drastically increases the losses for all modes but one, resulting in single mode operation. In this chapter, we will introduce all of these concepts in detail, as well as common semiconductor laser structures, their properties and uses within optical access networks.

2.2 Optical Processes and Rate Equation

Semiconductor materials exhibit a defining feature, which is an absence of electronic states between the valence and conduction bands which gives rise to a gap between the two bands, i.e., a band gap of energy E_g. The formation of bands is a fundamental phenomenon, resulting from the solutions of the wave equation. Single atoms have discrete energy states which electrons can occupy. At $T = 0$K, the lowest unoccupied state forms the basis for the conduction band and the highest occupied state forms the basis for the valence band.

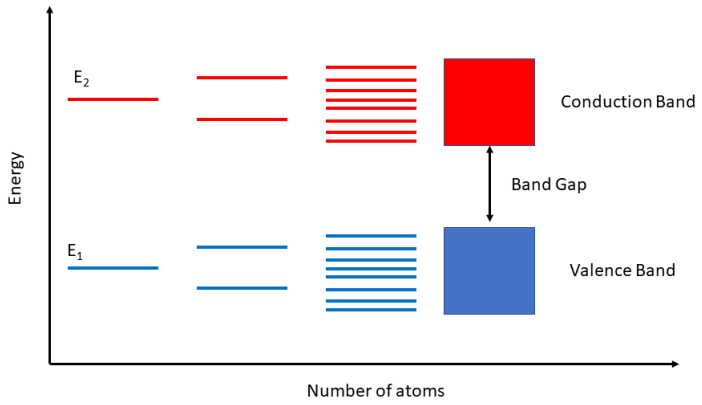

Figure 2.1: An example energy level splitting diagram as more atoms are brought closer together.

As more atoms are brought together, these single electronic states experience energy splitting, and as the number of atoms nears infinity, as it does for a solid, the energy splitting becomes infinitesimally small, forming continuous bands. This behaviour is illustrated in figure 2.1.

The above figure suggests that transitions between any valence band and conduction band states of the same energy is possible, however this is not true. In addition to energy conservation, momentum conservation must also be considered. An energy versus momentum (E-k) plot is given in figure 2.2. Due to photons possessing negligible momentum, transitions between the conduction and valence band must have the same k-vector, or within the diagram, only vertical transitions are possible, without interactions from phonons.

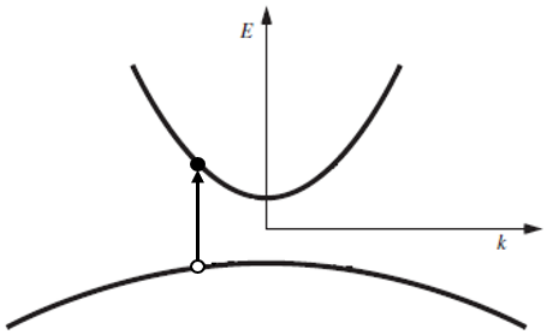

Figure 2.2: Energy versus momentum illustration for semiconductor materials. An example transition is shown.

Due to this, semiconductors with direct band gaps, where the highest energy of the valence band coincides with the lowest energy of the conduction band at the same wave-vector have become the obvious choice for photonic semiconductor devices. Such materials include III-V semiconductors like InP, GaAs and GaN. While direct band gap semiconductors are the ones which are predominantly used, photonic integrated circuits (PICs) based on indirect band gap semiconductors are also on the rise. A detailed review of these devices and their advantages is given in reference [39].

The aforementioned band structure gives rise to three key optical processes in semiconductor solids. Absorption, spontaneous emission, and stimulated emission. They are illustrated in figure 2.3.

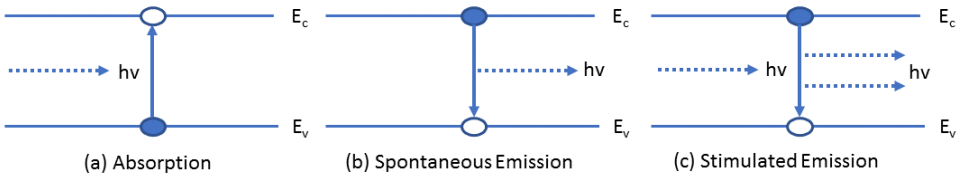

Figure 2.3: Optical Processes in Semiconductors.

Absorption is the process by which a photon of equal or greater energy than E_g excites an electron from the valance band to the conduction band, being absorbed in the process. This leaves a positively charged quasiparticle in the valance band, called a hole. The rate of this process, denoted as R_{abs}, is directly proportional to the photon density N_p. Spontaneous emission is the process in which the electron and the hole recombine spontaneously, creating a photon with energy equal to the energy difference between the hole and the electron. This photon naturally has random phase as the time of emission and direction are arbitrary. The rate of this process, R_{sp}, is directly proportional to the carrier density squared or N^2 for undoped active regions. Finally, stimulated emission is when a photon is incident upon an electron in the conduction band. The perturbation induced by the photon can cause the electron to recombine with a hole, producing a photon with identical energy and phase. This third process is key to semiconductor laser operation and its rate, R_{st}, is proportional to $N_p(N - N_{tr})$ where N_{tr} is the transparency value of electron density. Finally, there also exist non-radiative recombination processes, where the an electron may recombine with a hole without emitting any light. For semiconductors, two key processes lead to non-radiative recombination. One is due non-radiative recombination centres such as point defects and this process is directly proportional to the carrier density. The second is due to Augier recombination, in which the electron-hole recombination energy is given to another electron or hole, exciting it to a higher state. This process is proportional to N^3 because of the need for

both an electron-hole pair and a third particle. The total recombination rate can then be written as,

$$R_{rec} = R_{sp} + R_{nr} + R_l + R_{st} \tag{2.1}$$

where R_l is the carrier loss due to carrier leakage, and R_{nr} encompasses all of the non-radiative recombination processes. This equation can be further rewritten as,

$$R_{rec} = AN + BN^2 + CN^3 + R_{st} \tag{2.2}$$

where A,B and C are the coefficients of non-radiative, bimolecular and Auger recombination respectively. As the first three terms refer to unstimulated carrier decay processes, they are normally described by a carrier lifetime, τ. Then, the first three terms could be more simply rewritten as $\frac{N}{\tau}$, giving the recombination rate as,

$$R_{rec} = \frac{N}{\tau} + R_{st} \tag{2.3}$$

Treatment of R_{st} requires another approach, as it is directly dependant on the photon density. The growth in photon density ΔN_p, as it passes through a small region Δz, can be given by,

$$N_p + \Delta N_p = N_p \exp(g\Delta z) \tag{2.4}$$

where g is the incremental growth per unit length. Assuming that Δz is small, we can expand the exponential, and knowing that $\Delta z = v_g \Delta t$, where v_g is the group velocity, we can write the change in photon density as,

$$\Delta N_p = N_p g v_g \Delta t \tag{2.5}$$

Then, the rate of change of carriers due to stimulated recombination can be written as,

$$R_{st} = \frac{\Delta N_p}{\Delta t} = N_p g v_g \tag{2.6}$$

Then putting it all together, the carrier recombination rate is given by,

$$R_{rec} = \frac{N}{\tau} + N_p g v_g \tag{2.7}$$

So far, we had looked at rates at which electrons recombine either radiatively or non-radiatively, however for lasing to occur, there must also be generation of electrons. One way of generating electrons within the conduction band is by transferring them from the valence band by applying a voltage across the laser material. The generation rate of electrons within the conduction band due to an applied current is given by,

$$G_{gen} = \frac{I\eta_i}{Vq} \tag{2.8}$$

where I is the injection current, η_i is the injection efficiency, q is the elementary charge and V is the volume of the active region. Then, the change in carrier density over time can be given by,

$$\frac{dN}{dt} = G_{gen} - R_{rec} = \frac{I\eta_i}{Vq} - (\frac{N}{\tau} + N_p g v_g) \tag{2.9}$$

This is known as the laser rate equation and is important for determining many steady state and transient laser dynamics, more on this analysis can be found in reference [40].

2.3 Double Heterostructures

The dynamics described in the previous section are most commonly used (for semiconductors) within the basic double heterostructure, i.e., an undoped active region with relatively low bandgap which is sandwiched between two wide-bandgap materials, one of which is p-doped and another which is n-doped (see figure 2.4). When the junction is forward biased, electrons from the n-doped region and holes from the p-doped region move into the active region. As this region is surrounded by higher band gap material, the electrons and holes do not have the necessary energy to overcome the energy barriers and are confined, thereby increasing their probability of recombining with each other within the active region. This results in significant sponta-

neous emission at the band gap energy, as would occur in light emitting diodes (LEDs).

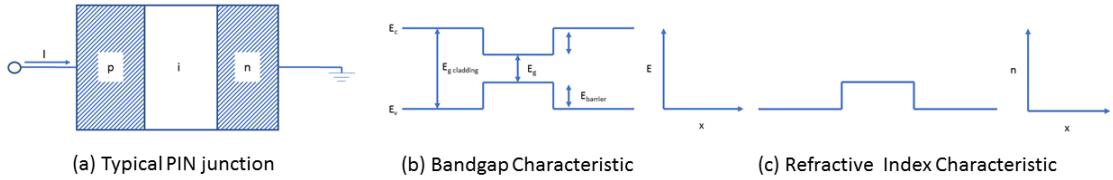

Figure 2.4: P-I-N junction, with its bandgap and refractive index characteristics shown.

The thickness of the active region plays a important role on the optical properties of the structure. If the thickness is below ≈100 nm (or near the de Broglie wavelength), quantum confinement occurs along the direction of the junction.

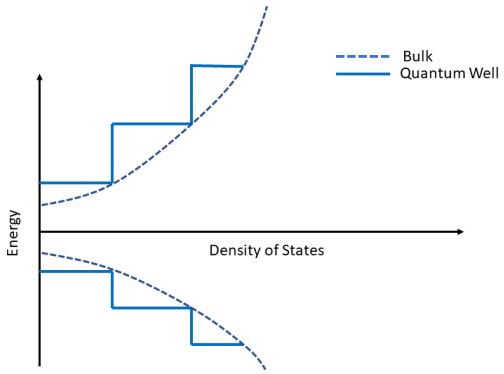

Figure 2.5: Example of electronic state splitting along the direction of the junction.

This effectively breaks the continuum of electronic states in the valance and conduction bands, splitting it into much more narrow (but not necessarily discrete) energy states forming a Quantum Well (QW) structure, as shown in figure 2.5. Thus there is a significantly increased probability of optical transition at these energies, resulting in increased gain. This gain can be further increased via lattice parameter miss-matching, causing strain

on the quantum wells. This reduces the available density of states at the valence band, resulting in population inversion occurring at lower carrier densities [41]. As the wide band gap material has higher refractive index than the active region, this would naturally result in transverse optical confinement, however the low thickness of the double heterostructure results in significantly poorer confinement than if this was a bulk structure. To solve this issue, separate confinement heterostructure quantum well (SCH-QW) structures have been developed [42]. This adds a third material (cladding) to the structure of even higher bandgap energy and large thickness, resulting in significantly improved optical confinement. Finally, to further increase the gain, multiple quantum wells (MQWs) may be grown in series. An example energy diagram of a QW, SCH-QW and SCH-MQW structure is shown below.

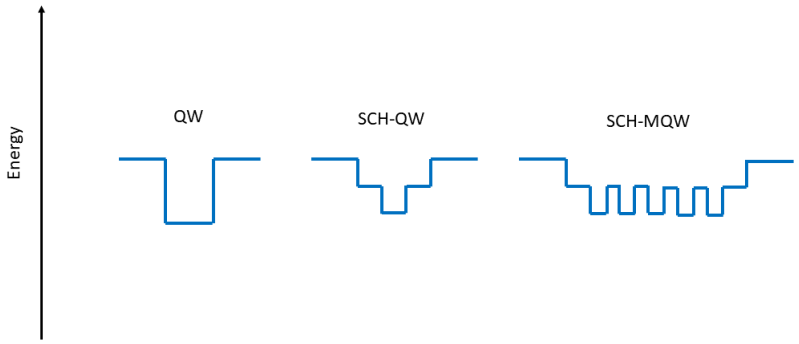

Figure 2.6: An illustration of QW, SCH-QW and SCH-MQW energy level diagrams. The energy level scaling is arbitrary and not representative of real devices.

Then, to produce lasing action, optical feedback is needed which can be easily achieved by cleaved facets on the device. This air-semiconductor discontinuity provides a large change in refractive index and a reflection coefficient of approximately 30%. The light which is randomly emitted longitudinally along the cavity will reflect backwards through the active region of the heterostructure, inducing stimulated recombination along its path, resulting in an avalanche amplification effect. This will then cause coherent light to travel back and forth between the facets, resulting in lasing action

when losses are overcome, which is known as a laser achieving threshold. The basic cavity that was described just now is known as a Fabry-Perot cavity.

2.4 Semiconductor Laser Cavities

As outlined in section 2.3, a Fabry-Perot cavity is the most basic cavity, an image of which is shown in figure 2.7.

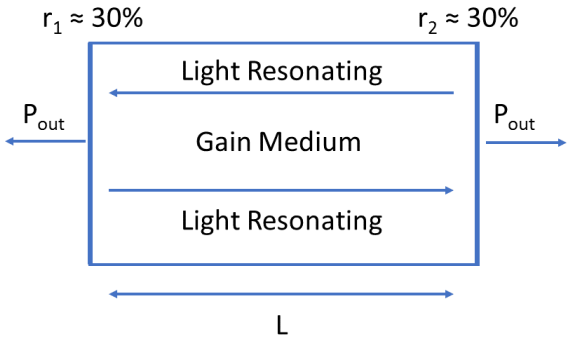

Figure 2.7: Illustration of a basic Fabry-Perot Cavity.

The electric field within the cavity can be described by,

$$E = \hat{e}_y E_0 U(x,y) e^{j(\omega t - \widetilde{\beta} z)} \tag{2.10}$$

where $\hat{e}_y$ is the unit vector indicating TE polarization, E_0 is the magnitude of the field, $U(x,y)$ is the normalised electric field profile, $\widetilde{\beta}$ is the complex propagation constant which includes any loss or gain and is given by,

$$\widetilde{\beta} = \beta + j\beta_i = \beta + \frac{j}{2}(\langle g \rangle_{xy} - \langle \alpha_i \rangle_{xy}) \tag{2.11}$$

where the real part is $\beta = \frac{2\pi\tilde{n}}{\lambda}$ with n being the effective refractive index, $\langle g \rangle_{xy}$ is the incremental transverse modal gain and $\langle \alpha_i \rangle_{xy}$ is the internal modal loss, both of which can be found from the weighed averages of the gain and loss, across the mode shape $U(x,y)$. For a mode to reach threshold, the round trip gain in the active region must offset the propagation and mirror

losses, so that the electric field exactly regenerates itself after one round trip. Assuming a cavity of length L and facet reflectivities of r_1,r_2 then a laser will reach threshold if it satisfies the following condition [40],

$$r_1 r_2 e^{-2j\widetilde{\beta}L} = 1 \tag{2.12}$$

Solving for $\langle g \rangle_{xy}$ gives,

$$\langle g \rangle_{xy} L = \Gamma_{xy} g L = \langle \alpha_i \rangle L + ln(\frac{1}{R}) \tag{2.13}$$

where Γ_{xy} is the transverse confinement factor, $R = r_1 r_2$ is the mean mirror intensity reflection coefficient and $\langle \alpha_i \rangle$ is the average internal loss. Simplifying further, the equation can be rewritten as,

$$\langle g \rangle = \Gamma g = \langle \alpha_i \rangle + \alpha_m \tag{2.14}$$

where Γ is the confinement factor. The mirror loss, α_m, can be written as,

$$\alpha_m = \frac{1}{L} ln(\frac{1}{R}) \tag{2.15}$$

Then, we can solve for modal wavelength, which gives the following solution,

$$\lambda_m = \frac{2nL}{m} \tag{2.16}$$

where m is the longitudinal mode number and is strictly an integer. Hence a Fabry-Perot cavity will lase with discrete wavelengths, separated by,

$$\Delta\lambda = \frac{\lambda^2}{2n_g L} \tag{2.17}$$

where n_g is the effective group index, which is given by $n_g = n - \lambda(\frac{\partial n}{\partial \lambda}) = n + \omega(\frac{\partial n}{\partial \omega})$. This results in a broadband spectrum, with an outline matching the gain spectrum as shown in figure 2.8. This figure also includes experimental results from a 400 μm Fabry-Perot laser.

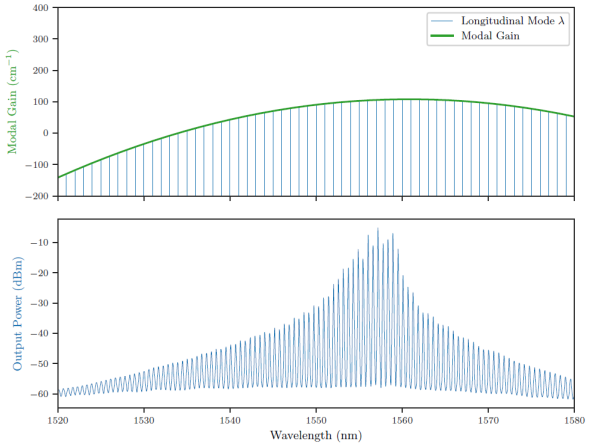

Figure 2.8: Cavity modes solved from equation 2.16, with the gain spectrum outline (top) and experimental Fabry-Perot spectrum for a 400 μm laser (bottom). Source : [36]

This type of multi-modal lasing is not particularly useful within the scope of this thesis. The main reason for this is that for optical communications, many independently sourced signals are combined together, and each of these need to be on their own unique wavelength. Thus multimode lasing would have catastrophic effects on an optical communications system by severely corrupting neighbouring signals. Thus, what is desired is single mode operation, where a single spectral line is dominant. To achieve this type of operation, one of the facet reflectors is typically coated with a reflective coating ($r_1 \cong 100\%$) and the other is replaced with a structure of varying refractive index, which will act as a wavelength selective filter.

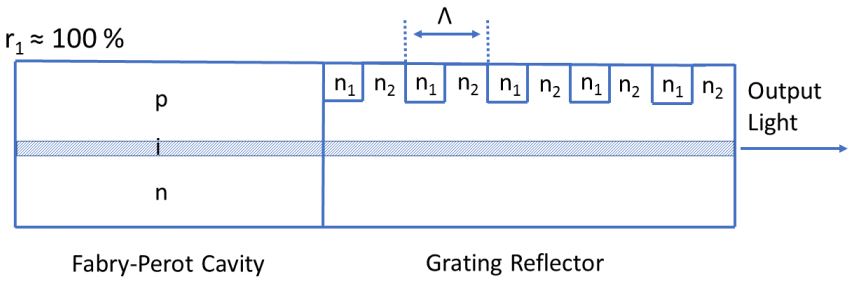

Figure 2.9: Fabry Perot Cavity with one of the facets replaced with a grating reflector. Period length and indices of refraction are indicated.

The structure employed in Distributed Bragg Reflector and Distributed Feedback lasers is called a grating and it consists of periodic variations of refractive index which can then result in single mode operation, an example is shown in figure 2.9.

Then, as there is periodic portions of the grating with different refractive index, reflection will occur at each interface. Each of these interfaces provide relatively small reflection and collectively add up to a large total reflectivity. The variation widths and periods are designed in such a way that constructive interference occurs at a desired wavelength and destructive interference occurs at every other wavelength resulting in single mode operation [43]. The desired wavelength is called the Bragg wavelength and the m'th harmonic of this wavelengths given by,

$$\lambda_B = \frac{2n\Lambda}{m} \tag{2.18}$$

where Λ is the period length and m is period order. This results in multiple reflective peaks, which can then cause mode hops called Free Spectral Range (FSR) mode hops. The spacing between the Bragg peaks or otherwise known as the FSR is given by,

$$\Delta\lambda_B = \frac{\lambda^2}{2n_g\Lambda} \tag{2.19}$$

In the case of a grating structure, the reflectivity is also wavelength dependent and hence, as shown in equation 2.14, so is the mirror loss.

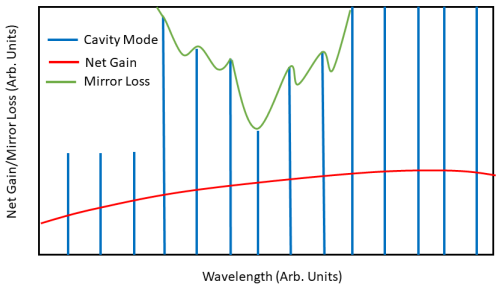

Figure 2.10: Illustration of cavity modes, along with the gain spectrum and mirror loss. The overlap of all gives the lasing peak.

Alignment of the reflectivity with a cavity mode will then result in lasing, assuming other conditions are also met, as shown in figure 2.10.

2.5 Basic Light Characteristics of Semiconductor Lasers

All laser diodes exhibit several important characteristics which need to be characterised. These play a key role in optical communication systems and ones which are of particular interest to this work are discussed below.

2.5.1 Laser Wavelength and Tunability

The most important parameter of lasers is their emission wavelength. It plays a key role in WDM systems, and in spectroscopy measurements. It is typically measured using an Optical Spectrum Analyser (OSA) which uses a diffraction grating alongside a photodiode to measure this property. Typically these instruments can give detailed analysis of the entire lasing spectrum. A significant advantage of semiconductor lasers is that their output wavelength can be finely tuned via variation of electrical bias across laser sections. Variation of electrical bias/current leads to a change in refractive index of the material. As seen in equations 2.16 and 2.18, the Bragg peak and also the Fabry-Perot mode positions are dependent on refractive index. Hence, changes to refractive index induce variations in wavelength. Additionally, changes to the device temperature also induces a shift in the material gain spectrum thus influencing lasing wavelength. These mechanisms are discussed in detail below.

- **Free Carrier Plasma Effect** induces a negative change in refractive index due to injection of electron-hole plasma into a semiconductor. There are two mechanisms which cause the change in refractive index. One is the polarisation of the free carriers which reduces the index proportionally to the carrier density. The second is related to the spectral shift of the absorption edge of the semiconductor material to higher

energies which also results in a negative change of refractive index. Relatively large changes in refractive index are possible, typically up to -0.04. One downside of this mechanism is that it leads to parasitic thermal tuning, which reduces the overall effectiveness of the mechanism, however it is still significant and is widely used. One noteworthy advantage is that this effect occurs very quickly, on the order of 100s of picoseconds. The change of the real part of the refractive index can be quantified by the following equation [44],

$$\Delta n = -\frac{e^2\lambda^2}{8\pi^2 c^2 n\epsilon_0}(\frac{1}{m_e} + \frac{1}{m_h})N \tag{2.20}$$

where m_e and m_h are the electron and hole effective masses and N is the carrier density. The imaginary part of the refractive index can be expressed as,

$$\Delta\widetilde{n} = \frac{e^3\lambda^2}{4\pi^2 c^3 n\epsilon_0}(\frac{1}{m_e^2\mu_e} + \frac{1}{m_h^2\mu_h})N \tag{2.21}$$

where μ_e and μ_h are the electron and hole mobilities.

- **Quantum Confined Stark Effect** can induce both a negative or a positive change in refractive index depending on device wavelength, the device used or the material composition [45]. However, for the devices within this thesis the change is generally negative. This is due to an applied electric field. The effect occurs when a pn junction is placed under reverse bias, thereby reducing the bandgap energy, pushing the band-edges towards each other. This induces a large change in absorption coefficient and hence refractive index. The changes in refractive index achieved using this method are not particularly large, on the order of 10^{-3} to 10^{-2} [46], however, this effect does not generate any parasitic thermal effects, and is similarly fast to the Free Carrier plasma effect. Furthermore, the increase in absorption coefficient has other uses than just wavelength tuning, i.e., burst mode and wavelength switching applications.

- **Thermal Tuning** is the third and one of the most important tuning ef-

fects which is able to tune refractive index and thus wavelength. Using a classical Lorentz model, the change in refractive index with temperature, better known as the thermo-optic coefficient can be expressed as [47],

$$\frac{dn}{dT} = \frac{n^2 - 1}{2n}(-3\alpha(T) - \frac{2}{E_g}\frac{1}{1 - \frac{E^2}{E_g^2}}\frac{dE_g}{dT}) \tag{2.22}$$

where $\alpha(T)$ is the linear thermal expansion coefficient. This equation suggests that the thermo-optic coefficient depends on temperature for two basic properties of the material. Its thermal expansion and the change in bandgap energy with temperature. For semiconductors, the effect of the bandgap shift is dominant and the thermo-optic coefficient is therefore positive. A secondary effect of the bandgap shift is a change in the gain spectrum peak, which redshifts with increasing temperature. The change in wavelength due to the combined effects is approximately 0.1 nm/^{o}C for InP. However, it must be noted that there is also a gain spectrum shift of around 0.5 nm/^{o}C, which is an important factor to take into account when designing laser diodes. This type of tuning may arise due to resistive (Joule) heating of the device due to injection of current or it may be induced by a TEC or just by ambient temperature fluctuations. This effect is relatively slow when compared to others (response time with time constants of 10s of ns to 10s of μs), with the temperature evolution for a given section, when subjected to a heat source such a Joule heating, is which is given by [48],

$$\frac{\partial T(x,y,z,t)}{\partial t} = \frac{K}{\rho C} \bigtriangledown^2 T(x,y,z,t) + \frac{Q(x,y,z,t)}{\rho C} \tag{2.23}$$

where K is the thermal conductivity, C is the specific heat, ρ is density and Q is the heat generation. x, y, z correspond to spatial co-ordinates and t corresponds to time. It must be noted however that increases in temperature will affect the amount of nonradiative losses, which will inadvertently affect the output power and laser threshold. As such, excessive rises in temperature may put the laser below threshold, or make its output power too low for optical access networks, effectively

limiting the effective range of tuning that is achievable.

While the tuning in refractive index will always be continuous, wavelength or other parameters do not necessarily tune continuously. This is mostly due to tuning of separate sections at different rates. For example, if the grating is tuned at a faster rate than the Fabry-Perot section, then it will eventually favour the next mode more in terms of reflectivity and will cause a mode hop, which is a discontinuous jump in wavelength. Three types of possible tuning regimes are shown below.

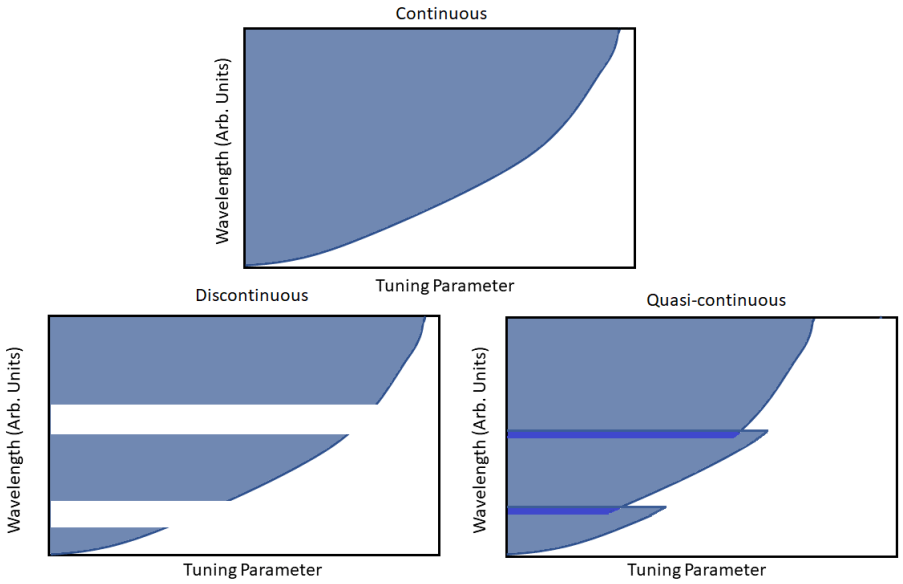

Figure 2.11: Three tuning regimes available for laser parameters.

First, is the continuous tuning regime, where the wavelength (or other parameter) is continuously available throughout the entire tuning range. Next, is discontinuous tuning, where there exists gaps in the measured parameter, however typically leading to a larger tuning range, and finally, there is quasi-continuous tuning, in which the discontinuities overlap. For optical communications, it is desirable to have continuous tuning, particularly as when mode hops occur, there are spikes in optical output power and a plummeting of side mode suppression ratio, which is detrimental for these systems.

2.5.2 Side Mode Suppression Ratio

As discussed earlier, a grating structure is normally used to achieve single mode operation. However, full suppression of all cavity modes is not possible due to the width of the reflective peak not being infinitely thin. Another reason may be that the FSR is too low, meaning that higher/lower order reflective peaks may overlap with the gain peak, resulting in lasing at those wavelengths. Then, it is useful to define a parameter which quantifies how single mode the laser is, with this parameter being called Side Mode Suppression Ratio (SMSR). It is the ratio of the highest power mode divided by the second highest power mode, or in equation form,

$$SMSR = 10 \times \log_{10}(\frac{P(\lambda_0)}{P(\lambda_1)}) \tag{2.24}$$

Typically, SMSR values of above 30 dB are acceptable for optical communications, however current devices are capable of achieving values which are significantly higher. This parameter is typically also measured using an OSA.

2.5.3 Threshold

Laser threshold is known as the current at which the laser first begins lasing in a given mode. It is typically measured using a photodetector, with current being applied to the laser in a linear fashion, and output power being measured by the photodetector. Threshold is then seen as a sharp jump in output power, and typically increases linearly from then on with applied current. Threshold current can be analytically approximated using device parameters in the following manner [40],

$$I_{th} \approxeq \frac{qVBN_{tr}^2}{\phi_i} \exp 2(\langle \alpha_i \rangle + \alpha_m/\Gamma g_{0N}) \tag{2.25}$$

with g_{0N} being a gain coefficient. It is then apparent that shorter lasers would have lower threshold due to the intrinsic dependence of internal loss and transparency value of electron density, which has resulted in a large interest in devices which lengths are on the order of micrometers. This threshold

current is highly temperature dependant, due to many device parameters being affected by thermal changes. Fortunately, all of these variations can be grouped into a single parameter, T_o, and modelled as such,

$$I_{th} = I_o \exp(T/T_o) \tag{2.26}$$

With I_o being the threshold current at 0K. Then, knowing threshold at a few currents, threshold at different temperatures can be easily approximated. This approach is particularly effectively for devices with a single active section.

2.6 High Order Surface Grating Semiconductor Lasers

Currently deployed and commercially successful lasers are not too different from the one described in the previous section.

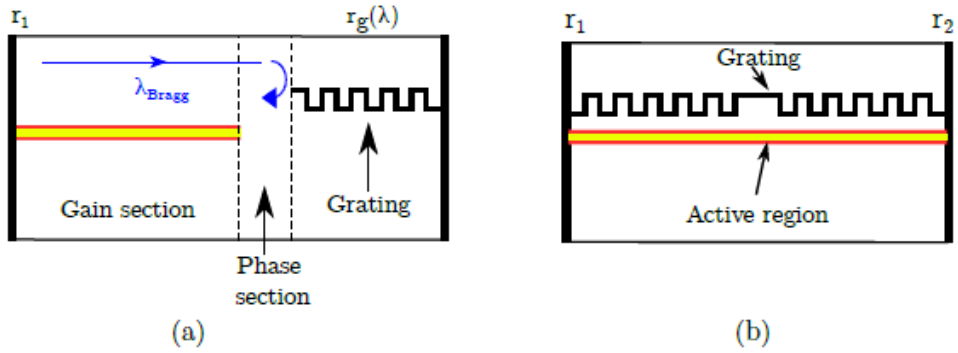

Figure 2.12: A typical DBR cavity (left) and a typical DFB cavity (right). Source : [36]

They are known as Distributed Bragg Reflector (DBR) and Distributed FeedBack (DFB) lasers [49] which have excellent output power, high side mode suppression ratio, narrow linewidth, low threshold, great tunability across the C-band (1530 nm to 1565 nm) when in array arrangements and typically exhibit high modulation response [38]. The laser which is most

similar to the one talked about in section 2.4 is the DBR, a schematic of which is shown in fig 2.12 (a) [36].

An additional section is normally added in to the design shown in figure 2.12, in a way of a phase section. This allows for fine control of the Fabry-Perot mode positions without affecting the gain of the laser. The design of DFBs is a bit different compared to examples shown so far. In this structure, the grating is built upon the active region as shown in figure 2.12 (b). Initial designs included a quarter wave shift in the middle of the structure to avoid the cavity being anti-resonant and to allow lasing at the Bragg frequency, however, nowadays different phase shifts have been introduced for both practical and different application reasons [24, 50]. The advantage of these lasers over standard DBRs is their relative fabrication simplicity. However, both types of these lasers have historically employed low (1st or 2nd) order, buried grating structures which require high resolution lithography to fabricate. Additionally, the repeating grating structure is formed by etching and regrowth of a material with a slightly different refractive index. This regrowth step is prone to error and significantly reduces device yield. Hence, it is of strong interest to realise a laser which does not require regrowth or high resolution lithography. One solution is to make use of surface gratings [51]. Surface grating structures are etched directly into the ridge waveguide, creating what is called slots while requiring no regrowth steps. A high order grating is also used and hence feature size is large, allowing the use of photolithography. It should be noted that for devices within this thesis, e-beam lithography was used due to no availability of a stepper at the foundry. Furthermore, as the semiconductor-air interface provides a large discontinuity in refractive index, fewer periods/slots are needed and thus there is more room for error in fabrication. For our group, these lasers were fabricated on a commercially purchased wafer, which consists of 5 AlGaInAs QWs, above which there is a 1.6 μm p-doped InP layer (referred to as cladding here), 50-nm thick, p-doped InGaAsP layer, and a 200 nm InGaAs contact layer. Below the quantum wells there is 120 μm layer of InP. Detailed layer structure is provided in table 2.1. The slots and the ridge of the laser are fabricated using two inductively coupled plasma (ICP) etch steps using Cl_2 and N_2 gas,

with and illustration of the process shown below and the specific steps used to form the ridge/slots being the following;

1. Silicon Nitride layer is deposited using a plasma enhanced chemical vapour deposition process.
2. Electron beam lithography is used to define the slots.
3. SiO_2 is deposited to prevent etching of slots during the first ICP etch.
4. First ICP etch step is performed to a depth of 0.5 μm.
5. SiO_2 is removed to allow etching of the defined slot patterns.
6. Second ICP etch is performed to a depth of 1.35 μm. Giving slot depth of 1.35 μm and a ridge height of 1.85 μm.

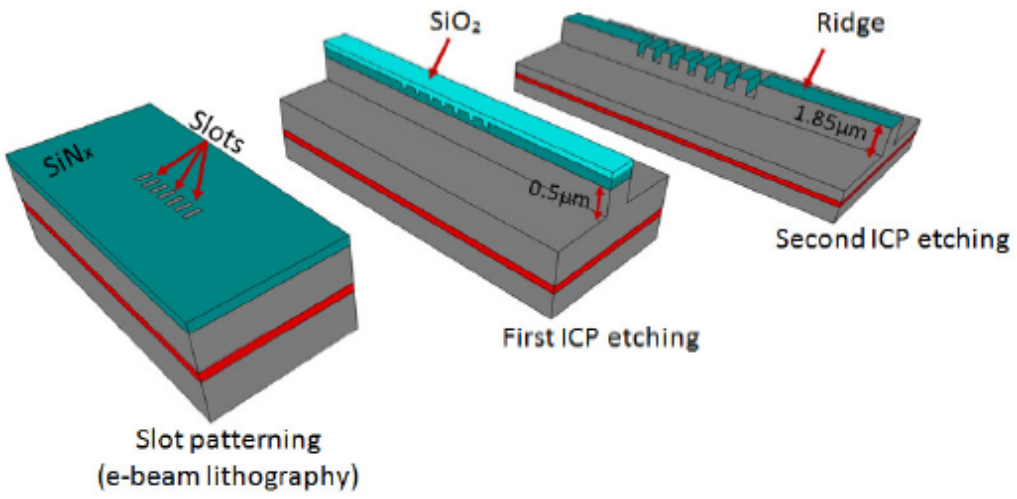

Figure 2.13: Illustration of the manufacturing process of our laser devices. First, showing definition of the slots is performed (left), then the first ICP etch is shown (middle) and finally, second ICP etch is performed (right).

The laser is subsequently contacted, cleaved and the facets are coated with high reflection (HR) and anti-reflection (AR) films, before being eutectic bonded onto an AlN carrier. As the slots were etched into the ridge, the need for regrowth steps was removed.

Table 2.1: Layer structure of the QW wafer.

Layer	**Material**	**Group**	**Repeat**	**x**	**y**	**Strain** (ppm)	**PL** (nm)	**Thickness** (μm)	**Dopant**	**Type**	**Dopant density** (cm^{-3})
16	$GaIn_xAs$	-	-	0.53	-	0	-	0.2	Zn	P	$> 1.5e^{19}$
15	$GaIn_xAs_yP$	-	-	0.71	0.62	0	1300	0.05	Zn	P	$> 3.0e^{18}$
14	InP	-	-	-	-	-	-	0.1	Zn	P	$> 1.5e^{18}$
13	InP	-	-	-	-	-	-	1.5	Zn	P	$= 1.0e^{18}$
12	$GaIn_xAs_yP$	-	-	0.85	0.33	0	-	0.02	Zn	P	$= 1.0e^{18}$
11	InP	-	-	-	-	-	-	0.05	Zn	P	$= 7.0e^{17}$
10	Al_xGaIn_yAs	-	-	0.90	0.53	0	-	0.06	-	-	-
9	Al_xGaIn_yAs	-	-	0.72-0.90	0.53	0	-	0.06	-	-	-
8	Al_xGaIn_yAs	-	-	0.44	0.49	-3000	1100	0.01	-	-	-
7	Al_xGaIn_yAs	1	5	0.24	0.71	12000	1530	0.006	-	-	-
6	Al_xGaIn_yAs	1	5	0.44	0.49	-3000	1100	0.01	-	-	-
5	Al_xGaIn_yAs	-	-	0.90-0.72	0.53	0	-	0.06	-	-	-
4	Al_xGaIn_yAs	-	-	0.90	0.53	0	-	0.06	Si	N	$= 1.0e^{18}$
3	Al_xGaIn_yAs	-	-	0.86-0.90	0.53	0	-	0.01	Si	N	$= 1.0e^{18}$
2	InP	-	-	-	-	-	-	0.05	Si	N	$= 1.0e^{18}$
1	InP	-	-	-	-	-	-	0.3	Si	N	$= 3.0e^{18}$
...	**Substrate**										

Lasers employing surface gratings have been previously designed and characterised by our group and have shown excellent performance in terms of output power, SMSR, linewidth and threshold current [29]. A schematic of a laser employing a surface grating and a semiconductor optical amplifier (SOA) is shown in figure 2.14.

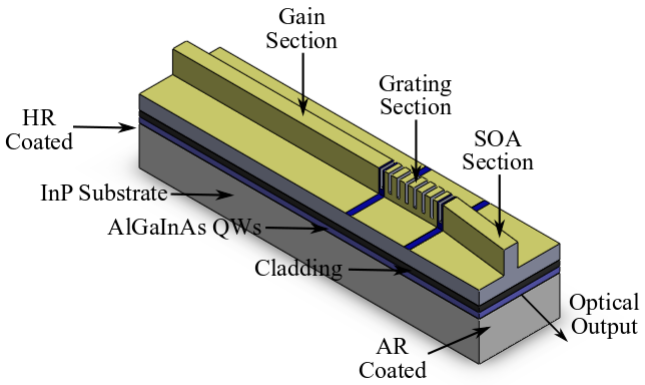

Figure 2.14: A laser developed by our group, employing a surface grating. It additionally has an SOA.

Optimal design of such devices is crucial for operation within optical networks. The length of the gain section will have an effect on output power, linewidth and SMSR, with longer devices having improved output power and reduced linewidth, while generally also having poorer SMSR assuming the grating design remains constant between devices of differing gain lengths. Thus, it is generally important to choose the correct gain section length for whichever purpose the laser is going to be used for.

Similarly, and arguably even more important is the grating design. As discussed earlier this will affect the reflectivity of the wavelength selective mirror and will have a significant effect on mainly output power and SMSR. Typically, important grating parameters are period order, the number of slots and etch depth of the slot. Period order typically has some effect on reflectivity and the FSR spacing, while the number of slots and etch depth both have significant impact on reflectivity and the reflective peak bandwidth.

Detailed analysis on how these parameters affect reflectivity is typically performed using either transfer matrix method (TMM) or the scattering matrix method (SMM), from which the reflectivity and the transmissivity of the grating structure can be calculated. As the lasers which are used within this thesis make use of slots which are etched into the ridge waveguide, a 2D-SMM approach is more applicable as it considers the unique material layers and slot depth into consideration while TMM would not, and thus would yield incorrect reflectivity spectra for our devices. SMM operates on the principle of scattering theory by using junction operators to relate incoming and outgoing waves passing through a network of scattering junctions, such as a grating. Inward (a) and outward (b) waves on impact of a junction S are considered, as shown in figure 2.15.

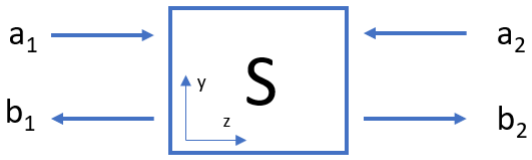

Figure 2.15: A visual aid of a two port SM junction.

The operator that relates these waves is known as the scattering matrix and is given by,

$$\begin{bmatrix} b_1 \\ b_2 \end{bmatrix} = \begin{bmatrix} S_{11} & S_{12} \\ S_{21} & S_{22} \end{bmatrix} \begin{bmatrix} a_1 \\ a_2 \end{bmatrix} \tag{2.27}$$

where S_{ij} are the scattering coefficients. Then, the unique material layers and slot depth are taken into account via the 2D electric field given by,

$$E(y,z) = E(y)e^{i\widetilde{\beta}z} = \sum_{k}^{\infty}(a_k e^{i\widetilde{\beta_k}z} + b_k e^{-i\widetilde{\beta_k}z})E_k(y) \tag{2.28}$$

where the electric field is expressed as a sum of eigenmode solutions. While to acquire an exact solution, the sum of the infinite set is required, in practice an accurate solution can be acquired after considering only the first 20-40 eigenmodes. More detail on the technique is given in [52], and in

particular for our devices in [53].

A large problem with lasers that contain such gratings is that the FSR typically falls within the gain spectrum due to their high grating order. This becomes problematic at higher temperatures since the gain spectrum will shift towards the next reflection peak and may cause mode hops to the next FSR mode. Multiple period gratings have been previously investigated which have their Bragg wavelength centred at one point, however the other harmonics are at different points due to varied FSR. This misalignment causes significant decrease in the net reflection peak for the other harmonics and hence, the next FSR mode requires larger gain to reach threshold and hence FSR mode hops occur at higher device temperatures [33]. An example reflectivity spectrum incorporating both single and triple period designs is shown in figure 2.16.

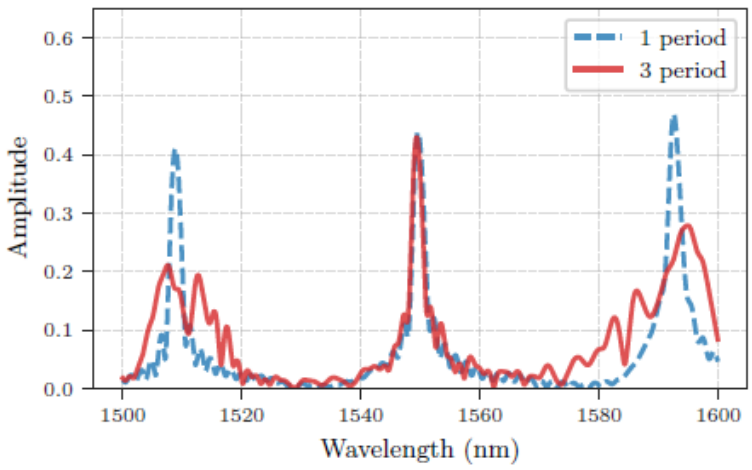

Figure 2.16: Reflectivity spectra of a single period grating compared to a triple period grating. Clearly significant reduction in reflectivity for next FSR peaks is observed. Source : [33]

It should be noted that for a more comprehensive guide on slotted laser design, the reader should have a look at [36].

2.7 Conclusion

In this chapter, we have introduced the fundamental theory of semiconductor laser diodes. Basics of laser cavities and grating structures have been introduced, alongside important light characteristics of laser diodes. Then, we introduced the laser structures which are the focus of this research, i.e., high order surface grating DBR lasers.

In the next chapters, we will cover in detail operation of these lasers under steady state and transient conditions, most of the results being geared for the TWDM transmission system. Athermalisation will be introduced, and this topic will be the root of the entire thesis.

Chapter 3

Steady State Characterisation and Optimisation

3.1 Introduction

In the previous chapter, a basic theoretical outline of semiconductor lasers is given. In particular, slotted surface grating devices are presented and their design is discussed in some detail. In this chapter, the tuning behaviour of these devices is characterised, particularly characterisation pertaining to optimal device parameters for athermal operation is performed.

To achieve wide range athermal operation semiconductor devices must meet two requirements. First, at low ambient temperatures these devices must be capable of generating sufficient self-heating, and thus operate without deteriorated performance at high currents. This may be achieved due to small device sizes, or very large injection currents. In either case, current density tends to be high, and investigation of what type of device is suitable for this mode of operation is necessary.

Secondly, at high ambient temperatures, these devices must be capable of operating at relatively low injection currents. Thus it is intriguing to investigate devices that could fit this criteria. Of particular interest are devices which have a significant red-shift of the reflective peak when compared to the gain spectrum peak at ambient temperature. These have been previ-

ously shown to have improved device performance at elevated temperatures in terms of output power and laser threshold.

Finally, we take a further look into the athermalisation condition, particularly for devices with two tuning sections. This is of particular interest as our gratings include gain, but also significantly more loss than the gain section. This could have a variety of implications for athermalisation and these are investigated.

Then, within this chapter, detailed athermalisation theory is presented in section 3.2. Conclusions drawn from the outline of the theory are then used in section 3.3 which presents results of how high order slotted semiconductor lasers perform under high current injection at ambient temperature. An optimal set of devices is selected and their performance at elevated temperatures while under low current injection is investigated within section 3.4. Then, this final device is further investigated in section 3.5, with a more detailed athermalisation analysis being applied to it. From the measurements within this chapter an optimal device for athermal operation is selected.

3.2 Athermalisation Background Theory

As mentioned earlier, athermalisation is the stabilisation of the semiconductor laser wavelength with respect to ambient temperature changes. Our devices contain an all-active structure, thus above threshold the carrier density clamps and varies only slightly with changing injection current. This results in thermal tuning being the dominant wavelength tuning mechanism. Thus, as ambient temperature varies, to maintain a constant wavelength, the device self-heating must also change in an equal and opposite way as to maintain the laser temperature constant as illustrated by equation 3.1. This will then result in the laser diodes wavelength remaining constant.

$$\Delta T_a = -\Delta T_{LD} \tag{3.1}$$

where ΔT_a is the change in ambient temperature and ΔT_{LD} is the change in laser diodes temperature. ΔT_{LD} can also be expressed (approximately) as,

$$\Delta T_{LD} = Z_{th}\Delta P_I = Z_{th}\Delta I^2 R = Z_{th}\Delta(IV) \tag{3.2}$$

where ΔI is the change in input current, R is the ohmic resistance, ΔP_I is the change in input power and Z_{th} is the thermal impedance. Thus, it is clear that to maximise the range over the ambient temperatures that the laser can operate athermally it is necessary to maximise the self-heating of the laser at lower temperatures to be able to compensate for large ΔT_a. From the given equations, it is clear that this can be easily achieved by increasing the injection current (and thus increasing the forward voltage). However, this cannot be used to increase the athermal range without limit as laser diodes have a maximum forward voltage at which they can operate without short-circuiting, and also due to laser threshold being dependent on the local temperature of the laser diode. Athermal range can then be more realistically written as,

$$T_{ar} = Z_{th}(P_i - P_{threshold}) \tag{3.3}$$

where P_i is the input power at a given current, and $P_{threshold}$ is equal to the power required for lasing at the given input current. Here an assumption is made that all of the input power is dissipated as heat. This equation can thus be rewritten as,

$$T_{ar}(I) = Z_{th}R(I^2 - I_0^2 \exp(2\frac{Z_{th}I^2R + T_a}{T_0})) \tag{3.4}$$

where, $I = I_0 \exp(T/T_0)$ was used for threshold current. Then, taking a derivative with respect to current, and solving for the maxima, we can find the current which yields the maximum athermal range, in terms of laser parameters. This solution assumes that this current is relatively large, and thus resistance would not vary much (would be relatively independent of current), and is given by,

$$I = \sqrt{\frac{T_{\mathrm{o}} \ln\left(\frac{\sqrt{\frac{T_{\mathrm{o}}}{RZ_{th}}}}{\sqrt{2}\, I_0}\right)}{RZ_{th}} - \frac{T_{\mathrm{a}}}{RZ_{th}}} \tag{3.5}$$

It can clearly be seen that the three key parameters on which this current depends on are R, T_o and Z_{th}. Thus, to maximise the athermal range it is needed to either optimise the device resistance (not practical in our case),the characteristic temperature of the device, or the thermal impedance. First we will examine thermal impedance. For a simple rectangular structure with a stripe heater source, thermal impedance can be expressed as [40],

$$Z_{th} \approx \frac{ln(4h/w)}{\pi \xi L} \tag{3.6}$$

where, L is the length of the stripe heat source, w is the width of the stripe, h is the thickness of the substrate upon which the stripe is sitting on and ξ is the thermal conductivity of the material. Knowing that most of the heating within our laser occurs within the ridge, then our laser can be approximated as a stripe heater mounted onto a thick substrate as shown in figure 3.1. The values of h,ξ and w are relatively constant within our devices, however L can change and thus thermal impedance can be varied by varying the laser/section length. Thus in the next section, devices of various lengths are investigated and their performance at differing injection currents at ambient temperature is investigated in section 3.3.

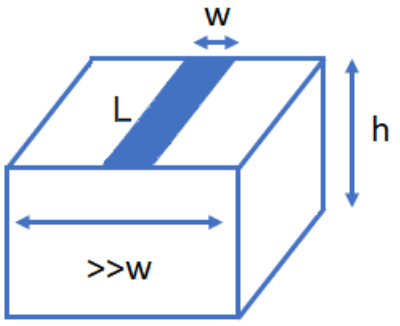

Figure 3.1: A simple model for simulating the heating of our laser devices.

Secondly, T_o dependence is investigated. As there is a requirement of

large ΔT_{LD}, this indicates that the devices need to operate at high local temperatures as well. Semiconductor lasers have been documented to experience deteriorating performance in terms of output power, threshold and linewidth with increasing ambient temperature, and thus local temperature, particularly at low injection currents. However, recent studies have shown that by misaligning the reflective Bragg peak and the gain spectrum peak some of these issues can be alleviated. Particularly, if the Bragg peak is blue-shifted relative to the gain peak then improvements in linewidth are observed [54]. However, a relative redshift provides increased output power and decreased threshold at elevated temperatures, which is due to an increase in T_o. This is due to the gain peak redshifting faster than the Bragg peak with increasing temperature(0.5 nm/^{o}C vs 0.1 nm/^{o}C), causing the gain peak to overlap more with the Bragg peak at elevated temperatures. Of course, the amount of misalignment will determine the range over which the effect is useful, however too much misalignment may lead to poor performance at lower temperatures, thus an optimal value must be determined. This analysis is performed in section 3.4.

Finally, threshold characteristics of such a device are investigated. Above, the assumption for the athermalisation condition is that current is passed into the device sections with equal current density. While to achieve continuous athermalisation an equal change in current density into both sections is required, the starting point for both sections does not need to have an equal current density. This then raises the issue that threshold cannot be calculated using an equation that uses one current, and requires consideration of two currents. Of particular interest is that the grating has far greater loss than the gain section, thus a current scheme that injects more current into the gain section and less into the grating may lead to significantly reduced threshold current, and improved athermal range. This is performed in section 3.5.

3.3 Optimisation of Laser Length for Athermal Operation

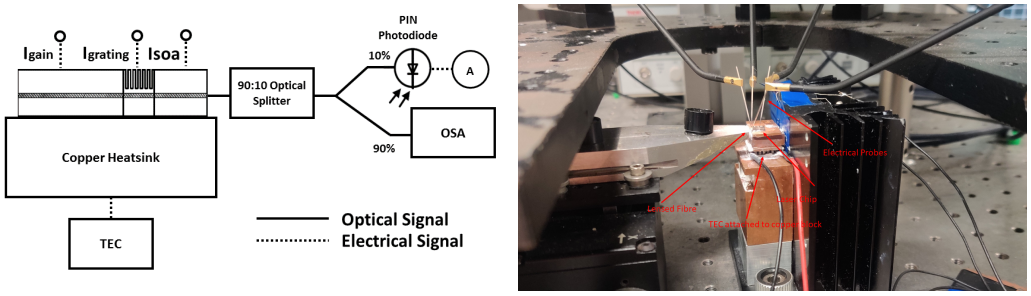

(a) (b)

Figure 3.2: (a) Steady state characterisation setup schematic (b) Real life image of the setup. The laser is provided current via electrical probes, with light collected via a lensed fibre and analysed by an OSA.

Our devices were tested on a setup shown in figure 3.2. The laser was placed on a copper heatsink, with the temperature of this heatsink being monitored and controlled using a TEC (ILX LDC-3742). This was used to simulate a consistent ambient temperature which for the following experiments was set to 20 ^{o}C. The laser is then contacted using standard probes, which are connected to ILX LDX-3220 current sources. The output light from the laser is coupled to an optical spectrum analyser (Agilent 86140B) using a lensed fibre, which is then passed through a 90:10 optical splitter. 90% of the light is passed to an optical spectrum analyser (OSA) for spectral analysis, while 10% of the light is passed to a photodiode (current of which is read by Keithley 6485 picoammeter). This is done to assist with the coupling of the device as the diodes temporal response is much faster than the integration time of the OSA, allowing improved and faster coupling.

For these measurements, equal but varied current density was passed into both the gain and grating sections to induce laser diode self-heating. By knowing the thermal impedance of the laser(see section 4.4), and the voltage across the diode, the self-heating can be easily converted to local temperature changes as per equation 3.2. Particular interest is paid to device performance

at high injection current, however performance was examined at every step due to the fact that in some instances, lower athermal ranges or differing wavelengths may be required and thus good performance at many currents is desirable.

For these measurements we had devices of three different total lengths' available, these being 400, 700 and 1000 μm. The chosen device structures were equivalent, aside from their gain section length (thus a resulting gain section lengths of approximately 170,470 and 770 μm as the grating section length is approximately 230 μm). The SOA section length is approximately 230 μm. The gratings of these devices consisted of three separate periods to minimise the FSR reflective peaks effects on the SMSR at higher currents and to maintain the wavelength within the intended reflective peak. The benefits of such gratings have been demonstrated in reference [33]. The grating parameters are given in the table below.

Table 3.1: Parameters of the triple period grating.

Period Order	Slot Order	Period Length (μm)	No. Slots	Wavelength (nm)
[35,41,47]	4.5	[8.56, 10.03,11.49]	[8,8,7]	1535-1570

It is useful here to define two quantities, one being the laser dominant wavelength (λ_{DM}) or the wavelength with the most optical power and secondly, the wavelength which has the second most power (λ_{SM}). An example spectra for the two parameters and how they may differ based on laser current is plotted in figure 3.3. It can be clearly seen from the optical spectra that λ_{DM} did not vary much in this case, however λ_{SM} did so significantly when current was varied. The impact on SMSR in this case now comes from the FSR modes rather than the regular side modes, and thus measuring these two quantities is important for quantifying when this mode competition starts.

The wavelength tuning mechanics of all three lengths are then shown in figures 3.4 (a)-(c). The device position here refers to position of the laser within the array, with the lowest number (1) referring to the bluest device and the largest number (12) referring to the reddest device.

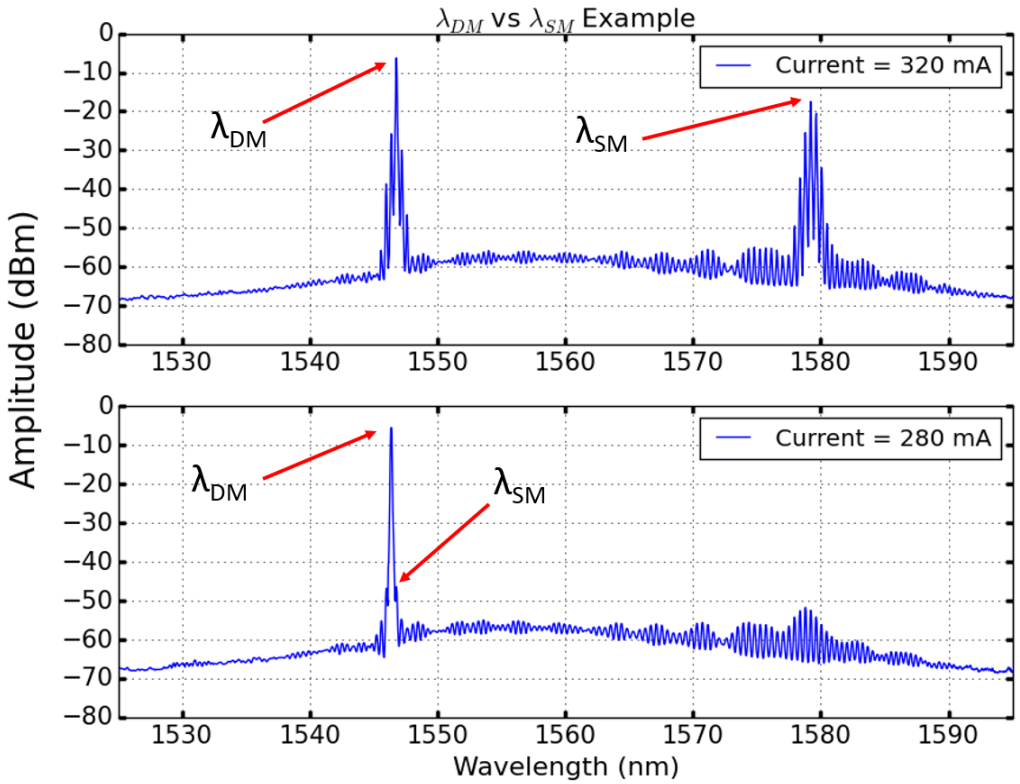

Figure 3.3: Example of spectra for a 700 μm device with differing λ_{SM} but approximately the same λ_{DM}.

It is desirable that the laser exhibits lasing within its intended reflective peak, as these particular wavelengths target the C-band telecom window. An FSR mode hop would bring all of the lasers outside of the C-band, which would then cause the laser to lase outside of set TWDM wavelength channels. As can be seen, 1000 μm devices tend to begin dominantly lasing within their next FSR, with bluer devices doing so at lower currents than redder ones. Lasers with total length of 400 and 700 μm do not seem to exhibit this behaviour and this is likely due to the fact that these devices do not have enough gain to lase within the next FSR peak due to its severely reduced reflectivity. Note that for each of the devices in terms of length, there is one that seems to jump to a new FSR at very low currents, however this is actually a measurement artefact, these devices are simply not above threshold at those currents due to slight damage at the laser facet.

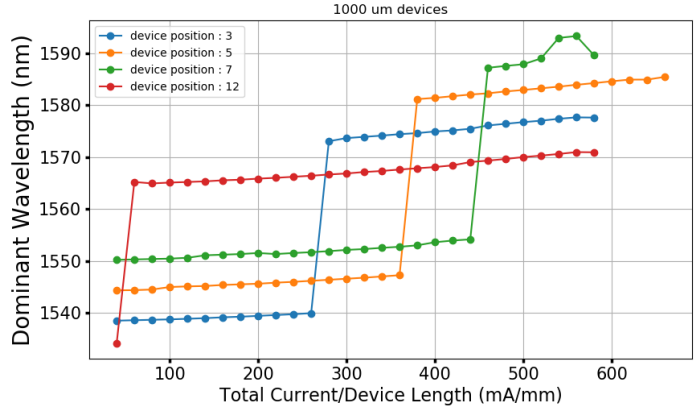

(a)

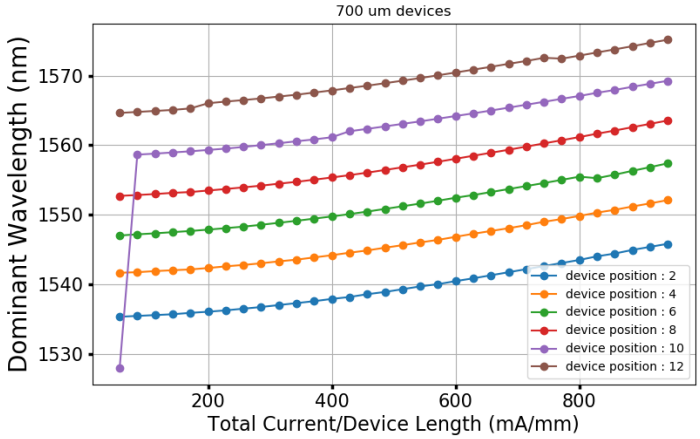

(b)

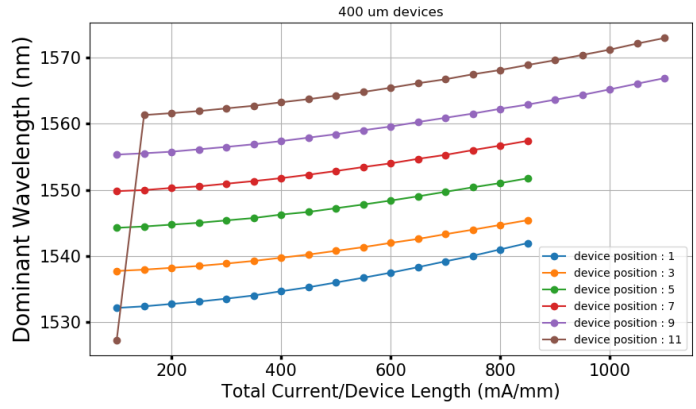

(c)

Figure 3.4: Variation of dominant wavelength versus total current/device length for (a) 1000 μm (b) 700 μm and (c) 400 μm device lengths.

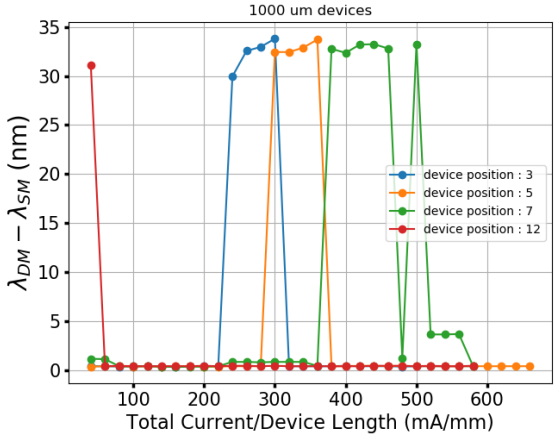

(a)

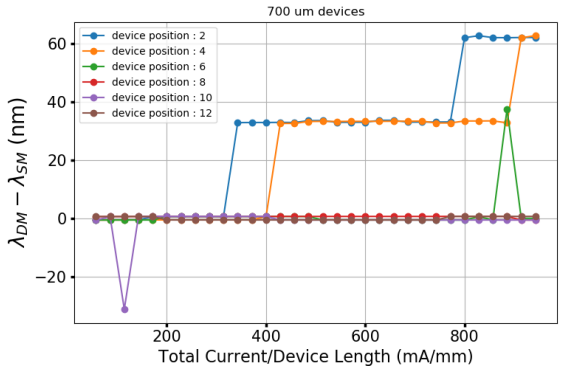

(b)

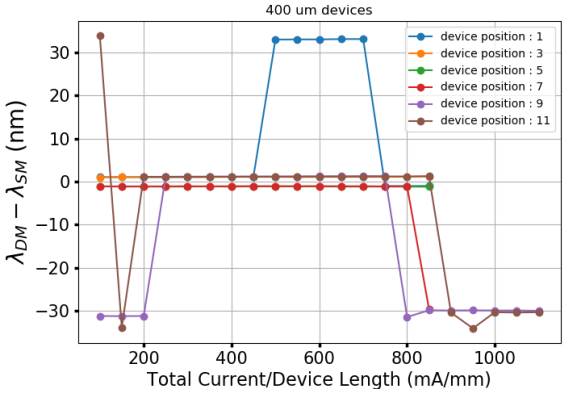

(c)

Figure 3.5: Variation of λ_{DM}-λ_{SM} versus total current/device length for (a) 1000 μm (b) 700 μm and (c) 400 μm device lengths.

It is then interesting to look at the side peak wavelength, which once again is defined as the wavelength of the second most dominant peak. In particular, it is interesting to look at the difference of the dominant wavelength versus the side peak wavelength. It would be typically expected that this difference is just the mode spacing which would be defined by the cavity length and should be small when compared to the FSR spacing. This measurement then shows the interaction between the next FSR reflective peak and the intended reflective peak. This is shown in figure 3.5 (a)-(c). Note that λ_{DM} refers to the dominant wavelength and λ_{SM} refers to the side peak wavelength. Ideally, there would be no interaction and the lasers SMSR would be dominated by the side peaks within the intended FSR reflective peak, however it is clearly observed that for 1000 μm lasers, that there is a large interaction with next FSR mode as the side peak difference jumps by a large amount just as there is a jump in the dominant wavelength. This difference is maintained for a small amount of current and then drops as the dominant wavelength settles, largely due to the previous FSR no longer lasing. For the 700 μm laser case, it is clearly seen that there is an interaction between the next FSR, however a full jump to this wavelength never occurs. Interestingly the two bluest lasers seem to interact with the second FSR, but the main lasing peak is still maintained at the intended peak. Overall, it is seen that with increasing current, for the bluer lasers the SMSR seems to be dominated by the next FSR modes in the red direction, which is expected as the laser temperature is increasing and is thus shifting the gain spectrum peak towards those reflective peaks. As for the 400 μm, there seems to be minimal interaction with the next FSR modes except for the bluest laser. This is likely due to the fact that this device does not have enough gain to significantly interact with the next FSR reflective peaks. Overall, for all laser lengths it is seen that the redder devices seem to have a smaller or negligible interaction with the next FSR reflective peak with respect to increasing current, likely due to the gain peak being too far from the next FSR peak to interact with it.

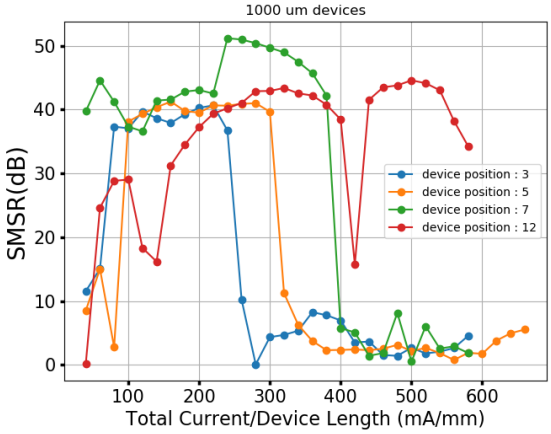

(a)

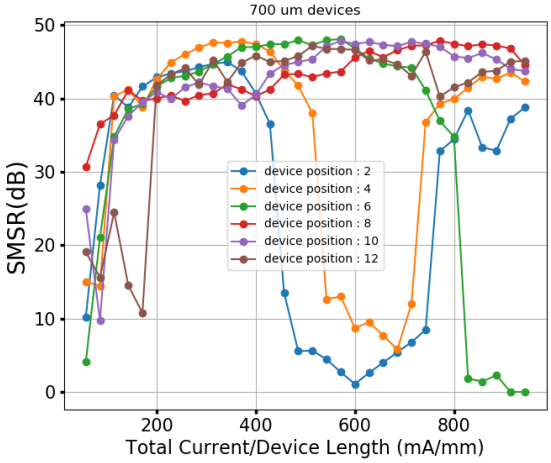

(b)

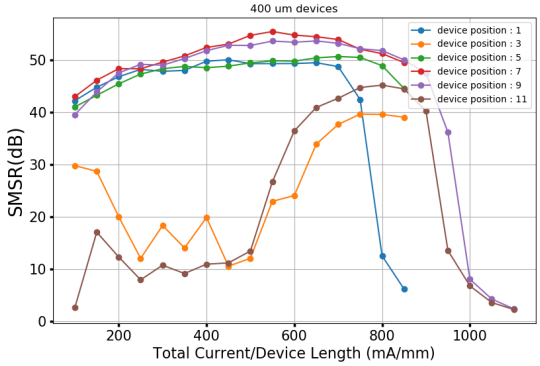

(c)

Figure 3.6: Variation of SMSR versus total current/device length for (a) 1000 μm (b) 700 μm and (c) 400 μm device lengths.

It is also interesting to see that even while using triple period gratings, the reduction in reflectivity of the next FSR reflective peaks is still not enough to eliminate its impact on the SMSR.

Finally, it is of significant interest to look at the overall SMSR, which is shown in figure 3.6 . For the 1000 μm devices it can be seen that as the wavelength jumps to the next FSR mode, the SMSR drops and remains below acceptable levels ($\leq$30dB). The only exception being the reddest laser of the array, where it maintains an acceptable SMSR for the entire range except for one instance. For the 700 μm case, this behaviour is also observed for the two bluest devices. As their interaction with the next FSR occurs, the SMSR drops below acceptable levels, however after a high enough current is injected into the laser the SMSR seems to recover. Redder lasers do not seem to exhibit this behaviour with their SMSR remaining mostly above 40 dB across the entire tuning range. Then, 400 μm devices seems to exhibit good SMSR across their entire tuning range except for two lasers exhibiting somewhat poor SMSR at the beginning of the tuning range. This would then suggest that the 400 and 700 μm devices are a clear choice for our athermalisation measurements, however, this will be further analysed in the next section.

3.3.1 Threshold Examination

In the previous subsection, spectral characteristics in terms of wavelength and SMSR were carried out via linear changes in current density across the device. Based on these measurements it seemed that 400 μm devices exhibit the most consistent, and favourable performance out of the three available device sizes. However, this only takes into consideration the input power part of equation 3.4. It is also necessary to considering the threshold part. This is particularly needed as all of these devices were operated at an ambient temperature of 20 ^{o}C and therefore they required very high current densities to achieve high self-heating. In reality, an athermalised laser would operate at much higher ambient temperatures and as such, it would not be operating as such high current densities. It is then necessary to examine threshold

characteristics of these lasers for full optimisation. We chose the best case scenario for these measurements, which are redshifted lasers (ref. [55]) and did a standard LIV measurement, which passes equal current density into each laser section starting from 0 at differing temperatures. The results are shown in figure 3.7. As can be seen, expected LIV behaviour occurs, with threshold increasing with increased ambient temperature, with there being an increase in output power with respect to increasing current, with some kinks being observed due to mode-hops. The LIV for 80 ^{o}C of 400 μm devices was not included as the device did not reach threshold at any injection current. It is then clear, that in terms of threshold, the 700 and 1000 μm devices are clearly superior. Thus, 700 μm devices then are a clear choice for our athermalisation measurements as they have better performance in terms of spectral characterisation and threshold.

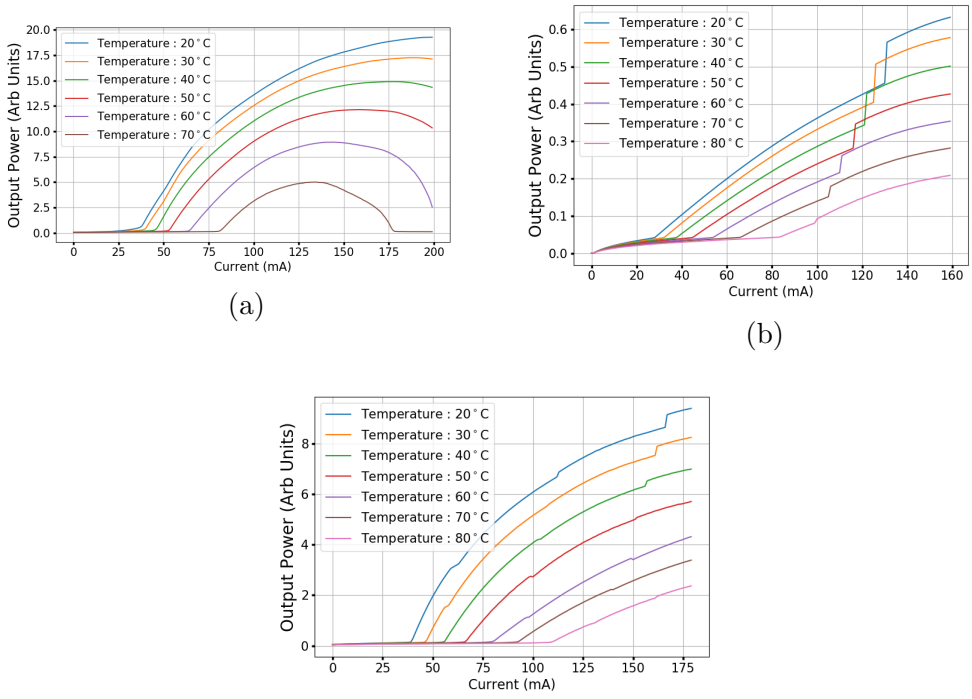

Figure 3.7: LIV characteristics for (a) 400 μm (b) 700 μm and (c) 1000 μm device lengths. Non-linearity due to temperature effects is clearly observed.

3.4 Optimisation in terms of Wavelength Detuning for athermal operation

In the last section, measurements were carried out on devices of differing length to determine the optimum device length for high injection current, low ambient temperature operation. It was shown that devices of total length of 700μm had optimal performance in terms of SMSR and remaining within their intended mode. Preliminary measurements also suggested that devices with redder wavelengths had increased performance while operating under these conditions. Here, we will investigate the changes in laser parameters with respect to the device wavelength. An optimum detuning (difference between reflective peak wavelength and gain spectrum peak wavelength at ambient temperature) will be found.

The devices were tested on a setup shown in figure 3.2. The lasers were contacted and biased at 100 mA into the gain and grating sections. The SOA section was provided with 30 mA of current, which is well above the SOAs transparency. A TEC was used to sweep temperatures from 20 to 100 ^{o}C in 10 ^{o}C intervals to simulate various ambient temperatures, and if FSR mode hops are approached the temperature steps are reduced to show the transition between FSR modes.

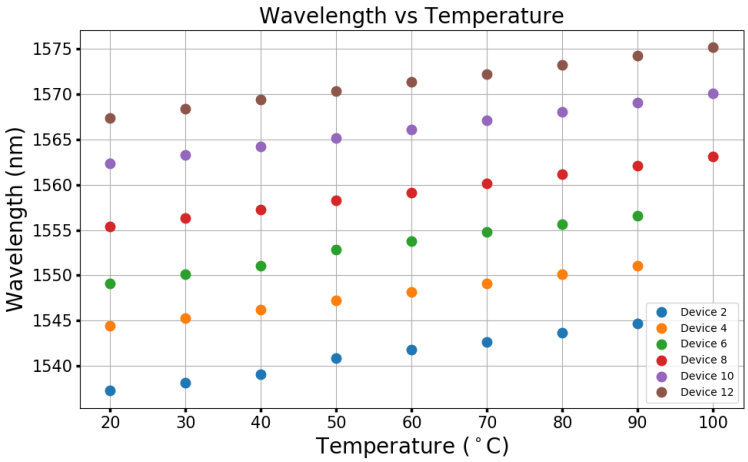

Figure 3.8: Thermal tuning of our triple period laser array. It is capable of covering most of the C-band.

The wavelength versus temperature relationship for the triple period array is shown in figure 3.8. Clearly we can see that there are no discontinuities in wavelength and the tuning behaviour is linear with temperature. This is a result of the suppression of the adjacent FSR peaks. In fact, the devices never mode hop to the adjacent FSR modes and instead fall below threshold if the temperature is too high. The observed trend is that redder wavelengths operate to higher temperatures. This is due to the misalignment of the gain spectrum peak and the Bragg reflective peak, which is referred to as detuning. This has been demonstrated before in [55], however the impact of detuning on SMSR was not shown and hence is investigated here in figure 3.9. Measurements recorded the SMSR of the peaks within the intended reflective peak (local SMSR) range, which was done using a short span and also recorded the overall SMSR (global) using a wide span on the OSA. This was done because the global SMSR also includes lasing peaks from the next FSR while the local SMSR does not. This difference in SMSR is here defined as the SMSR penalty. The effect of the next FSR modes on SMSR is typically significant while using high-order gratings due to a low FSR and hence, the impact of this is important to investigate. As seen in figure 3.9, local SMSR is observed to be very high at ambient temperatures and decreases with increasing temperature. However, local SMSR of bluer lasers is observed to be lower, as seen in figure 3.9(d) and it also decreases more rapidly than lasers with more red-shifted emission, with the change of SMSR over the thermal tuning range being plotted as SMSR loss (see figure 3.9(e)). Average wavelength here designates the central wavelength within the tuning range. This variance in SMSR is due to the gain spectrum redshifting with increased ambient temperature, providing more gain to red wavelengths with increasing temperature.

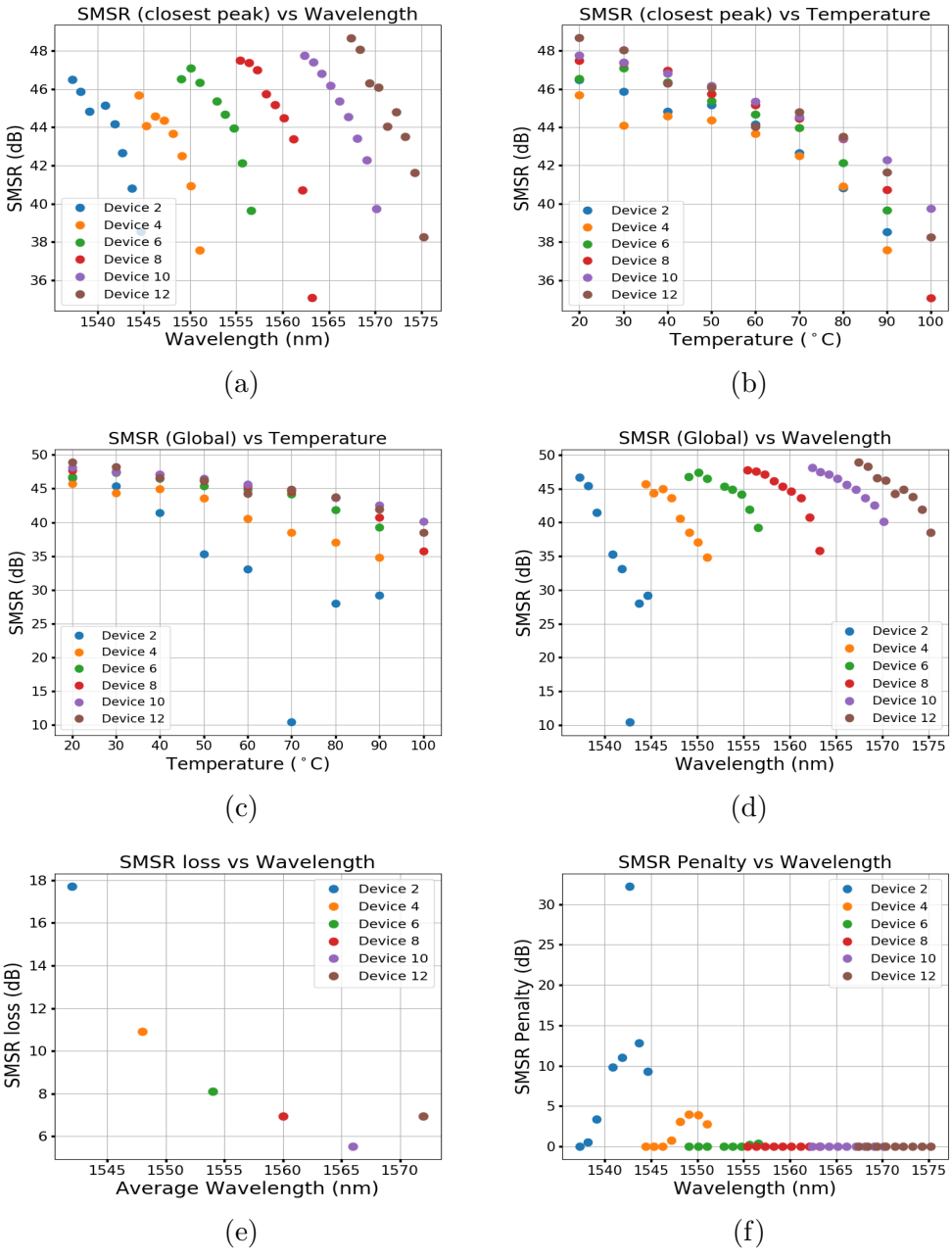

Figure 3.9: (a) SMSR of the closest peak vs Wavelength (b) SMSR of the closest peak vs Temperature (c) Global SMSR vs Wavelength (d) Global SMSR vs Temperature (e) SMSR loss vs Average Wavelength over tuning range (f) SMSR Penalty vs Wavelength. All for triple period grating devices.

This is shown as increased stability of the SMSR for red lasers, with the

highest stability observed at around +(20-25) nm away from the material gain peak. Past this point the benefits of detuning appear to diminish. Furthermore, when observing the global SMSR, it can be seen that blue end lasers experience a significant amount of mode competition from the next FSR. This is not the case for lasers past approximately 1555 nm. The difference between global and local SMSR (if detrimental) is defined as SMSR penalty and is plotted in figure 3.9(f). Additionally, the effect on output

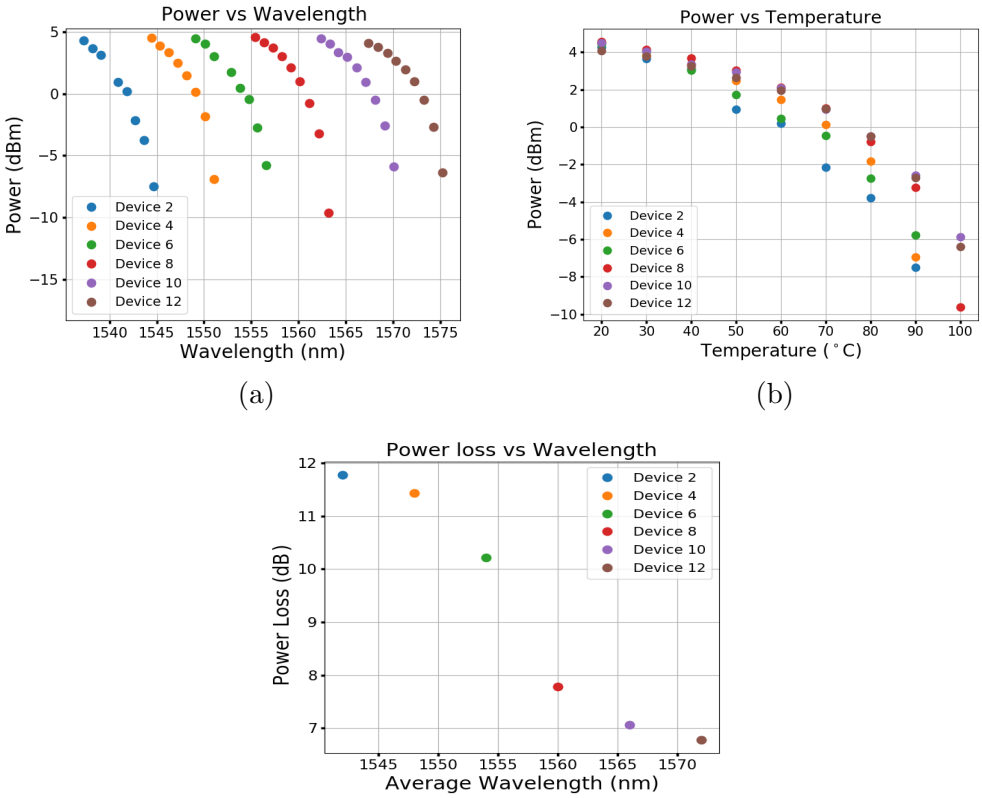

Figure 3.10: (a) Power vs Wavelength (b) Power vs Temperature (c) Loss in Power over the thermal tuning range vs Average Wavelength. All for triple period grating devices.

power versus detuning was also investigated, which is a first for simple, ridge waveguide lasers operating within the C-band. Looking at the output power data in figure 3.10, there is a typical relationship of decreasing power with temperature, with the total loss in power over the tuning range plotted in

3.10(c). This is due to increase in leakage current and non-radiative recombination at higher ambient temperatures. However, it can be seen that redder emitting devices maintain their output power more steadily(see figure 3.10(c)). It should be noted that both figure 3.9(e) and 3.10(c) consider only the changes of the power/SMSR of the devices from 20 to 90 ^{o}C as blue-end devices (number 2,4 and 6) went below threshold at 100 ^{o}C. It can be clearly seen that the general trend suggests redder wavelengths lose less power when temperature is increased, however the benefit of additional detuning seems to diminish for redder emitting devices. This suggests that past a certain point there is no additional benefit in detuning the laser further, which seems to be around 25 nm, which can be contrasted with a similar result derived for Mid-IR lasers in reference [56]. In the lasers studied in this reference, there is a benefit to have a detuning of up to +250 nm.

3.5 A more in-depth look at the athermalisation condition

In the last section, measurements were carried out on devices with a length of 700 μm, and it was determined that a device which exhibited a detuning of approximately +20 nm was the best performer in terms of maintaining its SMSR and output power as temperature varied. These measurements were all based on the assumption that by passing equal current density into the laser, and thus input power, and linearly varying it we then would acquire the largest athermal range. While this assumption is largely true, it does not take into consideration that the laser has two tuning sections and not just one. There may be scenarios where it may be needed to have the two currents be different, such as athermalising several wavelengths on a single device as demonstrated in section 4.3. The input power part of equation 3.3 can be easily modified to just use the limiting section (whichever section heats up the least will then limit the athermalisation range), however threshold characteristic will change more drastically. As discussed earlier, for our devices, the gratings do also experience gain, however the losses are

also far larger, so the impact on threshold will be different based on the input current to each section. Traditionally, threshold is measured with equal current density into each section, and such a measurement for a 700 μm device that has been significantly redshifted is given in the previous section in figure 3.7. Change in threshold with respect to temperature, along with the characteristic temperature and current are more clearly plotted in figure 3.11.

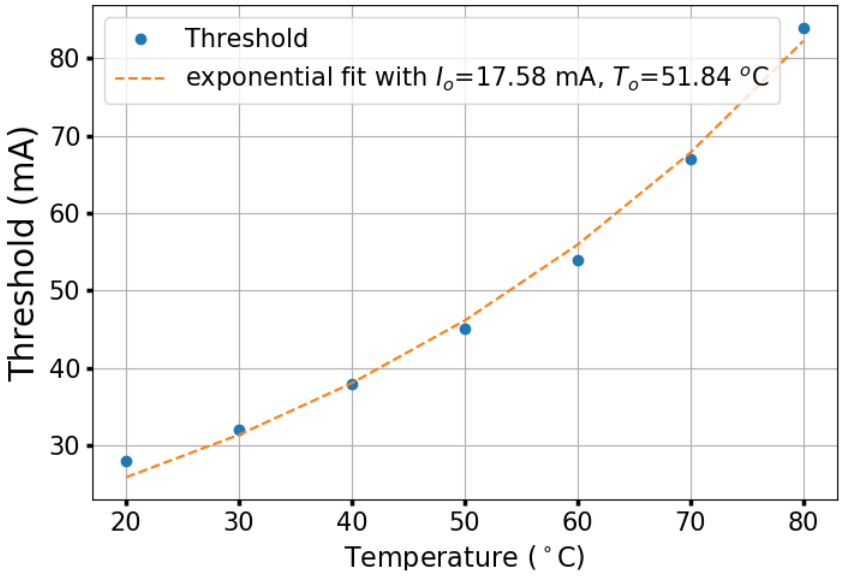

Figure 3.11: Threshold versus temperature characteristic. A fit using the standard exponential expression is performed and values of I_0 and T_0 are obtained.

The measured values of T_o and I_o are standard for a significantly redshifted device, albeit maybe even a bit low, particularly for T_o. As mentioned earlier, this single current approach to measuring threshold is not valid for a two section device, as the grating is far more lossy than the gain section, thus providing a larger current density to the gain section should provide a lower threshold. To investigate this, we have swept the gain and grating currents and measured output power. The resulting maps can be seen in figure 3.12.

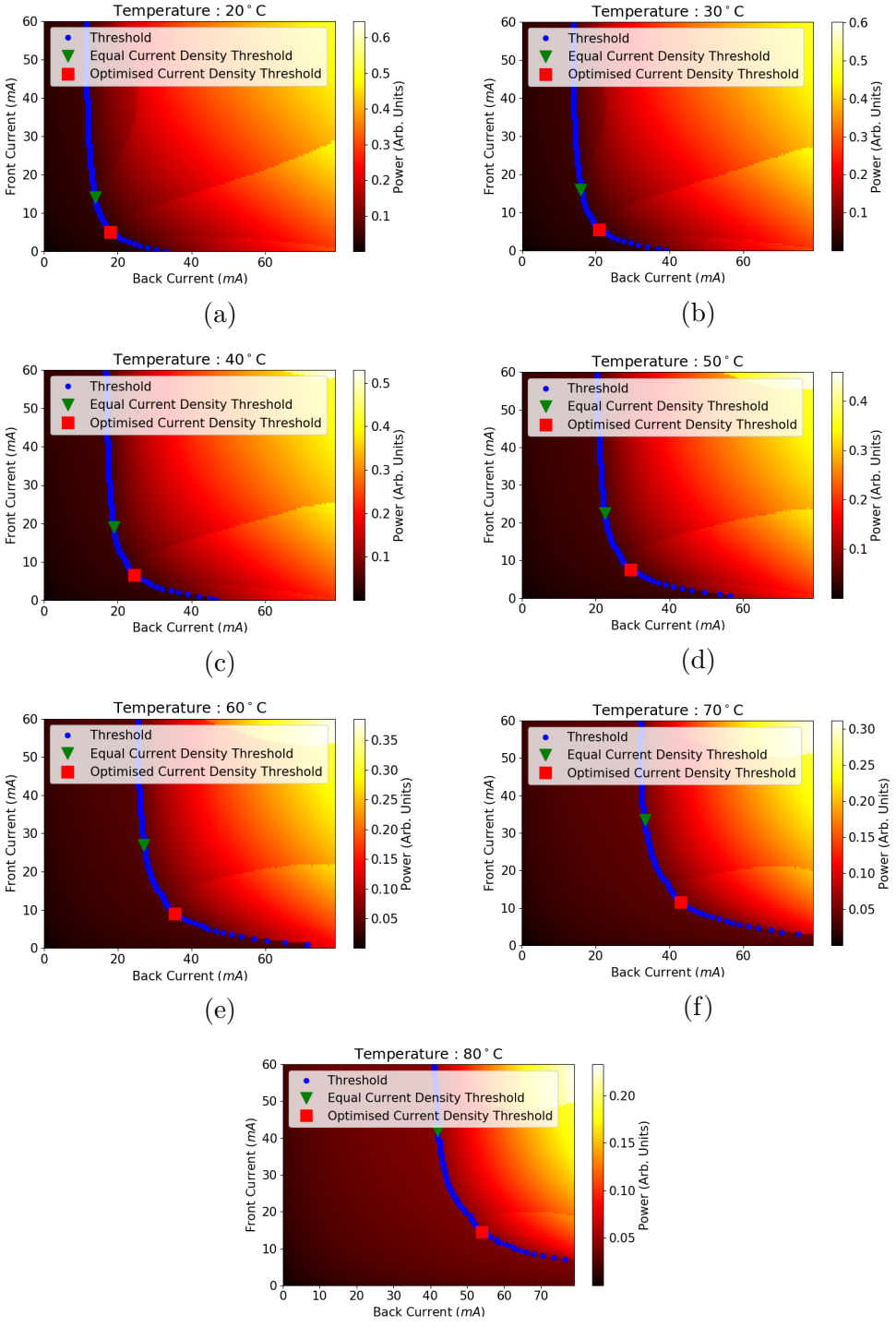

Figure 3.12: Power Maps while the Back (Gain) and Front (Grating) currents are swept at (a) 20 (b) 30 (c) 40 (d) 50 (e) 60 (f) 70 (g) 80 ^{o}C

Threshold which is achieved using the regular, equal current density approach is highlighted using the green triangle, while the lowest current required to achieve threshold is denoted by a red square on the map. As can be seen, gain current has a significantly larger impact than grating current, in fact for lower temperatures grating current is not required at all to reach threshold, however this is not the case at elevated temperatures. The lowest possible threshold then uses an increased gain current and a lower grating current, presumably the grating current is purely there to overcome the grating losses.

Figure 3.13(a) then compares the traditional threshold measurement to the optimised measurement. Clearly, there is a significant improvement observed. The value of T_o is observed to be slightly higher (however this may be within the margin of error), while I_o is observed to be significantly lower. The difference between the optimal threshold and traditional threshold for each temperature is plotted in figure 3.13(c). It can be seen that this difference increases in absolute magnitude, however the percentage difference remains relatively constant. This is due to both currents rising exponentially, so the difference between them will rise, however their ratio will remain the same. Figure 3.13(c) shows how each of the currents contribute to the overall current linearly. It can be clearly seen that the gain currents contribution is significantly higher. An exponential fit of $I = I_o \exp(T/T_o)$ was used for both fits, and seeing as $T_{gain,o} \approxeq T_{grating,o} = T_{opt}$, then we should be simply able to compare the amplitude of each currents impact on threshold via,

$$I_{frac} = \frac{I_{grating,o} \exp(T/T_{opt})}{I_{gain,o} \exp(T/T_{opt})} = \frac{I_{grating,o}}{I_{gain,o}} = 0.257 \tag{3.7}$$

Thus, the gain current has an approximately four times greater impact on threshold, when compared to the grating while using the values from the fit.

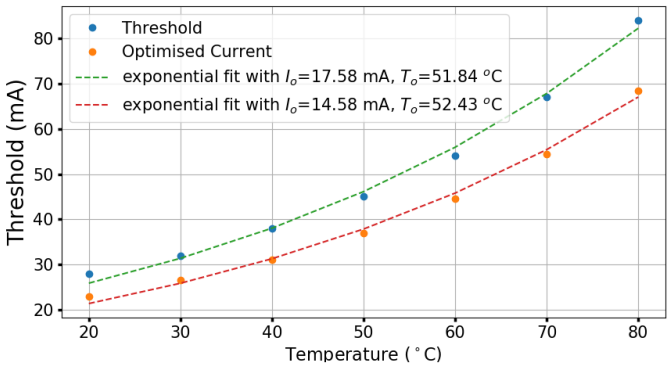

(a)

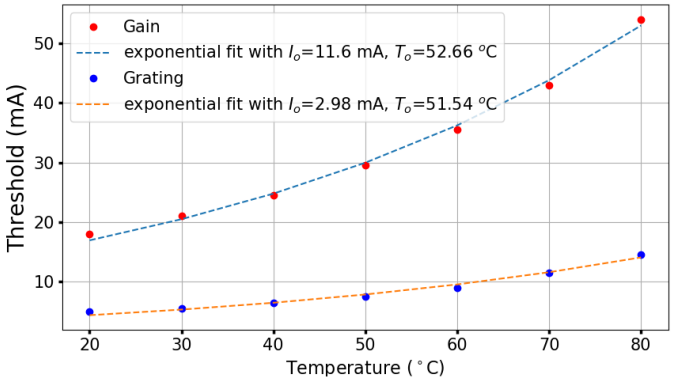

(b)

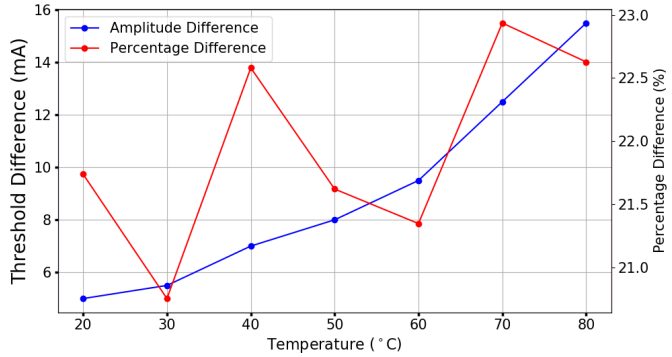

(c)

Figure 3.13: (a) Threshold comparison for the standard and optimised method (b) Threshold scaling for the gain and grating sections respectively and (c) The difference between the standard and optimised method.

While not perfectly constant, it is observed to be relatively so from the experimental data as shown in figure 3.14.

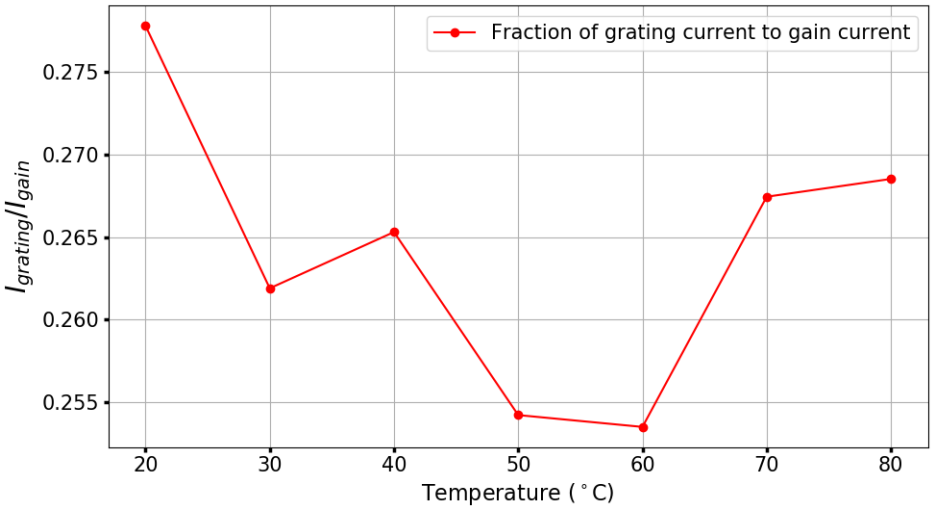

Figure 3.14: Experimental comparison of the impact of grating current to gain current for achieving optimised threshold.

This result is significant as this suggests that for these 700 μm lasers, the gain current will be the dominant current for the threshold component of the athermal range equation, assuming that $4I_{grating} \geq I_{gain}$. For large range athermalisations it is of best interest to have $J_{grating} \geq J_{gain}$, where J denotes the current density. Considering the length of the gain section is approximately twice that of the grating, we have $2I_{grating} \geq I_{gain}$ leading to the the aforementioned condition holding for practically every wide range athermalisation. Then, for a two section device, the athermalisation equation can be rewritten as,

$$T_{ar}(I_{lim}) = Z_{th,lim}R_{lim}I_{lim}^2 - Z_{th,gain}R_{gain}I_{0,gain}^2 \exp(2\frac{Z_{th,gain}I_{gain}^2R_{gain} + T_a}{T_{0,gain}})) \tag{3.8}$$

where I_{lim} is the limiting current, or rather the current of the section which induces the least self-heating. R_{lim} is the resistance of the respective section and $Z_{th,lim}$ is the thermal impedance of such section.

3.6 Conclusion

First, it was shown that high-order slotted semiconductor lasers with our grating parameters can be tuned to very high injection currents at ambient temperature while staying within their intended FSR mode and maintaining good SMSR. In particular, devices with total length of 700 μm have shown exceptional performance.

Secondly, these devices were then tested at relatively low injection currents with varying ambient temperature and were shown to have good performance in terms of output power and SMSR. In particular, for the first time it is shown that laser SMSR is improved with wavelength detuning with increasing ambient temperature. It is shown that lasers with a wavelength detuning of +(20-25) nm have shown the best performance at high temperature. The results of this chapter then suggest that for optimum wide range athermal performance a device of total length of 700 μm and a wavelength detuning of +(20-25) nm must be used.

Finally, we had a more in depth look at the athermalisation condition, in particular for devices which contain two sections. Due to this investigation, it was discovered that threshold for our devices can be significantly lowered. This then leads to the conclusion that the gain section is dominant for the threshold part of the athermal range equation.

Chapter 4

Steady State Athermalisation

4.1 Introduction

In the previous chapter an optimal device for wide range athermal operation is selected. In particular, it was found that a device of total length 700 μm, with an approximate redshift of 20 nm in its reflective Bragg peak with respect to the material gain peak was the optimal choice. In this chapter, this device is athermalised and the variance of device parameters while under athermal operation are examined.

In particular, changes in these parameters can have severely detrimental effects on WDM systems and it is crucial to maintain them above a certain level. Three important parameters which are crucial to WDM are investigated, namely wavelength has to be maintained to within $\pm$12.5 GHz (0.1 nm), requiring very precise current control to achieve this. Secondly, SMSR must be maintained above 30 dB, which becomes problematic as the device approaches threshold currents at higher ambient temperatures. Finally, output power will inevitably decrease with decreasing injection currents and increasing ambient temperature. It is desirable to maintain a constant output power and a method to do so during athermalisation is investigated. As athermalisation is a solution for an energy problem, wall plug efficiency is also investigated. These results are presented in sections 4.2.1 and 4.2.2.

For WDM systems, it is necessary to be capable of covering the C-band.

For DFB and DBR devices, this is typically achieved using laser arrays. However, each laser within the array must be capable of producing several wavelengths, and thus for athermal WDM, several of these wavelengths must be athermaliseable. This can be tricky as different currents will produce different wavelengths and may result in varying athermal range. This is investigated in section 4.3.

Finally, as a consequence of athermalisation of our devices, a thermal impedance measurement has been developed. This is an important device parameter used in optimisation, and thus this measurement is investigated. Several single grating devices of varying lengths were measured, which has led to a thermal impedance per device length which is consistent among all of our devices based on the same material.

Then, within this chapter, a laser diode is athermalised and the variance of the lasers parameters is shown in section 4.2. Multi-wavelength athermalisation is then performed on the same device, with detailed analysis performed on parameter variation and change in athermal range in section 4.3. Finally, a new method for measuring thermal impedance is then developed in section 4.4. This chapter demonstrates that our simple devices are capable of being used in high performance athermal WDM networks.

4.2 Single Channel Athermalisation

4.2.1 Wide Range Athermalisation

Since the results of the previous section suggest that devices with redder wavelengths behave more favourably at elevated temperatures, we chose a device on the red end of the laser array for our athermalisation studies. A tuning map of our laser taken at 20 ^{o}C is presented in figure 4.1 with the currents used for athermalisation plotted in black.

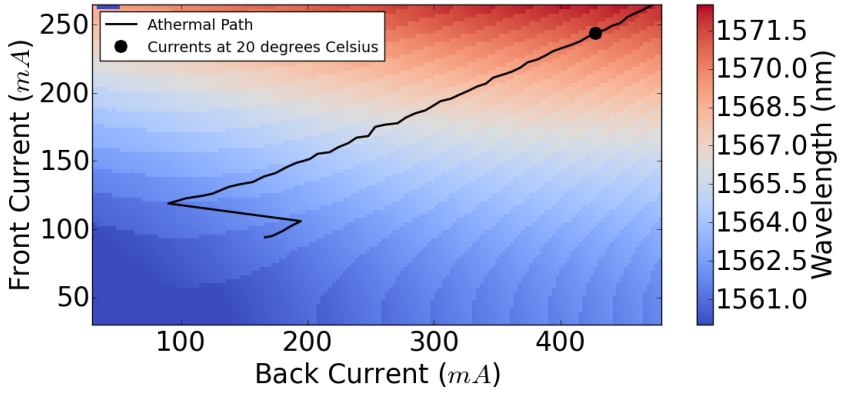

Figure 4.1: Tuning map of our device taken at 20 ^{o}C. The black line denotes the athermal path, and the black point shows corresponding currents at 20 ^{o}C.

As can be seen, at low currents(<100 mA in each section) the free carrier plasma effect tuning is present (the saddle point near 100 mA for back and front currents shows the region where carrier and thermal effects are equal), however at any reasonable current the thermal tuning is dominant. The athermalisation results are shown in figure 4.2.

We traverse the path as shown in figure 4.1 by slowly changing the TEC temperature and adjusting the currents to the front and back sections. The wavelength is maintained to within ±0.4 GHz or 0.003 nm via precise tuning of current, which is well within the required maximum spectral excursion requirement of ±12.5 GHz or 0.4 nm for 50 GHz spaced channels on a TWDM grid [57]. This resolution is higher than the OSA used in the previous mea-

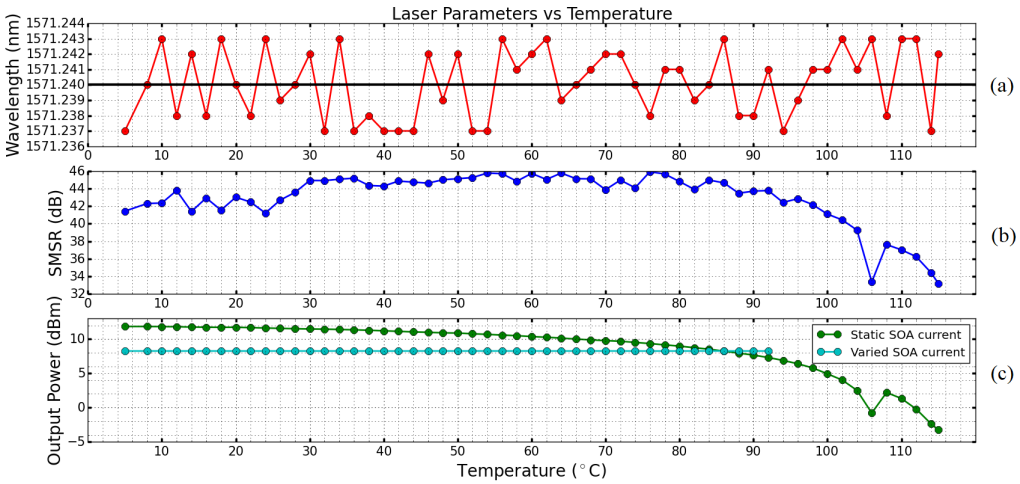

Figure 4.2: (a) Wavelength vs Temperature. The black line denotes centre of TWDM channel 8. (b) Wavelength vs SMSR. Note the decrease in SMSR at high ambient temperature. (c) Wavelength vs Power for both static and varied SOA currents. Note how output power can be stabilised from 5 to 94 ^{o}C.

surement, however for the measurements presented here, the wavelength was obtained from a HP 86120B wavemeter with a resolution of ± 2 pm , while the SMSR was obtained using the OSA. It is seen that the SMSR was maintained above 40 dB from 5 to 102 ^{o}C, after which it remains above 30 dB, which is also within TWDM requirements. Output power for this athermalisation was measured using a bare photodiode to get the absolute power and remains relatively stable until it reaches about 80 ^{o}C, decreasing more rapidly from that point onwards as the TEC temperature is increased. This is because as ambient temperature is increased, currents in each tuning section must be reduced to compensate for the increase in temperature, however this leads to a reduction in carriers for lasing and hence lower output power. An increase in output power is observed at 108 ^{o}C, which is due to a discontinuous mode hop. This discontinuous mode hop was necessary as the device was approaching threshold, hence an increase in gain current was provided. As no such discontinuities are observed before this point, it is clear that the tuning in the range 5 to 106 ^{o}C is continuous. Furthermore, output power is maintained above 0 dBm in all but the last point in the continuous range.

This output power variation can also be reduced to less than ±0.005 dBm by varying the SOA current as shown in figures 4.2(c) and 4.3.

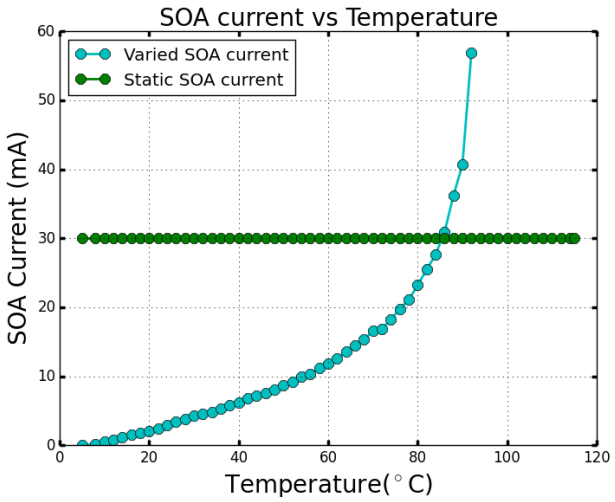

Figure 4.3: SOA currents for either maintaining static power or static SOA current.

As observed in figure 4.2, the decrease in power seems to increase more drastically with increasing temperature. In turn, this will cause a sharper rise in SOA current at higher temperatures and will lead to the SOA saturating relatively quickly, which occurs at ≈60 mA which is the SOA current at 92 ^{o}C. Past this point the loss in output power is too large and was not compensated. One possible solution to stabilising power within the entire range is to redesign the SOA, such as increasing the length of the SOA section so it can provide a larger amount of gain over a larger temperature range, however this was not performed for this study.

The athermalisation results shown here, in terms of the small wavelength variation and wide temperature range are the best achieved to date. They show that careful control of currents that flow to the device from monitoring temperature changes allow for very precise control on the laser wavelength. This result has the potential to influence the range of applications where these lasers operate in temperature varying environments. Currents used for the athermalisation are displayed in figure 4.4. As mentioned earlier, high

currents are needed at low temperatures to achieve high self-heating and hence a wide athermal range. Additionally, only one large discontinuity in current is observed proving that the tuning in the range of 5 to 106 ^{o}C was indeed continuous.

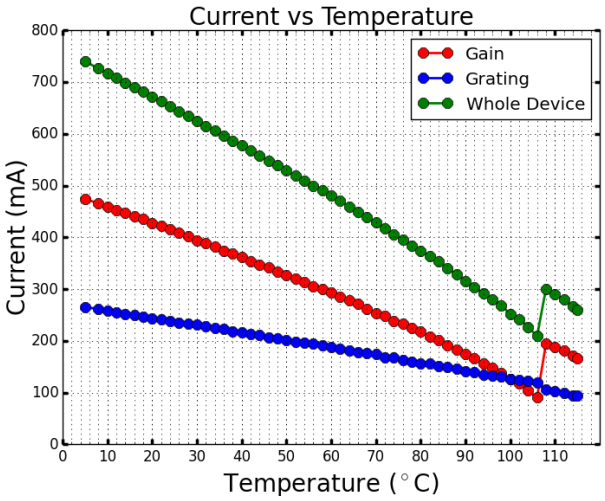

Figure 4.4: Currents used to achieve athermal performance.

Another measurement that was taken to further solidify this is input electrical power versus temperature which is shown in figure 4.5.

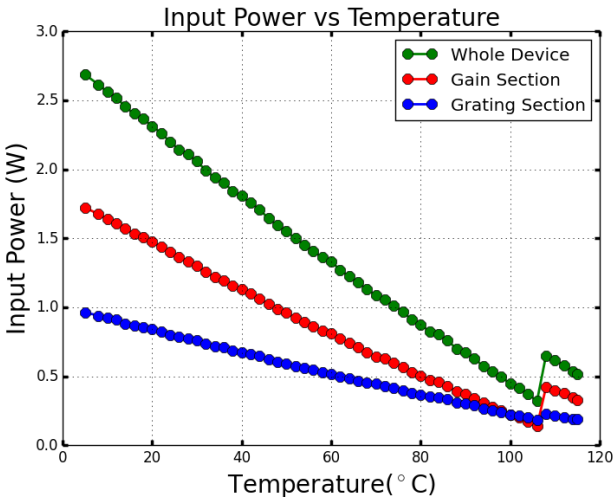

Figure 4.5: Electrical input power into our laser over the athermal path.

As discussed previously, temperature must remain constant for all-active devices within a mode during athermalisation, and so electrical input power must vary linearly to combat the changes in temperature. This linear relationship is observed in two parts within figure 4.5, suggesting that there are only two modes present during this athermalisation.

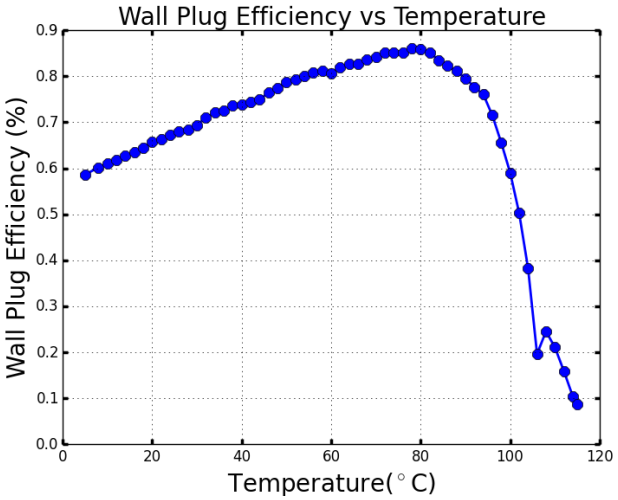

Figure 4.6: Wall Plug Efficiency over our athermal path.

Finally, the wall plug efficiency over the athermal range is shown in figure 4.6 and is observed to increase until approximately 80 ^{o}C, however from this point on it is observed to drop rapidly. This is because of a rapid decline in output power as a result of decreasing stimulated recombination past this point. Do note that the TEC was not included in the wall plug efficiency calculation as it was merely used to simulate various ambient temperatures. This performance is a 54 ^{o}C improvement over our previous work [58] while tuning continuously and a 20 ^{o}C improvement while tuning discontinuously, clearly demonstrating that choice of laser wavelength and length of lasing sections are important factors when designing lasers for athermalisation.

4.2.2 Athermalisation of different ranges for increased wall-plug efficiency

In the previous section, a wide range athermalisation was demonstrated. However, it was shown that the wall-plug efficiency of such athermalisation is relatively low (<1%). While wide range athermalisations might be desirable in several applications, this might not be the case in others. Thus, if a wide range athermalisation is not required then we could decrease the athermal range and improve wall-plug efficiency.

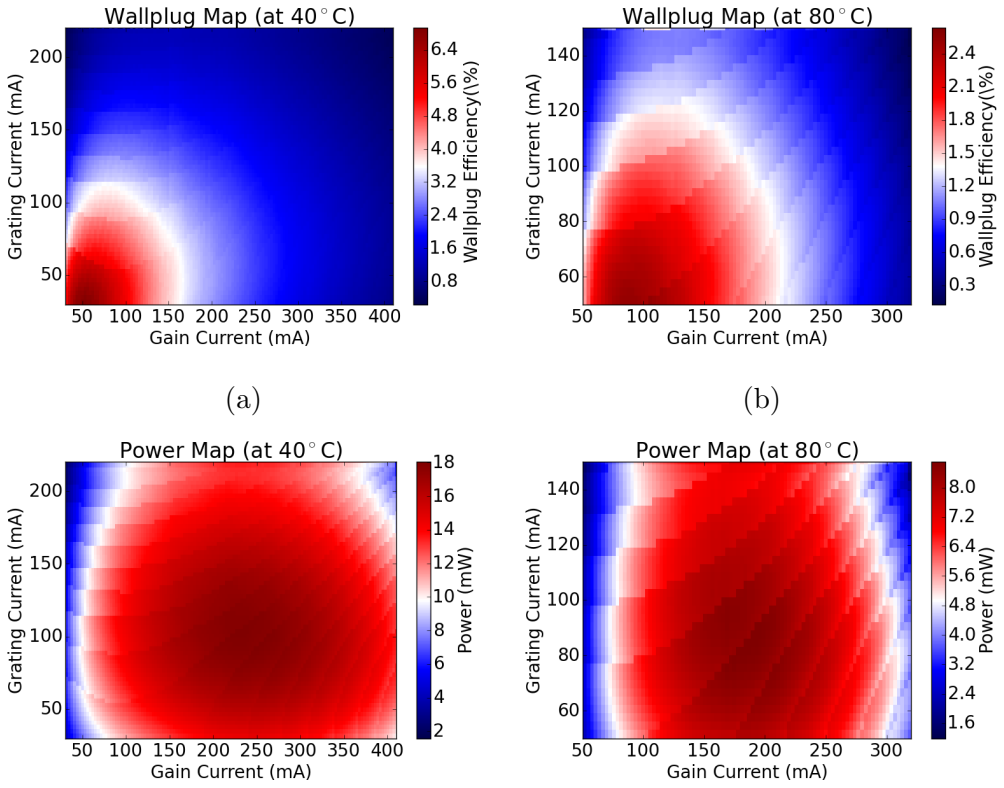

Figure 4.7: (a)-(b) Wall Plug efficiency maps for differing input currents into our device and (c)-(d) Power maps for differing input currents at 40 and 80 ^{o}C.

This is possible because as athermalisation range increases, so do the local operating temperatures as per equation 3.1. This then causes an in-

crease in Auger recombination, which results in decreased output power per milliampere of input current, reducing wall-plug efficiency. Then, to achieve maximum wallplug efficiency for a given athermal range, we must decide on the required range, and then start at the maximum wall-plug efficiency at the high temperature, and increase current towards our set point. We are thus required to acquire wall-plug efficiency maps at the elevated temperature, which are presented below. Power maps at these temperatures are also shown because as we are attempting to achieve good wall-plug efficiency, we are also attempting to obtain good output power as well, which would still be necessary for optical access networks. It is clearly observed that in both the 40 and 80 ^{o}C cases, wallplug efficiency is at its highest when at low currents, seeing an increase in wallplug efficiency with any decreasing current. However, output power appears to be highest at the median currents of the measured range, however it does not vary as significantly with current, as long as it is not in the very low current regime. Thus, we chose currents which were in the intermediate range, relatively low but still high enough to achieve sufficient output power as our starting point for the athermalisations, which both started at 40 and 80 ^{o}C respectively. The wavelength stability for both are shown below, with the wavelength stability of the previous sections athermalisation included for comparison reasons.

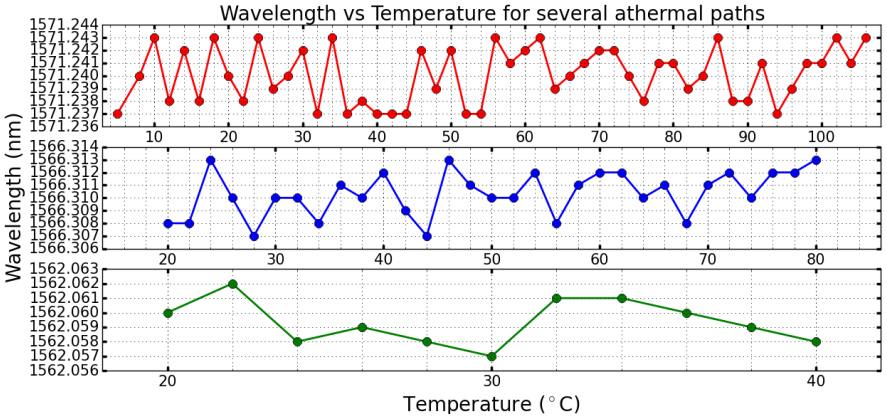

Figure 4.8: Wavelength stability of our laser while operated at different athermal ranges.

As observed, the wavelength stability remains to within $\pm$ 0.003 nm/0.4 GHz as with the previous athermalisation. The currents used are then shown in figure 4.9.

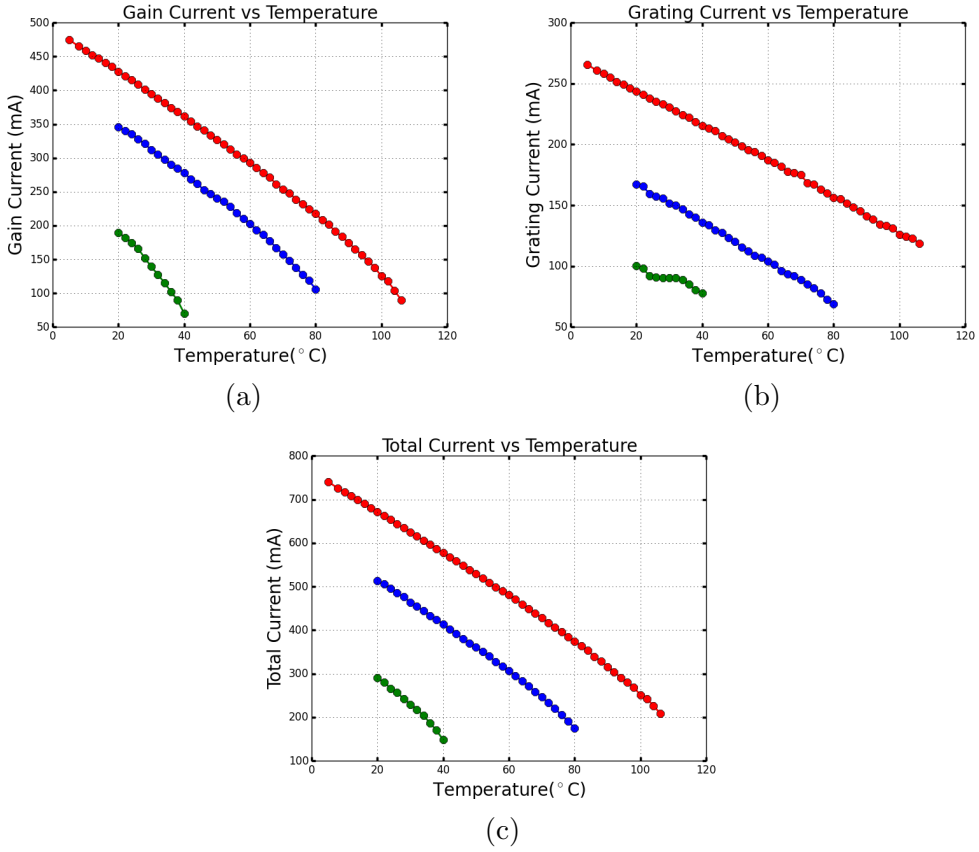

Figure 4.9: (a) Gain (b) Grating and (c) total currents for the differing athermalisations.

Expected behaviour occurs with decreasing current when temperature is increased. Clearly, less current is used for lower athermal ranges, which is a natural outcome derived from equation 3.4. The wall plug efficiency for each athermal path is given in figure 4.10. Increase in wall plug efficiency is then clearly observed for the two shorter paths, increasing with increasing temperature. This is due to a sharp drop in input power into a laser, with only a marginal change in output power.

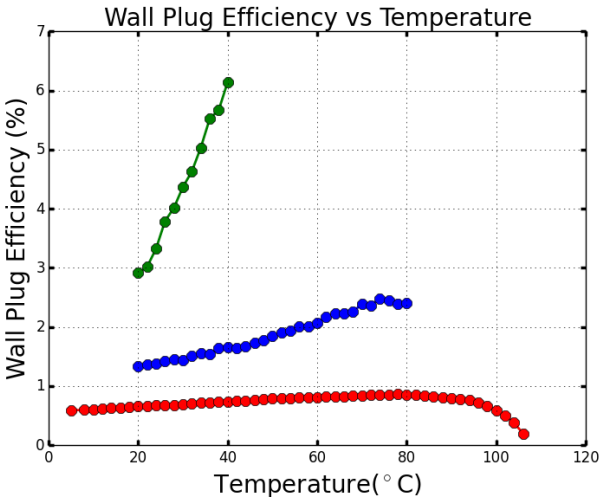

Figure 4.10: Wall plug efficiency of our laser over the differing athermal paths.

4.3 Multi-Channel Athermalisation

The measurements carried out in this section were done using the same setup as in the previous section. The main difference is that the TEC temperature in these measurements was adjusted in 10 ^{o}C increments instead of 2 ^{o}C except when a mode-hop was approached, at which point finer increments were used to obtain the maximum range of temperatures over which athermal operation is maintained. As mentioned earlier, the gain and grating currents were varied accordingly to maintain the athermalisation condition, while the SOA current was kept at a constant 30 mA, which is roughly the midway point between transparency and saturation of the SOA.

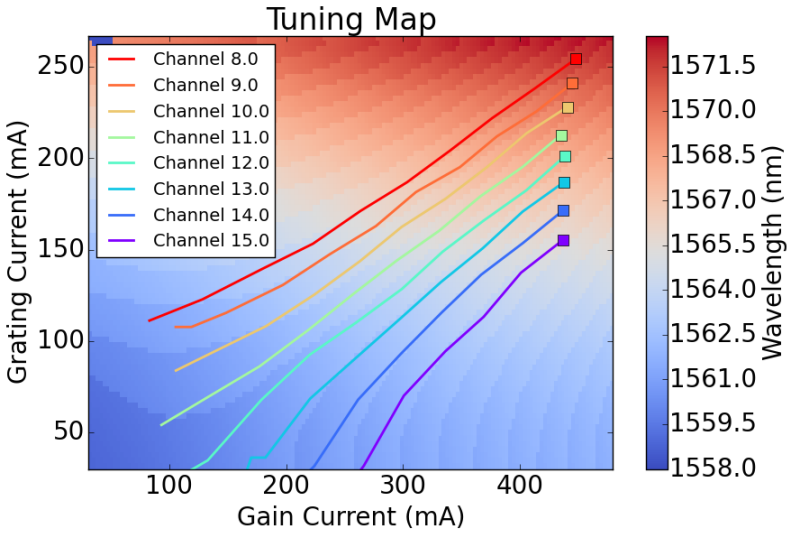

Figure 4.11: Tuning map of our device at 20 ^{o}C with athermal paths for 100 GHz channels shown.

The tuning map of the device at 20 ^{o}C is plotted in figure 4.11, with the shape of the map being a result of the asymmetric shift of the cavity modes with respect to the reflective peak. The currents used to achieve athermalisation for 100 GHz channels are plotted on the map. The squares are used to denote the start of the athermal path at 20 ^{o}C. We use this map to guide the athermal operation, by helping us choose a starting current and to avoid mode hops.

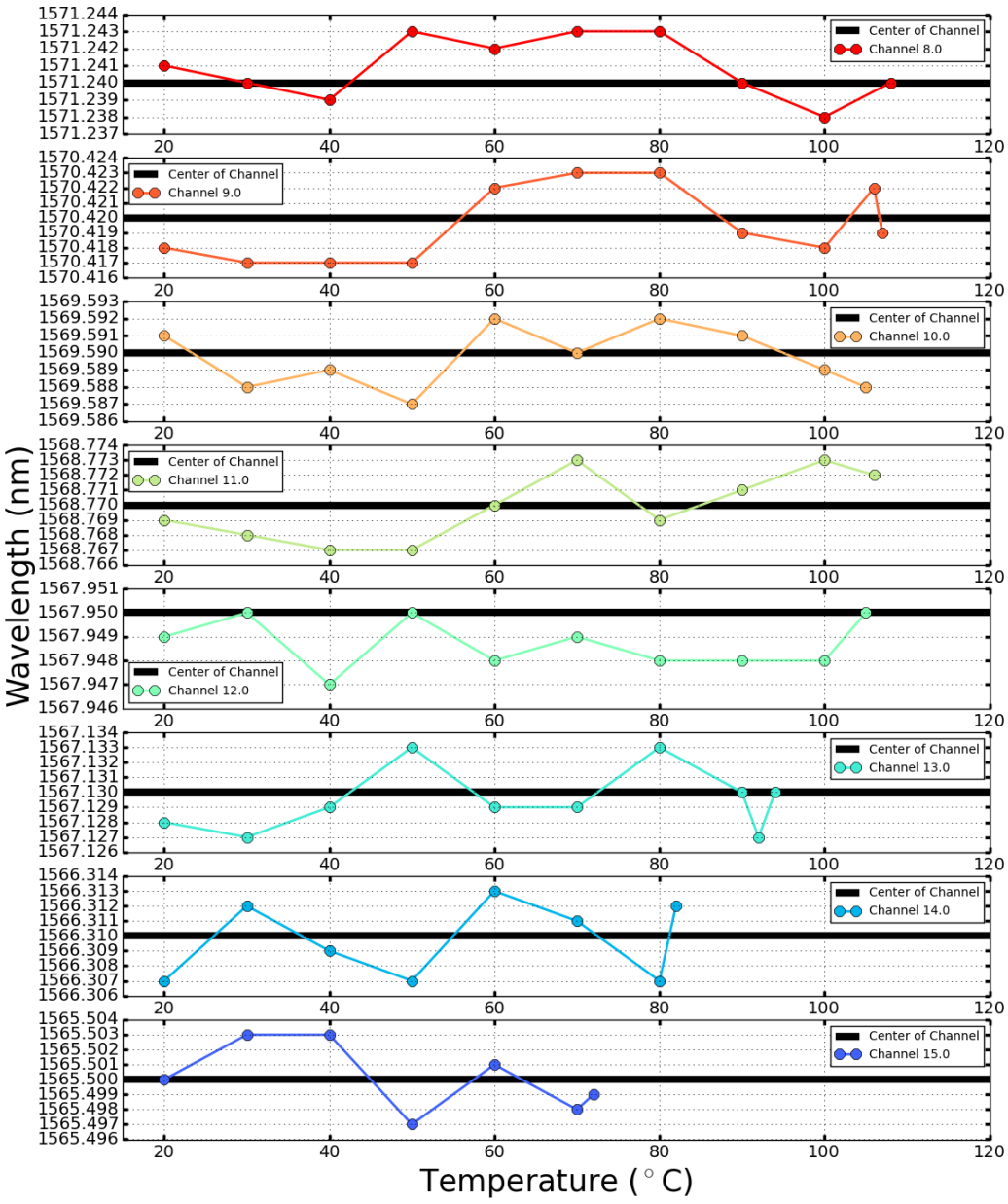

Figure 4.12: Wavelength stability of 100 GHz spaced channels. Note the increasing athermal range with increasing wavelength (from lower right to upper left).

Note, that the tuning map changes with temperature, this is why some of the paths appear to cross mode boundaries further along the path. Figure 4.12 shows the wavelengths for the 100 GHz spaced channels. It is observed

that the wavelength remains constant to within ±0.003 nm/± 0.4 GHz of the central wavelength. The athermal range can also be seen from these figures, but is better illustrated in figure 4.13.

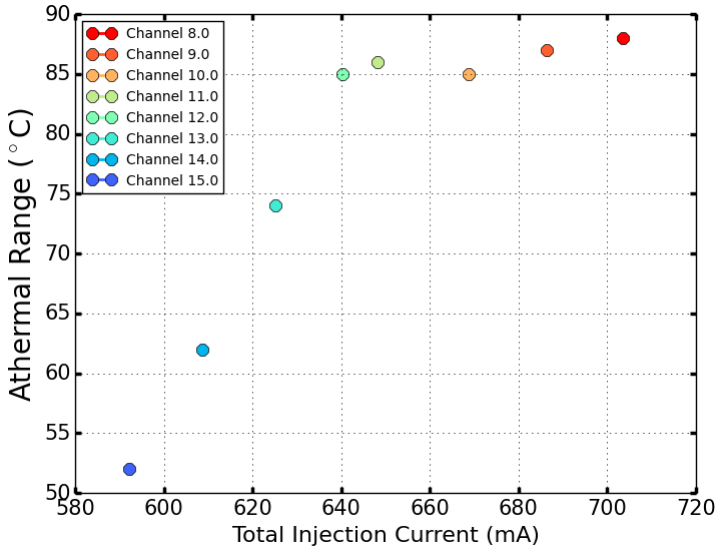

Figure 4.13: Athermal range of 100 GHz channels versus injection current at 20 ^{o}C. Note how the range saturates at high total currents.

Initially, there appears to be a linear rise in athermal range with increased current at 20 ^{o}C, however this effect seems to saturate. This behaviour can be explained by taking a closer look at injection currents into each device section given in figure 4.14 (a-c). From this figure, it is clear that there is not a large variation in gain current at 20 ^{o}C, aside from a small increase in gain current with increasing wavelength, which is negligible. The main difference between channels comes in the form of the grating current, as this varies by a significant amount between 100 GHz spaced channels and is responsible for the differences in athermal range. However, once a grating current of ≈200 mA is reached, this effect saturates and small differences to athermal range can be attributed to variations in gain current. This is because past 200 mA, the local temperature of the grating becomes significantly larger than that of the gain section and therefore, gain current becomes the limiting factor in the athermal range. This can be seen by the plot in figure 4.15.

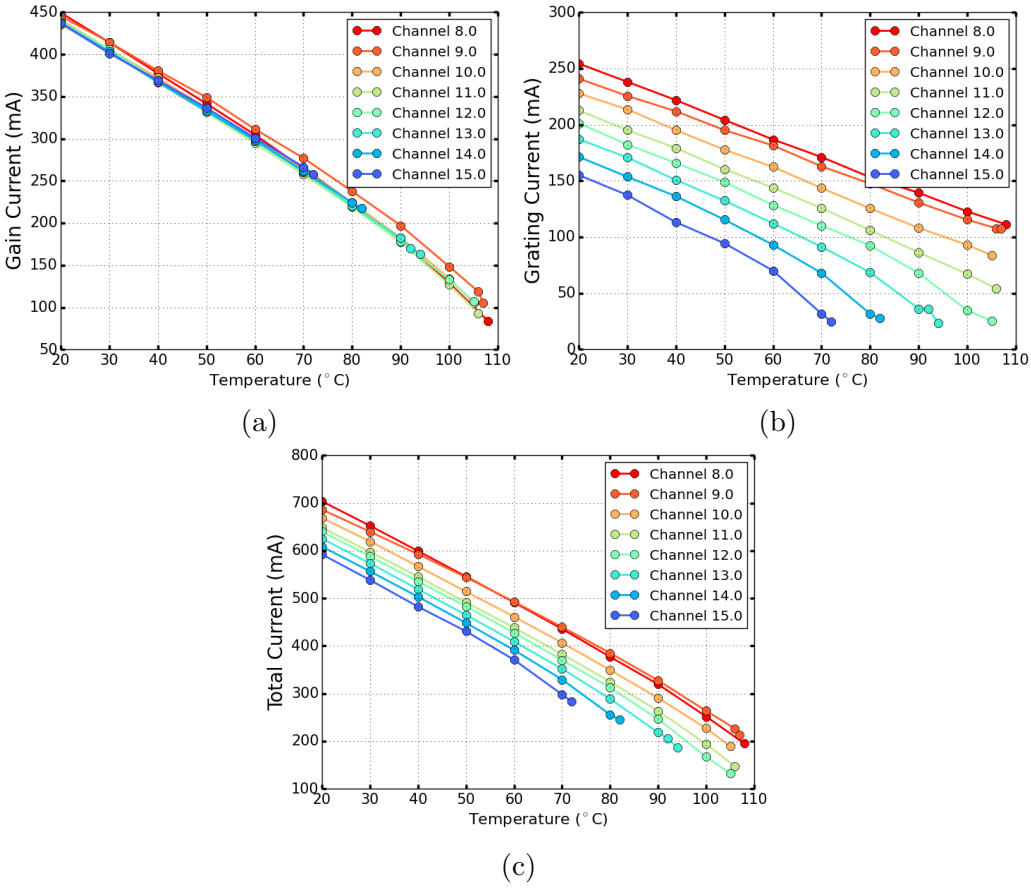

Figure 4.14: Variation of (a) gain, (b) grating and (c) total injection currents versus temperature over the athermal paths for 100 GHz spaced channels.

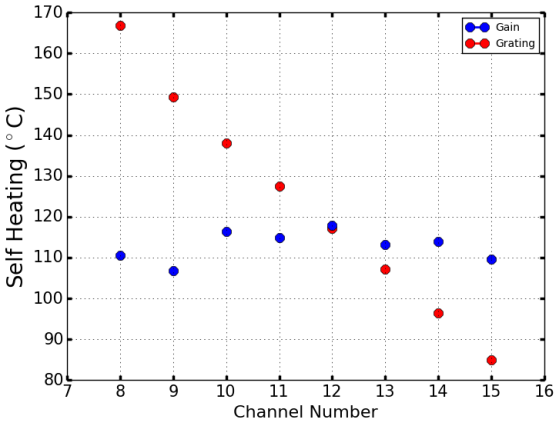

Figure 4.15: Self-Heating for each of the sections for a given WDM channel.

This plot is obtained using thermal impedance values recorded in reference [59], and from voltage measurements at a given current for each section. This then can be used to calculate input power which can be used to obtain average section temperature. Additionally, the increased athermal range seems to come with a reduced output power as shown in figure 4.16(a).

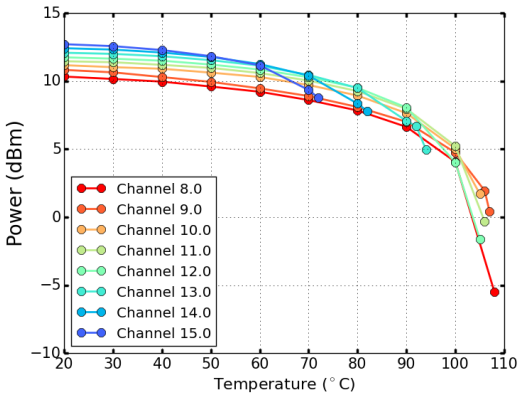

(a)

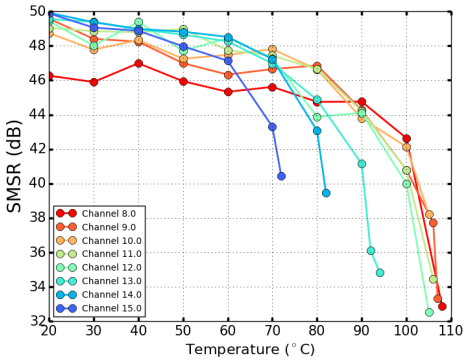

(b)

Figure 4.16: Variation of (a) output power and (b) SMSR and versus temperature over the athermal paths for 100 GHz spaced channels.

This can be compensated to some degree with the short SOA section, by varying the injection current into the SOA, but has not been studied in this set of experiments. The reduced power is due to shorter wavelength devices operating at lower local temperatures and hence, not suffering as severely from temperature sensitive effects such as leakage current and Auger recombination. Additionally, all channels exhibit a decrease in output power with

increasing ambient temperature, which is due to a reduction in carrier injection, reducing the gain provided to the main lasing peak and thus decreasing output power. Similarly, the SMSR is observed to decrease with temperature as shown in figure 4.16(b). A faster decrease is observed for shorter wavelengths which is due to them initially operating at lower injection currents, thus these wavelengths are closer to threshold than longer wavelengths resulting in a more rapidly decreasing SMSR with respect to temperature.

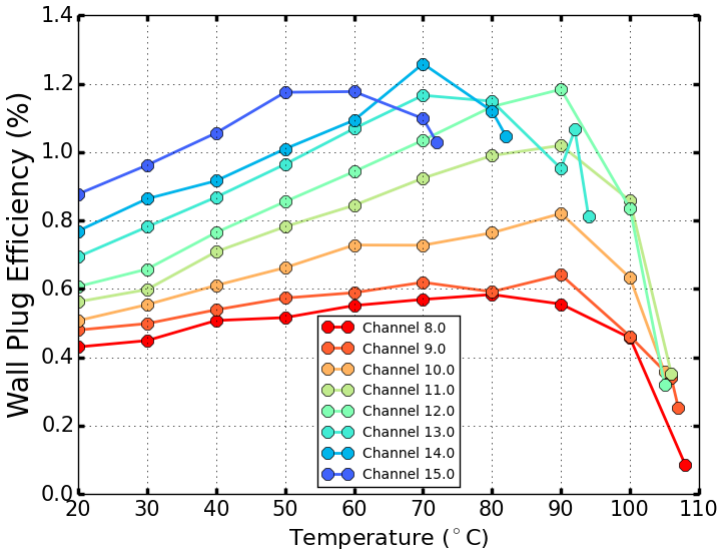

Figure 4.17: Wallplug efficiency versus temperature over the athermal paths for 100 GHz spaced channels.

Finally, wall-plug efficiency, which is the ratio of output power versus electrical input power into the laser, was recorded for each channel and this result is shown in figure 4.17. The input power into the TEC is excluded for this measurement as the TEC is only used to simulate changes in ambient temperature. It is observed that wall-plug efficiency decreases with decreasing channel number, which is due to increased device temperature, furthering temperature sensitive inefficiencies such as carrier leakage.

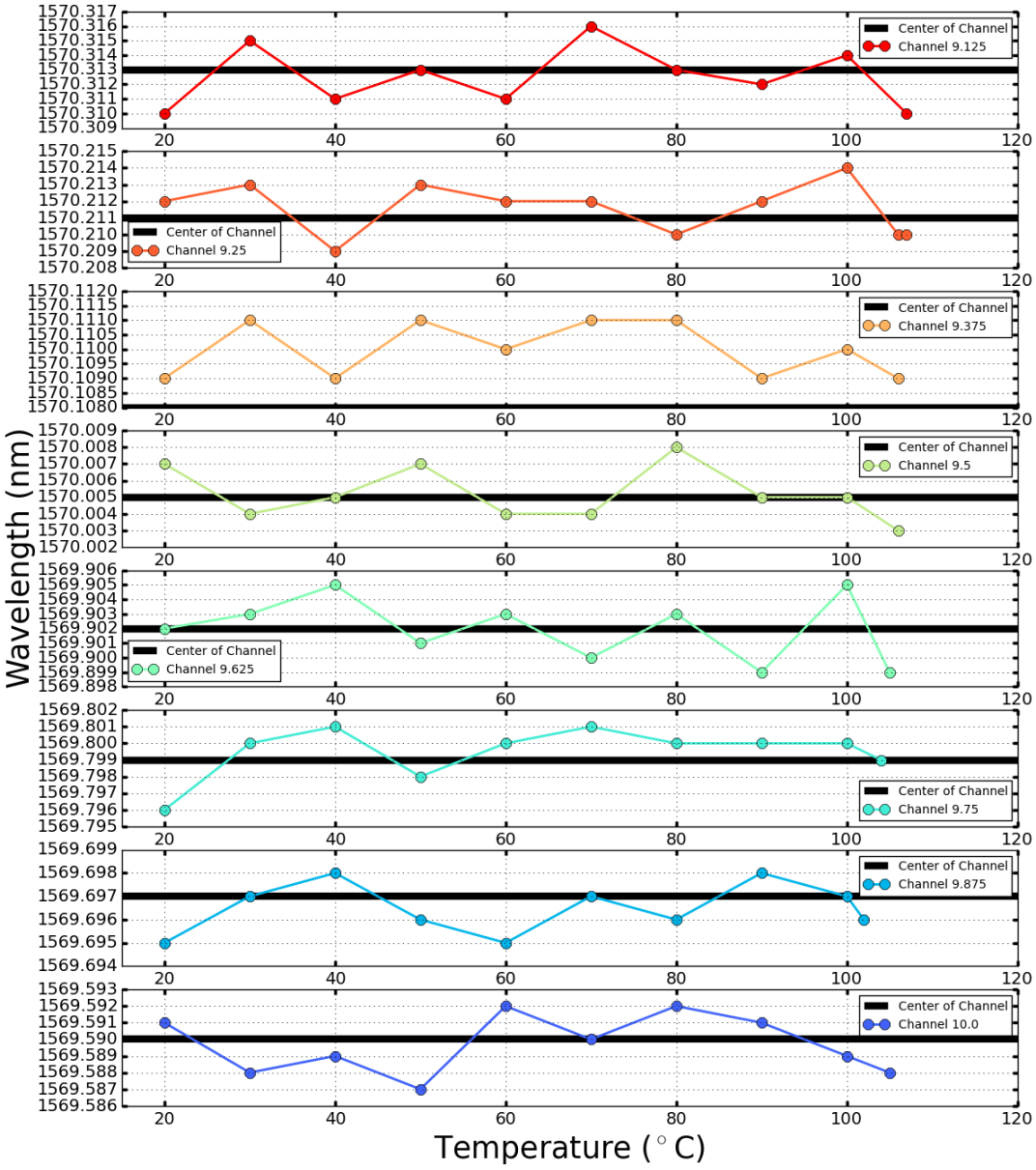

Figure 4.18: Wavelength stability of the 12.5 GHz spaced channels. Maximum drift of ±0.003 nm/±0.4 GHz from the channel centre is demonstrated.

The observed efficiency is seen to be relatively low, at around 1%, which is due to the devices operating at very high local temperatures. This is a trade off made to achieve a very high athermal range. If a smaller athermal range is required, then the amount of device self-heating could be reduced, and thus

a reduction in device temperature could be achieved, improving the wall-plug efficiency. Additionally, as the wavelength stability achieved was better than required, we chose to also investigate 12.5 GHz spaced channels on the DWDM grid, which allow a maximum spectral excursion of ±3.125 GHz. The chosen channels were between channels 9 and 10, with their specific wavelengths and stability illustrated in figure 4.18. As in the case of 100 GHz spaced channels, these more tightly spaced channels also exhibit a wavelength variation of ±0.003 nm/±0.4 GHz which is well within the ITU requirement. This level of stability could lead to further downscaling of channel bandwidth, below 12.5 GHz, however as the requirements in terms of wavelength stability are not yet defined, closer spacings were not studied. The athermal range is then illustrated in figure 4.19.

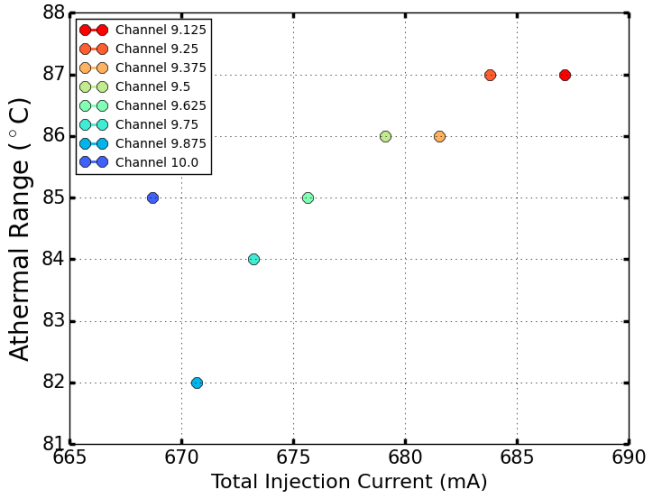

Figure 4.19: Athermal range of 12.5 GHz channels vs injection current.

It is observed to increase with decreasing channel number, however some of these channels seem to have a lower athermal range when compared to the 100 GHz channels they are surrounded by (channel 9 and 10). This is because channels 9.875 to 9 were operated within a different mode than channel 10, requiring lower total current for shorter wavelengths within the mode, and hence not allowing each channel to achieve the same amount of self-heating, leading to variations in athermal range.

The currents used for each channel are plotted in figure 4.20(a-c). It

is observed that while the grating current for channel 10 is the lowest, the gain current is not. As previously mentioned, for longer wavelengths, gain current becomes the dominant factor in deciding athermal range and thus, this results in channel 10 having longer athermal range than some of the other channels.

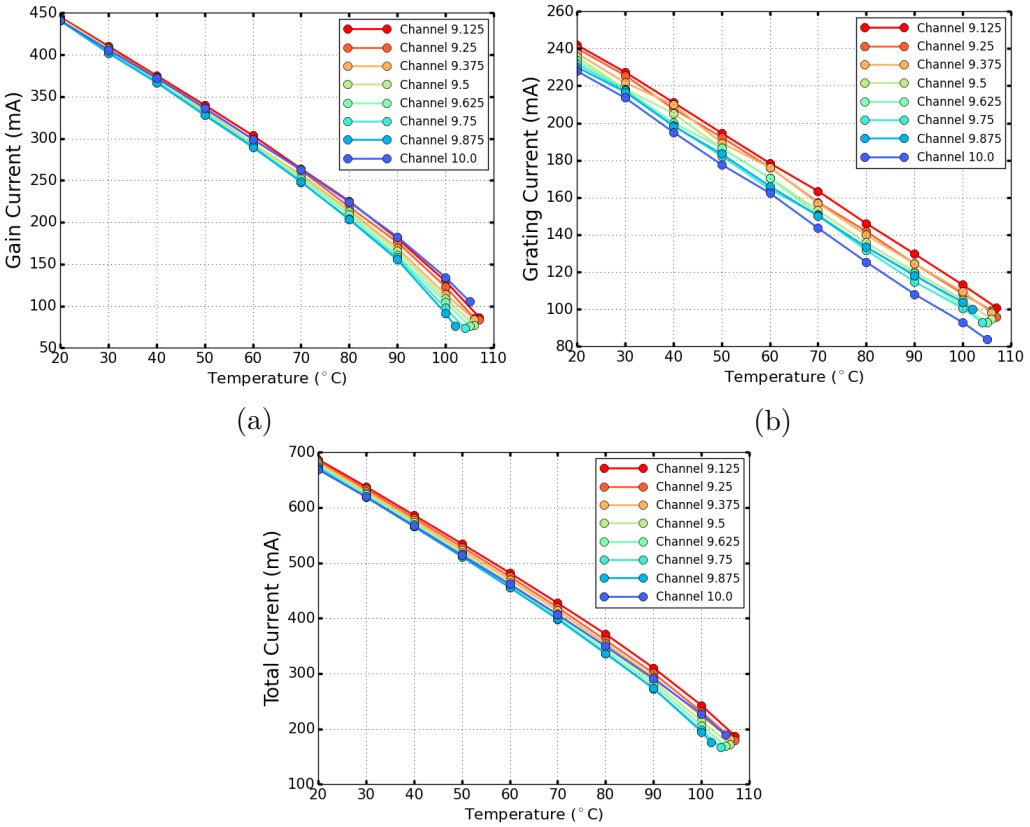

Figure 4.20: Variation of (a) gain, (b) grating and (c) total injection currents versus temperature over the athermal paths for 12.5 GHz spaced channels.

Output power and SMSR are also illustrated in figure 4.21 and are observed to be mostly consistent with trends demonstrated for 100 GHz spaced channels, which is expected.

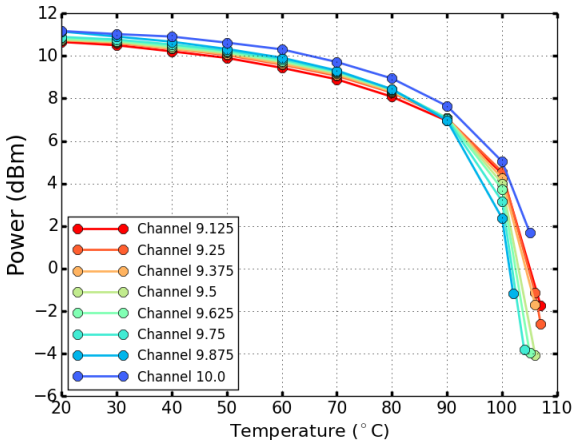

(a)

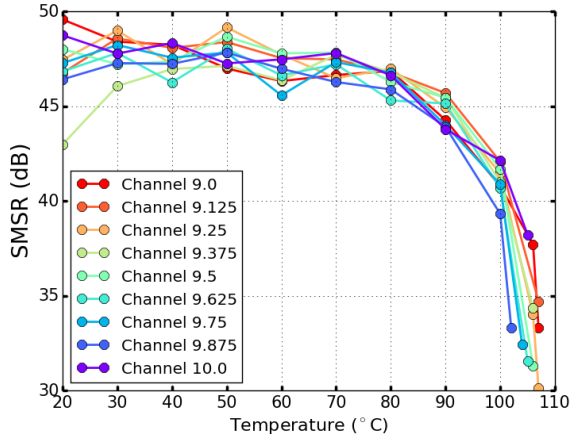

(b)

Figure 4.21: Variation of (a) output power and (b) SMSR and versus temperature over the athermal paths for 12.5 GHz spaced channels.

Wall plug efficiency similarly is observed to follow the same trend, with shorter wavelengths achieving improved efficiency. The athermalisation results shown here are the first to be performed on multiple channels, particularly of 12.5 GHz spacing on simple to fabricate devices, over such a wide temperature range. It is clearly observed that currents finely tuned over the two tuning sections of our device can achieve comparable, or even improved results over more complex, DS-DBR devices in terms of wavelength stability and athermal range. Thus, an array of ten of our devices could be a promising competitor to these more complex transmitters.

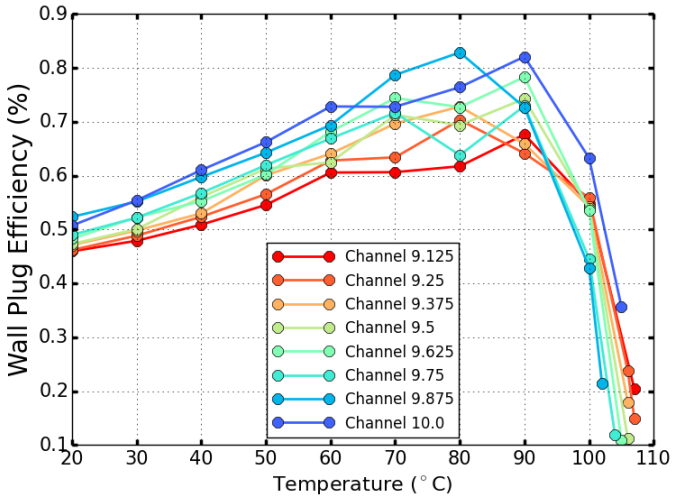

Figure 4.22: Wallplug efficiency versus temperature over the athermal paths for 12.5 GHz spaced channels.

4.4 Thermal Impedance Measurement

4.4.1 Introduction

In previous sections, we performed several athermalisations on our devices. In a previous chapter, we drew conclusions that our devices are dominated by thermal tuning. A useful parameter for thermal analysis is thermal impedance, which is defined as the temperature rise due to the applied electrical power into a particular component, which can be given by,

$$Z_{th} = \frac{\Delta T}{P_{dis}} \tag{4.1}$$

where ΔT is the temperature rise of the component in question, and P_{dis} is the power dissipated as heat. Laser diodes above threshold emit light, therefore this can be taken into account when calculated dissipated power, which is then given by

$$P_{dis} = P - P_0 \tag{4.2}$$

where P is the total power input into the laser diode and P_0 is the optical output power. However, for typical semiconductor laser diodes, the opti-

cal output power is much lower than the dissipated power. In this work, the wall plug efficiency is somewhere on the order of 1 to 5 % [35, 60] and therefore, P_0 has been omitted from our analysis. Due to this, P_{dis} only requires the measure of input current and voltage across the junction which are both trivial to measure, therefore we are only required to measure ΔT. Several methods to measure device temperature have been developed, such as one method by Paoli which exploits the temperature dependence of refractive index [61], making use of the lasing wavelength as a temperature probe. However, this technique is only capable of measuring thermal impedance for single section devices and is thereby unsuitable for any distributed Bragg reflector or more complex lasers. Thermal imaging provides another approach, with infrared (IR) [62,63] and more recently CCD-Thermoreflectance (CCD-TR) [59, 64–66] imaging yielding accurate, spatially distributed temperature profiles which could then be used to calculate thermal impedance. However, both these methods provide temperature profiles for the surface of the laser which may not lead to an accurate value of thermal impedance and in particular for CCD-TR, it requires a layer of material with high thermoreflectance coefficient on top of the surface of the laser to acquire an image, which may not be possible for some device structures.

Earlier in this chapter we have shown that input power with temperature over an athermal range has a linear relationship. Thus, we can get the change required in output power to offset a change in temperature relatively easily from the slope of that graph, or in equation form

$$Z_{th} = \frac{\Delta T}{\Delta P} \tag{4.3}$$

where ΔT is the temperature ambient change and ΔP is the change in power required to overcome the temperature change and maintain the athermalisation condition. Then, using this simple relationship, we can extract the thermal impedance of individual laser sections. This method is possible for all-active laser lasers.

4.4.2 Measurement and Results

For these measurements we used three device lengths of the same grating design, as given in table 3.1. The difference between devices then arises via differences in gain section length (170,470 and 770 μm for 400, 700 and 1000 μm devices respectively). Then, to measure thermal impedance, the setup in figure 3.2 has been used.

4.4.2.1 Distributed Bragg Reflector Lasers

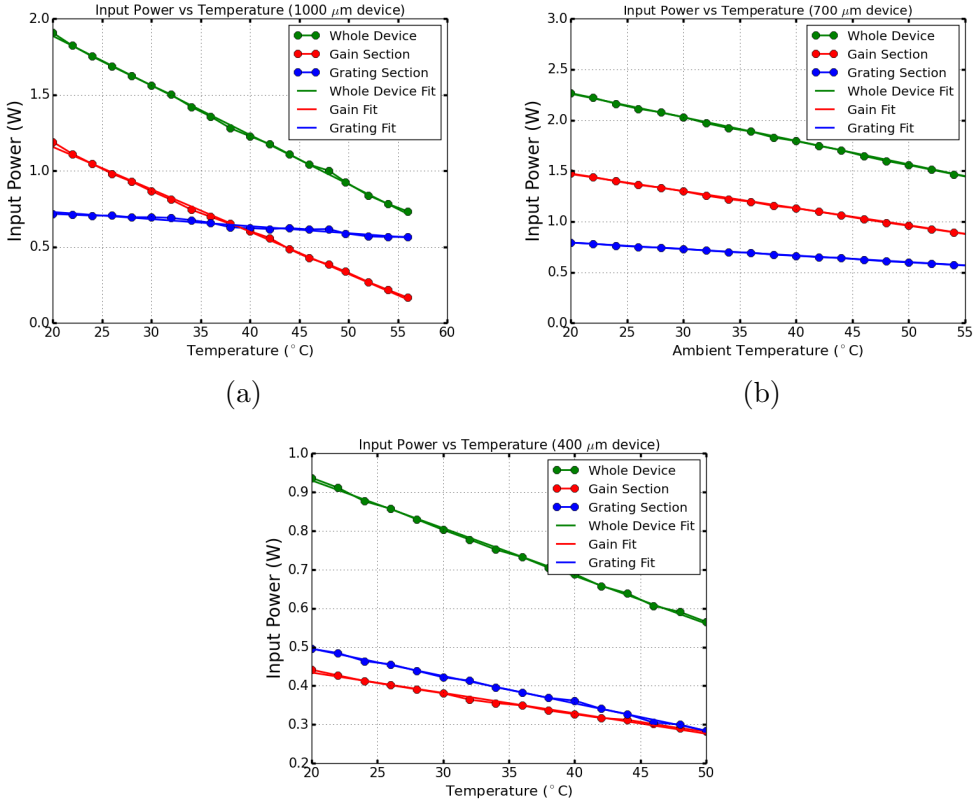

Figure 4.23: Change of input power versus temperature while maintaining the athermalisation condition. A linear regression is used to fit the relationships for each section. (a) 1000 μm (b) 700 μm and (c) 400 μm devices respectively.

To measure the thermal impedance of the DBR lasers, three laser diodes with the same material properties, of differing cavity lengths 400, 700 and 1000 μm were continuously athermalised over various temperature ranges. This was done to demonstrate a consistency in the measurement between differing devices and to obtain an average for the wafer material. The athermalisation was achieved by reducing the gain and grating currents with increasing temperature and vice versa) to ensure that the Bragg peak and the cavity modes stay aligned at the right wavelength when temperature is varied. The achieved wavelength stability in each athermalisation was $\pm$0.003 nm / $\pm$0.4 GHz, which is likely much higher precision than required for this measurement. The electrical input power versus ambient temperature for these athermalisations is given in figure 4.23. As expected, a linear relationship for each section (and hence, the whole device) is observed which has been fitted. The thermal impedance can then be calculated from the following relation,

$$Z_{th} = -\frac{1}{m} \tag{4.4}$$

where m is the slope for each respective section. For this case, the thermal impedance for each respective device is listed in table 4.1.

Table 4.1: Thermal Impedance (Z_{th}) of the respective lasers and their sections.

Device length (μm)	Z_{th} (Gain Section) (^{o}C/W)	Z_{th} (Grating Section) (^{o}C/W)	Z_{th} (Whole Device) (^{o}C/W)
1000	35.89$\pm$3.9	215.19$\pm$25.6	30.87$\pm$2.5
700	59.45$\pm$5.4	156.28$\pm$17.0	43.07$\pm$3.1
400	190.17$\pm$27.9	141.6$\pm$19.7	81.16$\pm$8.2

Multiplying by the length of each section and converting to milliwatts gives us the impedance length product ($Z_{th}L$), which is useful for comparing thermal impedances for sections of different lengths. This impedance length product in each respective device is given in table 4.2.

Note, all of the errors in this work have been calculated using standard Gaussian error propagation. It is interesting to note that this product is

Table 4.2: Thermal Impedance (Z_{th}) times length (L) of the respective lasers and their sections.

Device length (μm)	$Z_{th} * L$ (Gain Section) (^{o}C μm/mW)	$Z_{th} * L$ (Grating Section) (^{o}C μm/mW)	$Z_{th} * L$ (Whole Device) (^{o}C μm/mW)
1000	27.63±3.0	49.5±5.9	30.76±2.5
700	27.94±2.5	35.94±3.9	30.15±2.1
400	32.33±4.8	32.57±4.5	32.47±3.3

larger for the grating section in all devices. This is possibly due to the fact that there are slots in the waveguide, resulting in larger current density passing into the grating per milliamp of current.

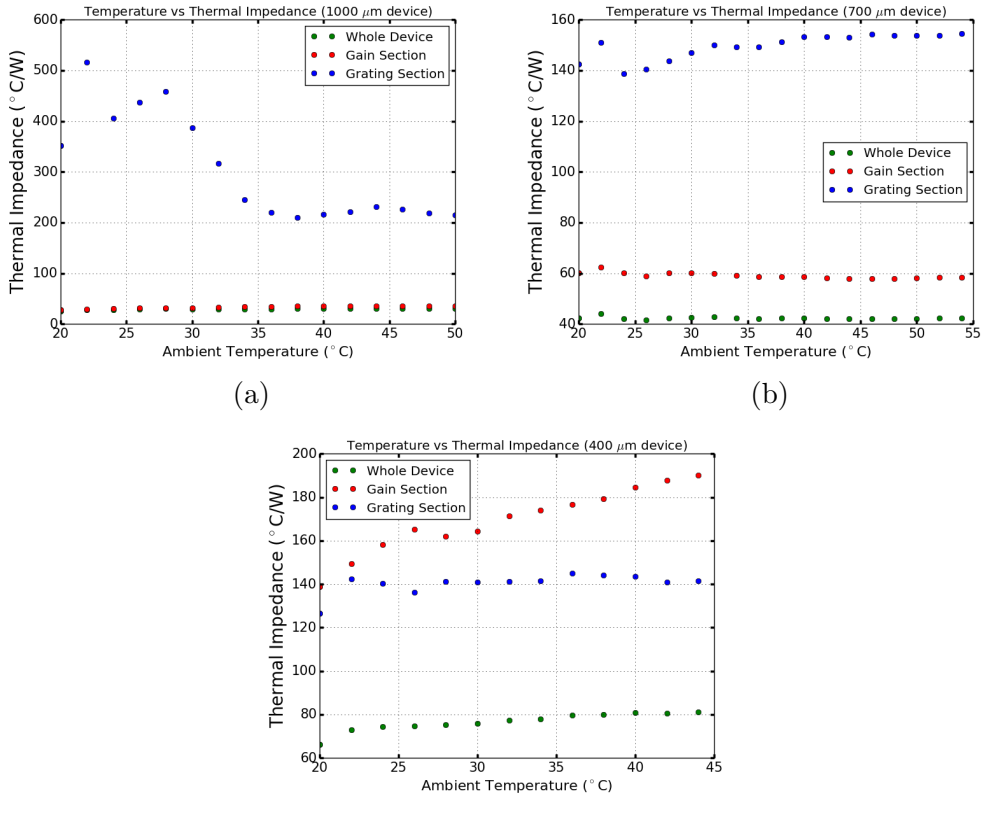

Figure 4.24: Ambient Temperature versus thermal impedance, measured from the starting temperature of 20 ^{o}C. (a) 1000 μm (b) 700 μm and (c) 400 μm devices respectively.

In particular, the value for the 1000 μm long laser seems to be significantly higher. This is likely due to the longer gain sections output power varying more significantly with changing current, for example, when the current is reduced to compensate for increasing ambient temperature, the output power is reduced, resulting in a lower photon density entering the grating section which will keep the carrier density higher in the respective section, altering the gratings refractive index and thus increasing the apparent value of the thermal impedance.

Thus, there is a limitation if output power varies significantly (assuming any amplification remains constant) over the measurement range. This was not the case for the 400 and 700 μm devices (where the power remained relatively constant over the measurement range), however it was the case for the 1000 μm laser (where the power dropped by 3 dB over the measurement range). This results in the measurement only being valid for the whole device and not the individual sections for the 1000 μm device. Additionally, as one of the fundamental assumptions of the method is that the wavelength change is only a result of temperature change, we expect there to be a low current limitation, as wavelength change in the low current regime is more significantly impacted by carrier effects.

Previously, our group conducted thermal impedance measurements using CCD-TR imaging [59] and the average values obtained in this work (29.3±2.1 ^{o}C μm/mW for the gain section and 39.33±2.8 ^{o}C μm/mW for the grating section) seem to be lower than the ones acquired previously using CCD-TR (40±6 ^{o}C μm/mW). This could be due to heating at the gold to semiconductor junction, which would have a higher effect on the surface temperature than the waveguide temperature. As CCD-TR is a surface imaging technique, this would explain the higher thermal impedance values shown there. The values acquired here however are in line with other group research outlined in reference [67].

Finally, a necessary thing to investigate is how many temperature steps (in this case the steps are 2 ^{o}C) it takes to achieve convergence towards these values. One reason is that a single step might not produce an accurate value, because it is not necessary to align the cavity modes and the reflective peak

at the same positions every time to produce the same wavelength, hence this might introduce significant error, however over many steps, this error will average out. Additionally, if too few steps are taken, then it may be plausible to just use the gain section to athermalise or just the grating section, however this single section tuning is not possible without mode hops for more than a few temperature steps. The ambient temperature versus thermal impedance is plotted in figure 4.24. It can be seen that after approximately 10 steps (20 ^{o}C), thermal impedance converges to its steady state value for all sections. This suggests that for this method to be of significant accuracy, an athermalisation range of approximately 20 ^{o}C is required. This level of athermalisation has been achieved by many devices in the literature and hence is not a significant limitation to the technique.

4.5 Conclusion

In conclusion, first we have used the results derived from the previous chapter to extend the athermalisation range of our lasers. Significant improvement was observed, with a device being continuously operated from 5 to 106 ^{o}C, and discontinuously to 115 ^{o}C with a wavelength variation of $\pm$0.4 GHz/0.003 nm which is well within the TWDM specifications. This performance is the best achieved to date in terms of continuous and discontinuous athermalisation range. When a smaller athermal range is required, it was shown that wall plug efficiency can be significantly improved by optimisation of starting currents for athermalisation.

Secondly, we have used the same approach to operate the same device athermally, achieving mode-hop free performance over eight, 100 GHz spaced channels with a wavelength variation of $\pm$0.003 nm/$\pm$0.4 GHz, with an athermal range of 72-108 ^{o}C depending on the channel. This performance has also been shown on a more tightly spaced, 12.5 GHz grid.

Finally, a new method to measure thermal impedance using the athermalisation condition was presented. This method allows measurement of thermal impedance for several types of laser devices, with single grating DBRs having the capability of measuring thermal impedance of several laser

sections, here being measured as 29.3±2.1 ^{o}C μm/mW for the gain section and 39.33±2.8 ^{o}C μm/mW for the grating section. By extrapolating, this technique allows measurement of device/section average temperature. The results from this technique can be used for design and optimisation of laser diodes. Furthermore, it can be used to monitor device burn in, where thermal impedance is expected to vary significantly, particularly for high-power usage cases. Finally, usage of the technique is non-invasive and does not require special equipment, which is desirable.

Chapter 5

Pulsed Mode Characterisation and Optimisation

5.1 Introduction

In the previous chapter our 700 μm devices were athermalised over a wide range of ambient temperatures, with changes in various device parameters documented. It was shown that very wide range wavelength stable operation was possible on simple, all-active ridge waveguide devices. In this chapter, we examine the transient behaviour of such devices. In particular, one of the focuses of this chapter is the change in wavelength over time as a laser is operated in pulsed mode.

Previous chapters drew the conclusion that 700 μm devices were the most suitable for athermalisation, however this was only the case for steady state operation. Pulsed operation has several other factors to consider, with rise time [57] and wavelength settling time being among them, which would be affected by laser size. Hence, we will revisit devices of differing lengths to choose an optimal device for our pulsed mode study. A characteristic study of their performance while under pulsed operation is performed. In particular, we look into both the short term and long term effects of laser excitation. In literature, transient thermal evolution for all-active laser devices under current injection has been experimentally demonstrated to be explained with

several time-constants [68]. Some of the short time constants can be as low as 11 ns, with the longer ones being on the order of milliseconds. The longer time constant portion is of particular interest for athermalisation as this is how long it will take for a device to stabilise after being retuned given a change in ambient temperature. Similarly, retuning of the laser is also relevant for wavelength switching/optical switch systems, and is thus investigated.

Shorter time constants, on the other hand, are relevant for the newly emerging telecommunications standard known as TWDM. This relevancy is due to the standard having a repetition rate of 8 kHz and thus thermal effects with the slower time constants are deemed irrelevant, due to the fact that the current is turned off before they can take effect, and the laser beginning to cool down. Another one of the key specifications that has to be met is the maximum spectral excursion. For the tightest channel spacings the wavelength needs to be maintained to within $\pm$12.5 GHz/0.1 nm of the channel centre. This is particularly challenging to achieve due to the aforementioned thermal deviation under pulsed current injection. Frequency shifts of over 100 GHz have been shown in literature [69], overshooting the telecom standard requirements by several times. Clearly compensation methods are required, as typical tools such as TECs are far too slow to compensate for these rapid thermal transients. Several methods have been proposed in literature [38,69–74] and some of their performance is investigated on our devices. From the results of these tests we derive our own method for reducing the wavelength drift and experimentally demonstrate its performance.

Finally, we examine the transient thermal behaviour of our devices in a more direct fashion via thermal imaging of the device surface. Charged Coupled Device Thermoreflectance (CCD-TR) has been chosen as our method of choice given our device feature size and the non-invasiveness of the technique. As transient CCD-TR is a relatively new technique, a detailed method of operation is presented alongside pulsed mode heating results of the laser in question.

Then, an extensive pulsed mode study of our lasers is presented. In section 5.2.2, we investigate the performance of three laser lengths under pulsed mode operation in terms of wavelength deviation and rise time. From these

results a single device is chosen. Then, in section 5.2.3, the results of wavelength deviation while the device is subjected to compensation techniques are presented. Finally, in section 5.3, we introduce the transient CCD-TR method and use it to thermally map our device while under pulsed mode operation.

5.2 Wavelength Discrimination Measurements

Wavelength discrimination is a technique to extract wavelength deviations that occur while a laser diode is operating. Previously, the go-to technique used to be heterodyne beating, however, due to requirement of expensive equipment and complex analysis, a technique based on wavelength discrimination was chosen for our measurements. In an introductory paper it was shown that wavelength discrimination can meet the same level of accuracy with reduced complexity and simple analysis [75]. The setup and analysis method is presented in the following section.

5.2.1 Experimental Setup and Analysis Theory

The setup for the wavelength discrimination measurement is shown figure 5.1.

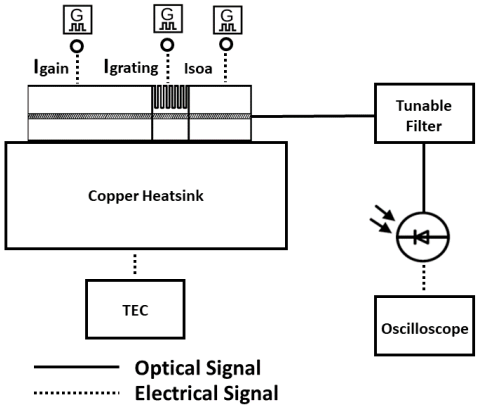

Figure 5.1: Setup to measure wavelength deviation over time.

A laser is placed on a copper heatsink which is integrated with a TEC and

a thermistor. This TEC is used to simulate a constant ambient temperature. Pulses of current/voltage can then be introduced to laser sections by either directly connecting a function generator (Gwinstek AFG-2225) to a relevant section or by modulating a current source with a function generator. We explore both methods. Light from the laser is then collected using a lensed fibre, which is then passed through a tunable filter (Finisar WaveShaper 1000S) which attenuates light of differing wavelengths at differing rates, effectively turning power variations into wavelength variations. The remaining light is then passed to a photodiode (Newport Model 1817 balanced photoreceiver) with the resulting electrical signal from the photodiode is then displayed by an oscilloscope. Analysis of this signal is then performed on a computer offline. This measurement has to be run twice, once for when the filter is set to transmit all light without attenuation ($P_0(t)$) and second for when the filter is set to attenuate differently at different wavelengths ($P_f(t)$). An example profile for when the attenuation of the filter is set to be wavelength dependant is shown in figure 5.2.

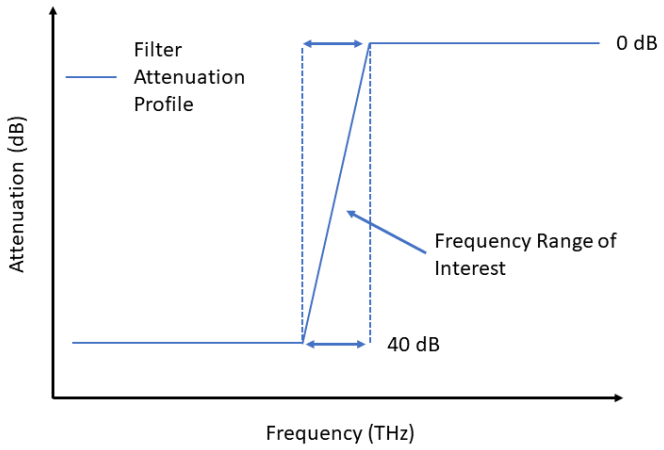

Figure 5.2: Example filter profile for collecting $P_f(t)$.

Both of these quantities collect the power over time. Then, we acquire the ratio of the powers as,

$$R_p(t) = -10 \times \log_{10}(\frac{P_0(t)}{P_f(t)}) \tag{5.1}$$

where the conversion to the decibel scale is performed due to the filter attenuation being given in dB. We then iterate over the ratios for each time and compare to the filter attenuation. If the ratio is within less than 1% of the given attenuation, then we say that this is our wavelength value. This is done as the filter attenuation is not perfectly continuous. One important thing to make sure of is that $P_0(t) > P_f(t)$ for all values of t during the active part of the pulse, or rather any part that is not inclusive of the rising portion of the pulse. This is because we generate a slope of attenuation over a small range of wavelengths and then the attenuation is set to 0 dB for the rest of the wavelength range, hence if $P_0(t) = P_f(t)$ at any point, we cannot discern what wavelength this corresponds to, effectively nullifying the measurement. This is done because the filter is capable of covering the entire C-band, and we are dealing with relatively small wavelength variations, thus we require a steep attenuation slope over a small range of wavelengths to get an accurate reading. An example set of raw data is shown in figure 5.3 for a 700 μm device undergoing a 5 V_{pp} voltage pulse.

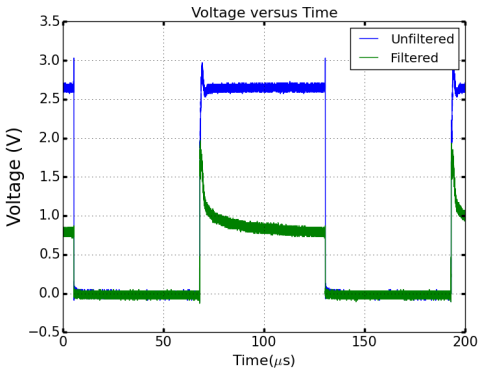

Figure 5.3: Example of raw data from the wavelength discrimination measurement.

As can be seen, the unfiltered pulse has an amplitude which is higher for all values during the pulse payload. The data during the pulse payload is then run through the calculation while being compared to the filter, yielding wavelength change over time which is present in the measurements in the next few sections.

5.2.2 Pulsed Mode Characterisation and Device Selection using square waves

5.2.2.1 Entire Device Pulsing using the current source

To identify which of our lasers is most suited for pulsed mode operation we first examined all of the lasers without any compensation methods. Initial characterisation consisted of square wave pulses to all of the lasing (gain and grating) sections. This is the ideal scenario for energy saving purposes as the laser is only on when it needs to be.

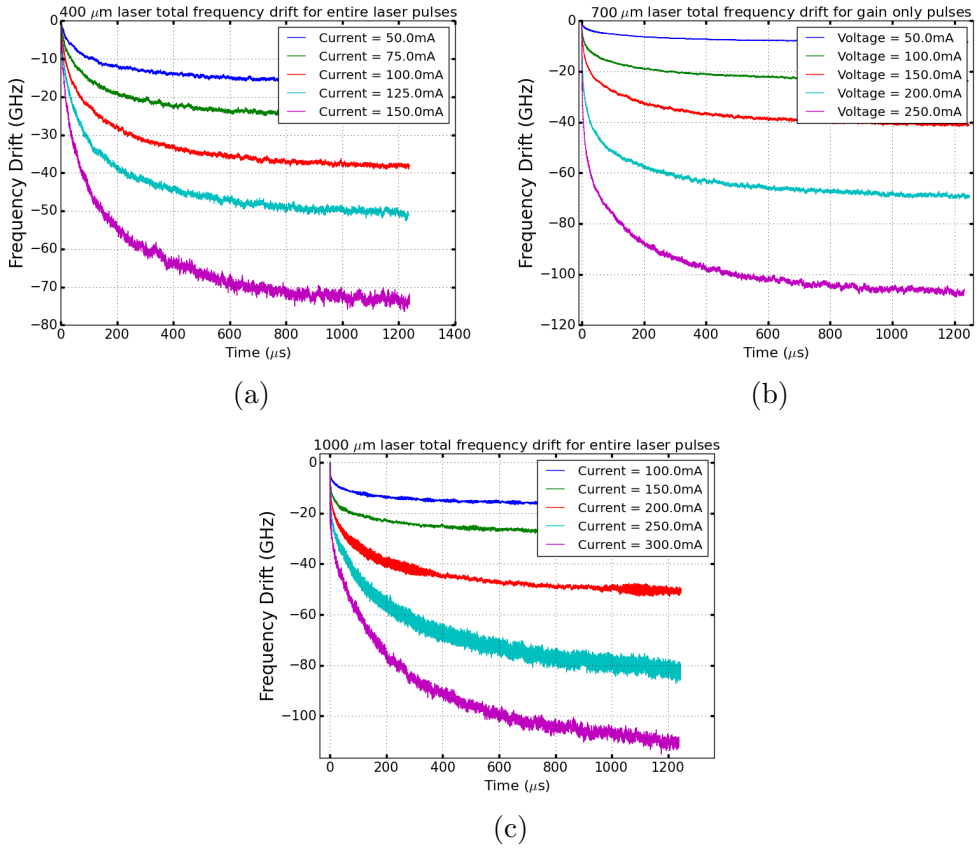

Figure 5.4: Frequency variation when the entire laser is pulsed via the current source for device lengths (a) 400 and (b) 700 and (c) 1000 μm.

In this case we modulated a current source using a function generator. One drawback from modulating our current source is that it is relatively slow,

with the resulting rise time and electrical ringing adding up to $> 5\mu$s which would make this sort of pulsed signal unsuitable for TWDM systems. This is a limitation of the current sources which we are using for this experiment. However, this sort of pulsed operation is useful for direct comparison between laser devices as we can get precise current/voltage readings and also, for some purposes, such as laser retuning, it is not necessary to have sub-μs switching/turn-on times, with current precision being more important. The results are displayed in figure 5.4.

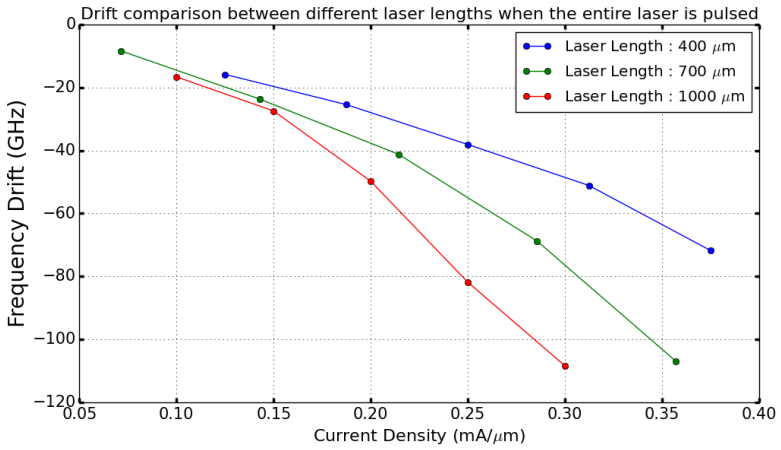

(a)

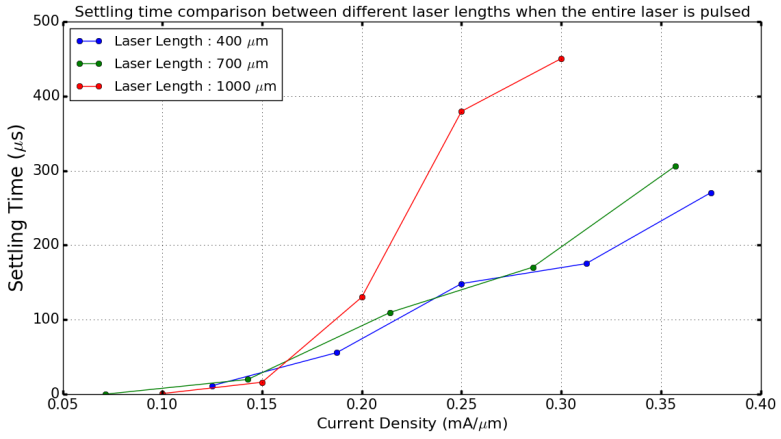

(b)

Figure 5.5: (a) Total frequency change and (b) Settling time per unit current density for different device lengths when the entire laser is pulsed.

As can be seen, the total drift increases with increasing current, as would

be expected due to a larger amount of self-heating. Longer devices seem to experience less overall drift per milliampere of current, however this is simply a thermal impedance issue. As shown in chapter 3, equation 3.6, thermal impedance scales inversely with length, and thus reducing the length of the laser will yield a larger amount of heating per unit current. It is then useful to compare the wavelength drift per unit current per unit length of each laser device. This is shown in figure 5.5. It can be clearly seen that shorter devices experience less drift per unit current per unit length. This is due to the heating that occurs in the first five microseconds which we cannot see in this measurement. Longer devices have much more surrounding material resulting in a longer/more spaced out heating duration. This then results in more of the heating occurring after the rising portion of the pulse, which we can observe. An indication towards this answer is given in figure 5.5(b), where the settling time is observed to rise with increasing device length. In this case, we define the settling time as the time taken for the device to reach its target (final) wavelength to within ± 0.1 nm/12.5 GHz. Another contribution for this result could be due to differences in capacitance and/or resistance between differing laser lengths causing variations in rise time and ringing amplitudes, however this aspect was not investigated.

5.2.2.2 Entire Device Pulsing using the function generator

Drawing our conclusion above, it is then naturally of interest to explore what occurs during the initial portions of the pulse (under 5 μs). While this is not possible using the current source due to its limitations, it is possible by directly connecting a pulse generator to our device. Additionally, shorter risetimes are also required to meet the TWDM telecom standard. Thus, to try to meet the TWDM standard, for which the maximum allowed rise time is 128.6 ns, we then switched to using a function generator which has an electrical rise time of $\approx$ 20 ns to modulate our device.

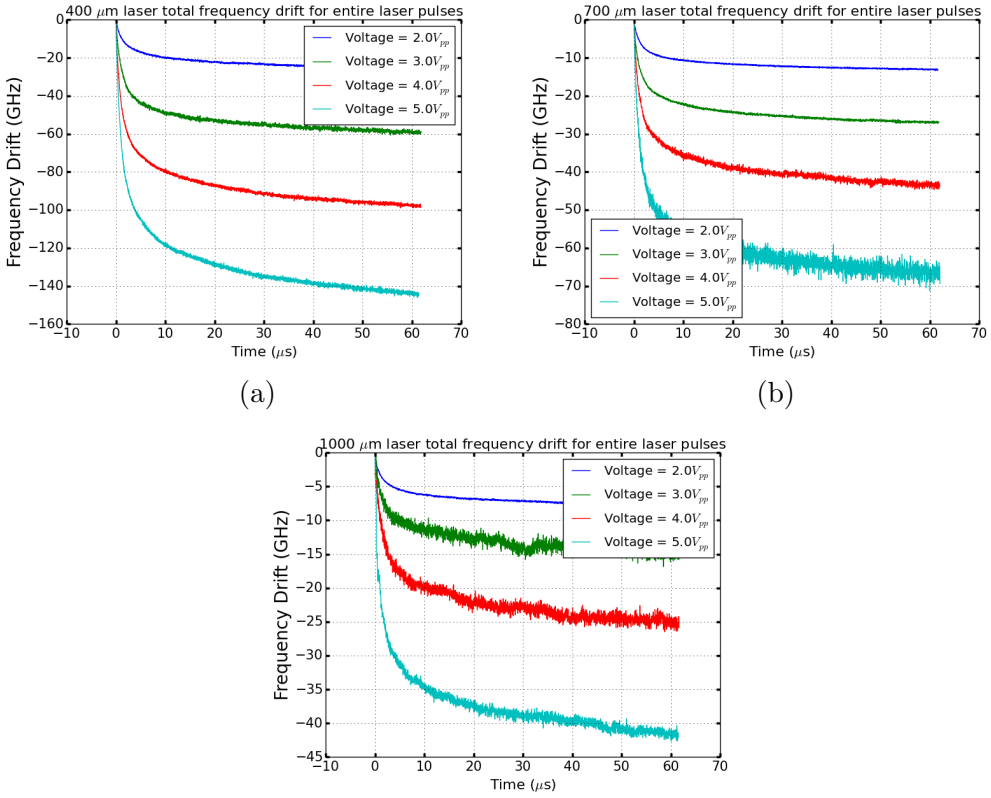

Figure 5.6: Frequency variation when the entire laser is operated via the pulse generator for device lengths (a) 400 and (b) 700 and (c) 1000 μm.

In this case, we focused on a shorter time frame as well, meeting the 8kHz repetition rate of the TWDM standard and using a 50% duty cycle which

should be the worst case scenario for a TWDM transmission system. One thing to note is that our function generator expects to transmit voltage into a 50 Ω load, and so at maximum output should be capable of outputting around 100 mA of current.

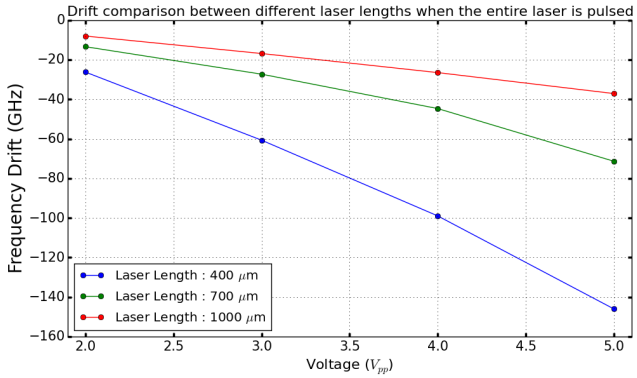

(a)

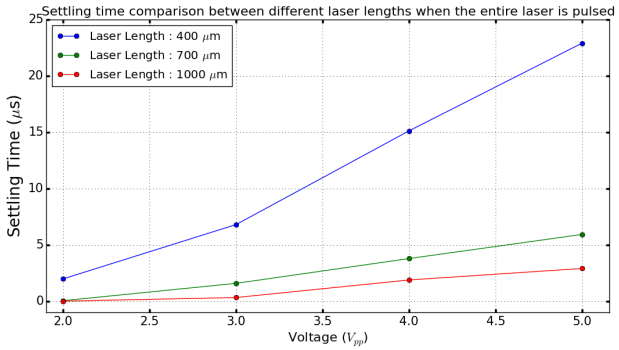

(b)

Figure 5.7: (a) Total frequency change and (b) Settling time per volt for different device lengths when the entire laser is pulsed.

However, as our lasers have lower resistance, the voltage the function generator will apply across them will be lower than stated, and due to the impedance mismatch may result in larger rise times. A solution for this would be to get the devices packaged or wirebonded with an inline resistor, however this was not possible for this study. The results of the entire laser being pulsed for each respective length is shown in figure 5.6 for different voltages. The rise-time observed is ≈ 300 ns across all devices, which is

above the allowed limit of 128.6 ns for TWDM. Nonetheless, it is interesting to have a look at the 4.7 μs of extra information we have available of our laser under pulsed mode operation. As expected, we observe the same trend of increased wavelength drift per increase in voltage for each device length. Figure 5.7(a) shows the total drift experienced by the device per unit applied voltage. This now shows that when you include the shorter timescale, the shorter device experiences more drift. This is due to the faster heating of the shorter devices, and agrees with the result shown earlier. The settling time is shown in figure 5.7(b) and is much shorter than we found in figure 5.5 (b), with the shorter device observed to have longer settling time, however this is mostly due to the significantly larger amount of the drift it undergoes. The longer devices do not drift as much, and thus can reach within the target wavelength within $\pm$0.1nm/12.5 GHz faster.

5.2.2.3 Gain section only pulsing using the function generator

As we've seen in figures 5.4 and 5.6, the wavelength drift is typically very large, on average several times the allowed drift for TWDM, unless we use very low currents/voltages. Even for the lowest voltage shown, only the 700 and 1000 μm long devices can meet the TWDM standard, and then it's only if we consider 100 GHz spaced grids which allow wavelength drifts up to $\pm$ 20 GHz/0.2nm. The current industry push is for 50 GHz spacing and below, thus we need to come up with a solution to achieve lower drift. As mentioned, lower pulse amplitude leads to lower drift across all devices, so one solution would be to lower the pulse amplitude even lower. This is not really feasible as the devices cannot achieve threshold at lower voltages. However, one advantage of multi-section devices, such as ours, is that we can pulse one section at a time, with the other sections remaining at steady state operation. This allows us to use a lower pulse voltage to the device section that's operating in pulsed mode, allowing the entire device to go above threshold at lower pulse amplitudes. One great example of this kind of operation is a laser in a master-slave configuration, for which only the gain section of the slave laser is typically modulated [76].

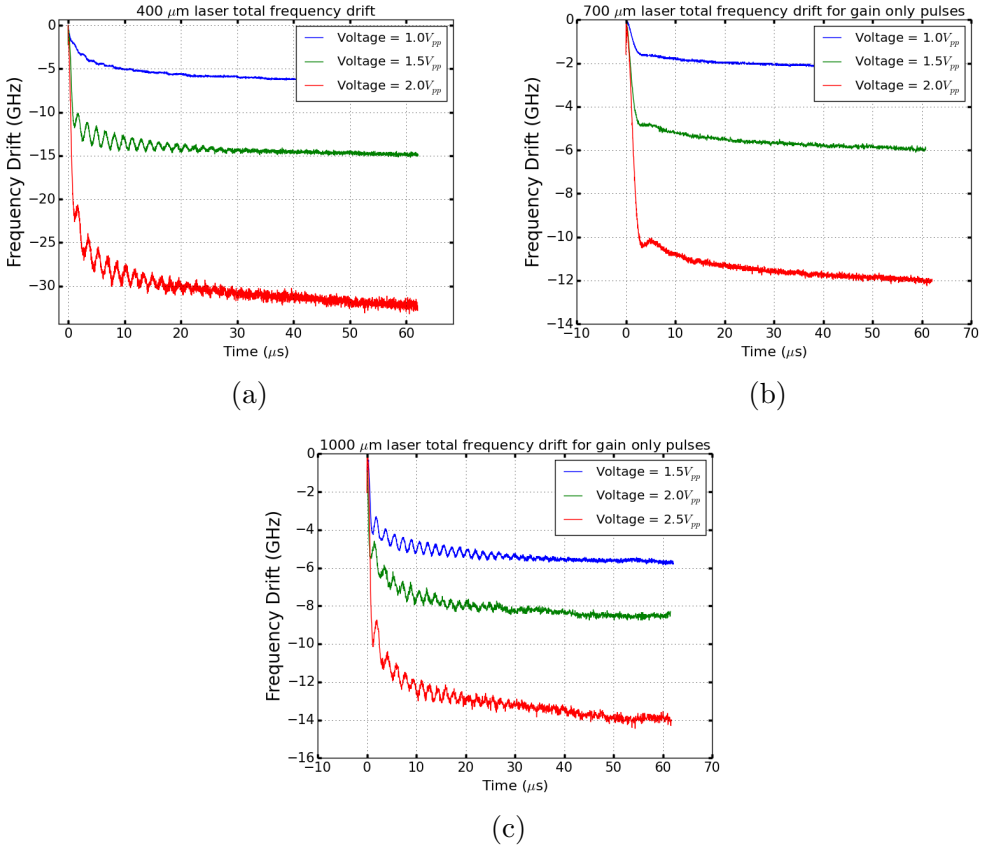

Figure 5.8: Frequency variation when only the gain section is pulsed via the pulse generator for device lengths (a) 400 and (b) 700 and (c) 1000 μm.

Then, it also makes sense to operate our lasers in a similar fashion. Another benefit of operating in this way is the reduction in rise time due to pulsing a smaller volume, which would in turn result in lower capacitance, which is directly related to rise time, resulting in our rise-time dropping to 50-100 ns depending on pulse voltage. For our lasers, the grating section remains a constant size, and thus, we tested pulsing the gain section while the grating and SOA sections remained in steady state operation, with the frequency change data shown in figure 5.8. Once again, we can see the expected result of increased drift with increasing pulse amplitude, however, as mentioned earlier, due to using smaller pulse amplitudes we observe significantly reduced wavelength drift. It is seen that across all three device sizes that there is at least one voltage configuration where we can comfortably meet

the ± 12.5 GHz/0.1 nm TWDM maximum spectral excursion requirement.

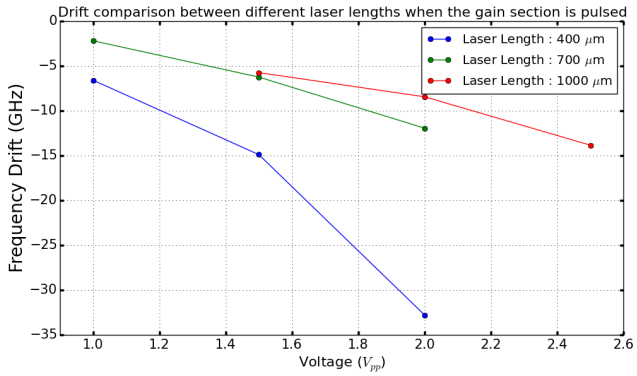

(a)

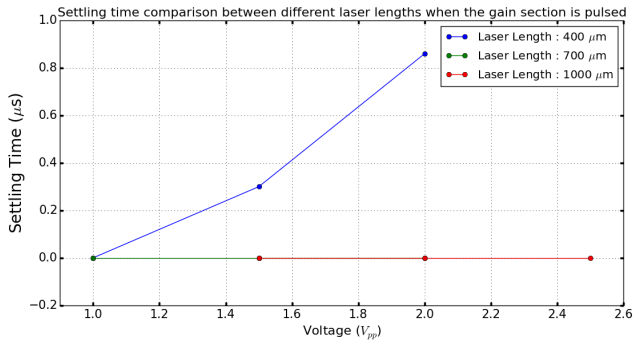

(b)

Figure 5.9: (a) Total frequency change as a function of voltage and (b) Settling time per volt for different device lengths when the gain section is pulsed.

Similar behaviour as seen previously is observed with the drift per unit voltage across device lengths in figure 5.9 (a). The settling time is shown in in figure 5.9 (b) and for the 700 and 1000 μm devices is seen as or near 0 μs, but that is because the observed drift is seen as less than ± 12.5 GHz for the entire duration. One drawback of this approach is that is it necessary to stick to low pulse amplitudes, even if further tunability is desired. This is because the reflective peak remains at a relatively constant position, while the cavity modes are shifting position over time as the gain section is heating up. Thus, for larger pulse amplitudes, this results in mode hops, which are catastrophic for burst mode transmission systems. This effect gets worse for

longer lasers due to smaller cavity mode spacing, however as using smaller pulse amplitudes is desired for decreased wavelength drift, this is not a large issue. Then, as the lowest drift (≈2.5 GHz) was observed for a 700 μm device (while the gain section was under burst mode), and due to much of our athermalisation work occurring on this device, it seems like a natural choice for TWDM networks and for further study on compensations techniques and thermal measurements, which are to occur in the following sections.

5.2.3 Further analysis and compensation techniques

As we have seen in the previous section, is it possible to achieve a frequency drift of ≋ 2.5 GHz. This is well below what is required for upcoming TWDM networks. However, for purposes of energy efficiency, it would be desirable to have the entirety of the laser unbiased when it is not transmitting data. In the previous section it was shown that for most currents/voltages it is not feasible to meet the TWDM requirements using standard methods, and thus we look into others from the literature.

5.2.3.1 Sub-Threshold Heating

One method in particular is known as sub-threshold heating [72], which involves passing a small amount of current into the laser, where it is still well below threshold and then when data is to be transmitted, the laser is turned on to its normal level. This can significantly reduce energy usage as the typical current used would be far below the pulsing current. We performed this on our 700 μm device, and the result can be seen in figure 5.10. The blue curves denote the compensated state, of the voltage pulse just below it. Using an off-state voltage of 1V, we can see there is an approximately 6 GHz of reduction in overall drift across all voltage pulse amplitudes. This is due to the fact that the overall change in voltage is less, or to think of it in another way, that 1V worth of heating has already occurred, and does not need to occur again. This is a significant result as the 2V pulse is now well within the tightest TWDM spacing requirements, with the other pulses falling outside these, however, Simon et al [73] suggested that knowing the precise starting

wavelength of the laser (beginning of the pulse), and assuming the wavelength changes in one direction only, the ±12.5/20 GHz maximum spectral excursion limit can be doubled.

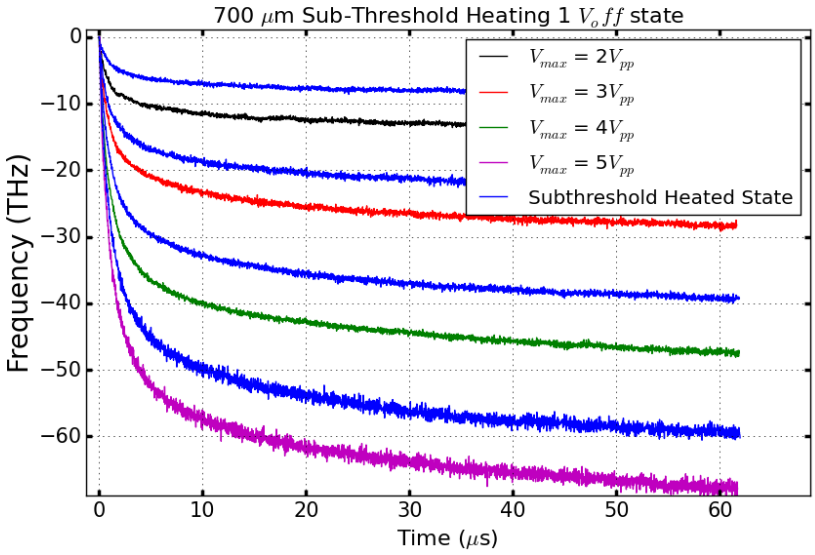

Figure 5.10: Frequency change in the sub-threshold heating scheme, with the blue curves denoting when sub-threshold heating is employed, and the coloured curves denoting regular pulsed operation.

In this case, the compensated approach would fall within limit up to 4 V_{pp}. One concern for this type of scheme that arises is the device is emitting some amplified spontaneous emission (ASE) noise while in the non-transmitting state. If the sub-threshold voltage is too high, then the emitted ASE will be too high and won't meet the TWDM requirement. In our case, the non-transmitting states emission is shown in figure 5.11. The difference between the two peaks is 51.97 dB which is enough for TWDM transmission [77]. It should be noted that this result is achieved having the SOA be on at steady state conditions. If the SOA was modulated as well, for example if it was turned off or even reverse biased in the off state, the emission from the laser would not be amplified and thus we would expect a much better result in terms of extinction ratio.

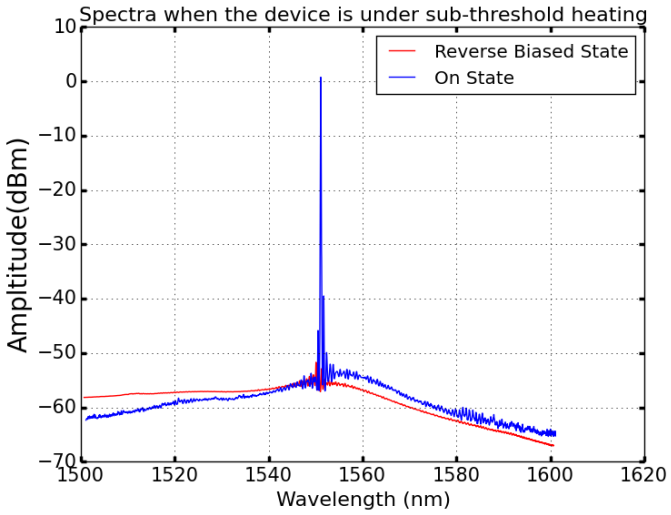

Figure 5.11: Example spectra of the laser when in the off-state for sub-threshold heating (+1V) and in the on (+5V) state.

5.2.3.2 Accelerated Self-Heating

Another method that has been proposed in literature is called Accelerated Self-Heating [70]. The idea behind this method is to overshoot by a significant amount at the beginning of the pulse and then lower the current to the intended level, where it remains there for the duration of the pulse. In literature, it has been reported that a 400 ns overshoot can yield significant acceleration of the heating, and thus by excluding the accelerated portion of the pulse, one can see improved results for the rest of the pulse. In our case, we varied the overshoot, in terms of percentage of the entire pulse duration. This was done as it can be used more directly with any pulse duration rather than using time-based constants. The results are given in figure 5.12, where the overshooting voltage is 5V and the operating voltage is 4V. The amount of observed drift is clearly larger than without the overshoot, and if we were to exclude the overshooting part the total drift is less, however this is not particularly practical, especially for longer overheating durations. Interestingly we observe fast cooling at the switch to the lower voltage, and for lower overheating durations this then returns to the slow heating of the device.

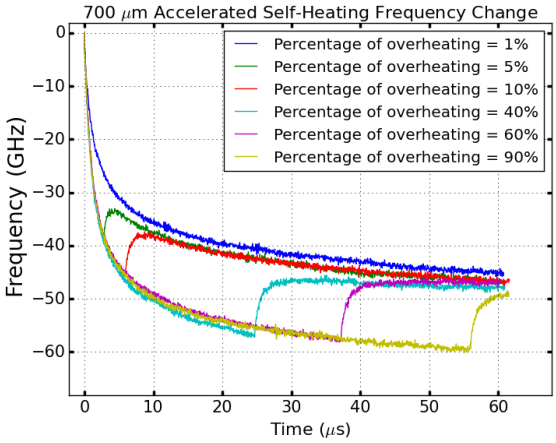

Figure 5.12: Frequency drift under the accelerated self-heating scheme for different percentages of overheating.

This is likely due to the fast thermal response of the active region, but due to the slow thermal response of the surrounding material, i.e. this material has still not been heated up to steady state level. At around 40 % of the pulse, we can see that once the quick cooling of the laser has occurred, the wavelength remains relatively stable, with little drift over the rest of the pulse duration.

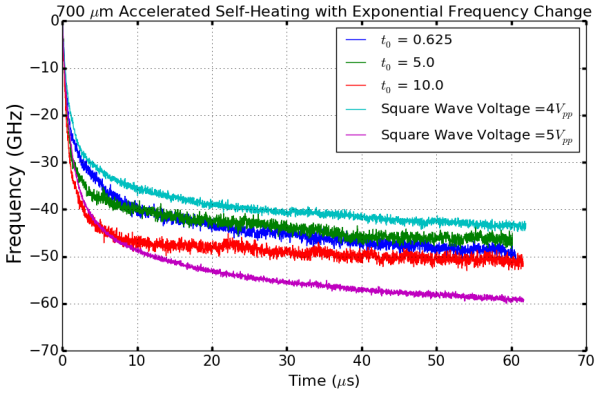

Figure 5.13: Frequency change under the exponential decay scheme, with comparisons from typical square waves.

However, this increased stability at an earlier point is of interest, particularly when wavelength has to be swept or devices have to retuned or

for wavelength switching purposes [78]. Then, we propose to decrease the overshoot level over time instead of instantaneously switching down to the intended level. Keeping the idea of an overshoot, we combined an exponential decay type of wave function, more easily given by the equation,

$$V(t) = V_a + V_b \exp(-\frac{t}{t_0}) \tag{5.2}$$

where, V_a is the operating voltage, V_b is the overshoot voltage and t_0 is the overshooting time constant. We set V_a to 4V and V_b to 1V as to end up at the same level as in the previous approach. The result is shown in figure 5.13. We plotted three time constants for the exponential to illustrate the difference between each of the exponential waves. Square wave signals were also plotted for illustration purposes. It can be seen that the overall drift is in the intermediate region between the 4 and 5 V square waves, which is due to the extra heating due to the exponential on top of the 4 V wave, but less heating than having a full on 5 V square wave. The time taken to reach within 5 and 12.5 GHz of the target wavelength for each pulse is listed in table 5.1.

Table 5.1: Settling time for the exponential decay pulsed-mode scheme and comparison between square wave method.

Time Constant (μs)	Settling Time (5 GHz) (μs)	Settling Time (12.5 GHz) (μs)
4 V square wave	14.0	3.54
5 V square wave	18.9	7.5
0.625	22.94	6.08
5.0	10.66	2.18
10.0	5.56	2.3

It can be clearly seen that there is a significant settling time improvement while using the exponential decay wave except in one case where the time constant is 0.625 μs. The improvement is more than three fold when using the optimised constant for both cases. As expected, we also observe a smooth transition in wavelength, with no instantaneous cooling of the laser device,

due to the voltage transmission being smooth. This faster settling time comes at a cost of a few GHz of drift, due to the extra heating occurring in the exponential part. If this scheme was run for a longer duration however, it would be expected that the wavelength would converge towards the 4 V value.

5.2.3.3 Tunability while under burst mode

The schemes demonstrated in earlier parts of the chapter use pulses to the entire laser to induce lasing and hence changes in wavelength. However, for TWDM purposes it is required that a single laser can tune over several channels. Then, to achieve this, we could not simply just use the lowest voltage/current, which would result in the lowest drift, as this drift is needed for tunability. One method to circumvent this is to use the sub-threshold heating approach, however sometimes this is not enough to meet TWDM standards, particularly as the pulse amplitudes shown here are still relatively low, with larger pulse amplitudes required for further tunability.

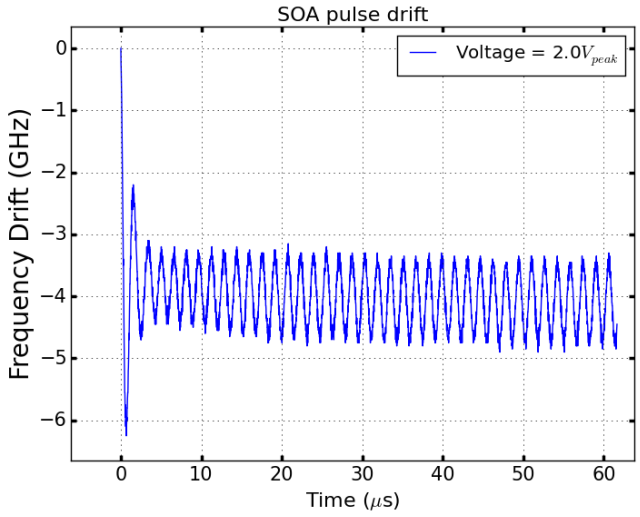

Figure 5.14: Frequency variation when just the SOA is pulsed at 8kHz.

Then, one approach to achieve several channel tunability would be keep the laser in DC bias, but to pulse the SOA section. Then all of the tuning

of the laser is available, with the only wavelength drift being caused due to the SOA turn on. The drift caused by pulsing the SOA to 2V is shown in figure 5.14. We observe a drift of about 6 GHz due to the SOA turn on but then the wavelength seems to oscillate around the 4 GHz mark. This is due to minimal thermal crosstalk between laser sections. One concern that arises from operating in this fashion is the on/off extinction ratio, similar to the sub-threshold heating approach.

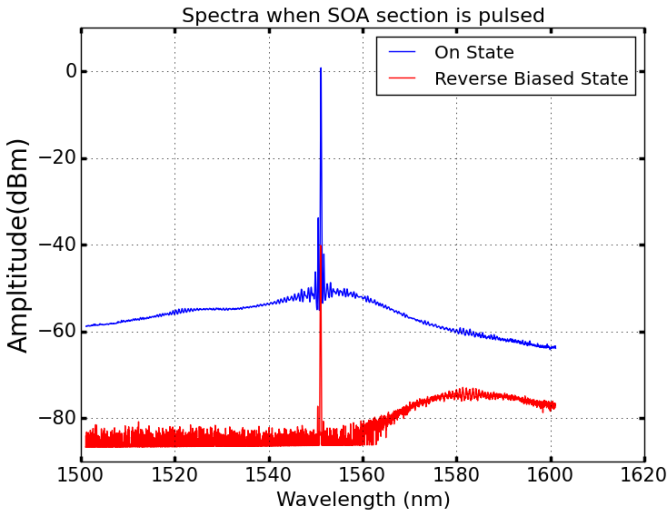

Figure 5.15: Example spectra of the laser when the SOA is in the on state and when the SOA is reverse biased.

To increase the absorption in the off state, we reverse bias the SOA to -1V (a similar approach on an external SOA was performed in reference [79]). The result is given in figure 5.15. Then, for this method, the extinction ratio is 39.24 dB, which unfortunately does meet the TWDM standard. It could however be easily mitigated by designing a slightly longer SOA. Then to acquire a larger extinction ratio, we can perform the same scheme to the one in section 5.2.2.3. This way, our laser goes fully below threshold when turned off and the emission is only the ASE from the grating and the SOA.

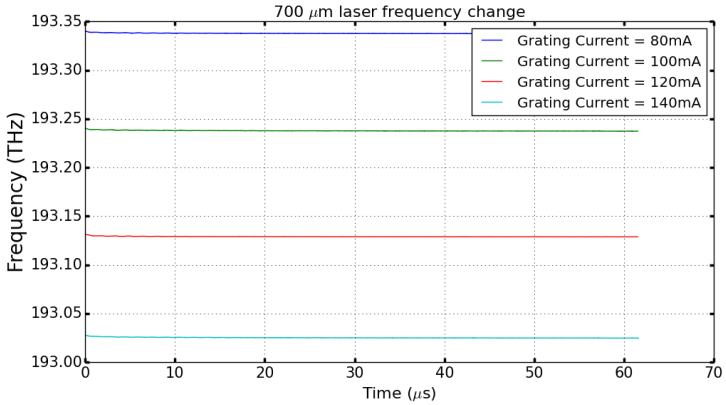

(a)

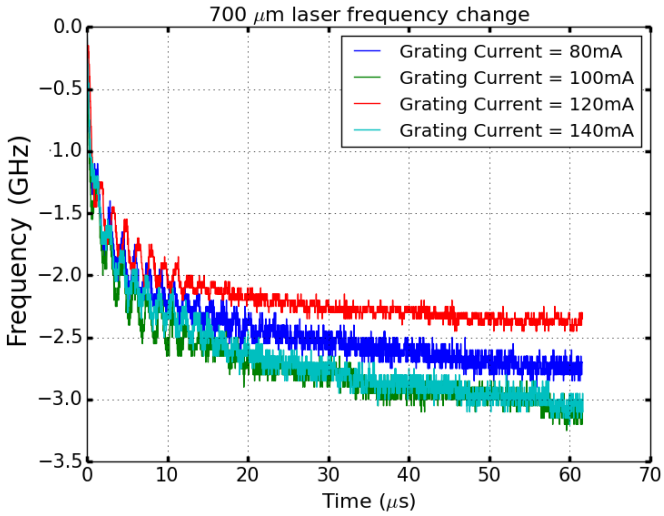

(b)

Figure 5.16: (a) Frequency tuning example while the gain section is under pulsed mode and the grating is tuned in steady state (b) Frequency drift for each of resulting frequency channels.

By using this method we can freely tune the steady state grating current, achieving much wider tunability with the benefit of incurring little wavelength drift. An example of this tunability can be shown in figure 5.16(a). Each of the wavelengths are separated by approximately 100 GHz each, however tighter channel spacings may also be possible via smaller changes in grating current. The frequency drift for each of the respective pulses is shown and it is in agreement with previous measurements as expected, with slight

variations, likely due to measurement error. The spectra in the on-state and off-state can be shown in figure 5.17. The given extinction ratio is 51.1 dB.

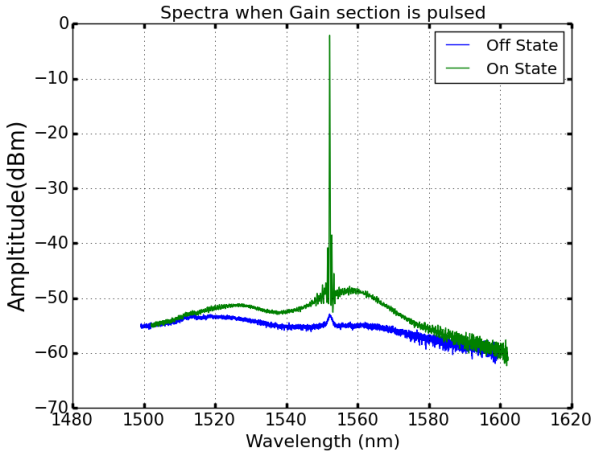

Figure 5.17: Spectra of the laser when the gain section is in the on and off state.

Then, to get largest possible extinction ratio, we also pulse the SOA, and reverse bias it in the off state. The associated spectra are given in figure 5.18.

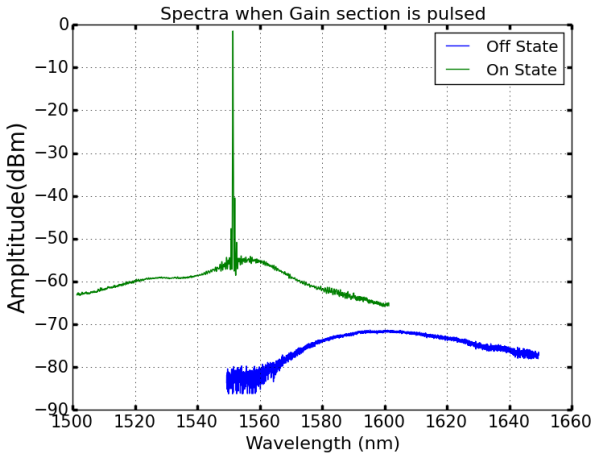

Figure 5.18: Spectra of the laser when the gain and SOA section is in the on/off state.

The extinction ratio in this case is 69.87 dB which is well within the

TWDM standard. However, one thing to keep in mind is that pulsing the SOA as well may come with extra associated drift. The total drift for pulsing the gain and SOA section to a peak of 2V in the on state is then given in figure 5.19,

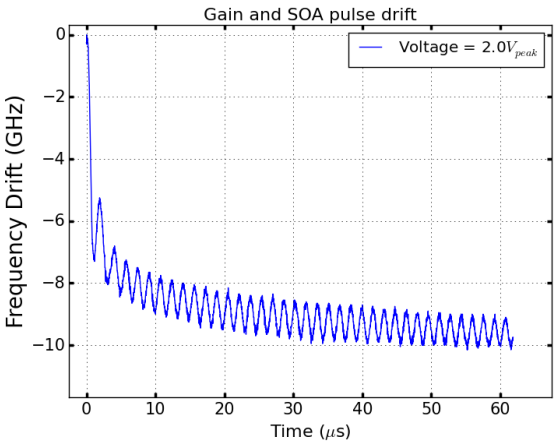

Figure 5.19: Frequency variation when both the gain section and the SOA are pulsed to +2V.

As seen, the observed frequency drift is just slightly less than if the gain section was pulsed on its own. This is due to some of the current being shared with the SOA, reducing the overall self-heating of the gain section and lowering the frequency drift.

5.3 Transient CCD-Thermoreflectance Measurements

In the two previous sections, we used the wavelength discrimination technique to acquire the change in wavelength over time when our devices are under pulsed mode operation. This was attributed to thermal effects as opposed to carrier effects, and could be clearly seen as the frequency was red-shifting with increased current. In effect, we were using wavelength as a probe to examine the change in average device temperature. In this section, we will examine the transient thermal behaviour of our laser in a more direct fashion via thermal imaging. CCD-Thermoreflectance imaging was our method of choice due to it being non-invasive and having sub-micron resolution. The break down of the setup and theory of this imaging method is given in the next section.

5.3.1 Theory and Setup

Both steady state CCD-TR [66, 80] and transient CCD-TR [81, 82] are well documented and understood techniques in literature. They have been used in many cases to acquire thermal profiles of optoelectronic devices [83–86]. The techniques are based on the principle that if material temperature changes, then its refractive index will also change. As reflectivity of any material is dependent on the refractive index, then naturally reflectivity will also change. Thus, we can then say that the relative change in reflectivity is related to a change in temperature, or more specifically can be approximated to first order by,

$$\frac{\Delta R}{R} = (\frac{1}{R}\frac{\partial R}{\partial T})\Delta T = \kappa \Delta T \tag{5.3}$$

where κ is known as the thermoreflectance coefficient, and is typically on the order of 10^{-4}-$10^{-6}\mathrm{K}^{-1}$ [87] depending on the material being imaged, the numerical aperture of the setup and illuminating wavelength. For our imaging purposes, the surface material covering our lasers is gold and thus the thermoreflectance constant is on the order of 10^{-4} K^{-1} [59]. In our case

the cause of temperature change is resistive heating due to current injection and so, the change in temperature between two different current injection states can be obtained by illuminating the sample in question, collecting the reflected light by a detector, and comparing the change in received light from the two states. This is the basic operating principle of any thermoreflectance system. In the case of CCD-TR, a CCD camera is used as a detector due it being a multi-point detector, i.e. it contains many pixels, which can act as individual detectors resulting in the ability to take images of entire devices in one go, without having to use complex laser scanning setups with single-point photodiode detectors. Due to this we can use a simple LED light source to illuminate the sample. As each pixel of the camera will record the intensity (I), we can simply get the intensity of light received by the camera at one current (I_1) versus another current (I_2), and thus, giving the temperature difference between the two states as,

$$\Delta T = \frac{1}{\kappa}\frac{I_1 - I_2}{I_1} \tag{5.4}$$

Typically for our purposes, the state represented by I_1 is recorded with the device under no current injection, thereby designated I_{cold}, and then I_2 will be the state represented by some current injection (I_{hot}). However, due to κ being small, we are required to use a lock-in technique, known as homodyne detection. For steady state CCD-TR, the sample is injected with square wave current pulse of frequency (f, typically 10-20 Hz), with the camera being triggered at twice that rate (2f), taking two images per cycle, one in the I_{cold} state and one in the I_{hot} state. The exposure time of the camera is set in such a way that the camera only records the end of the laser pulses, effectively catching steady state conditions. These are then averaged and the end result can be plotted as heat-map. For transient CCD-TR, the setup is typically more complex although the fundamental principle of CCD-TR remains the same. A schematic of the setup and a real world image of the setup used by our group is shown in figure 5.20

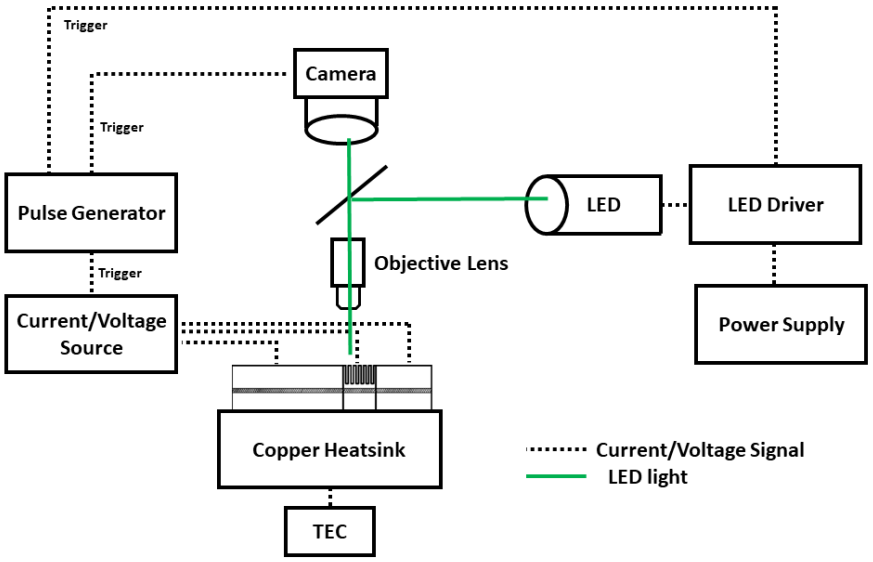

(a)

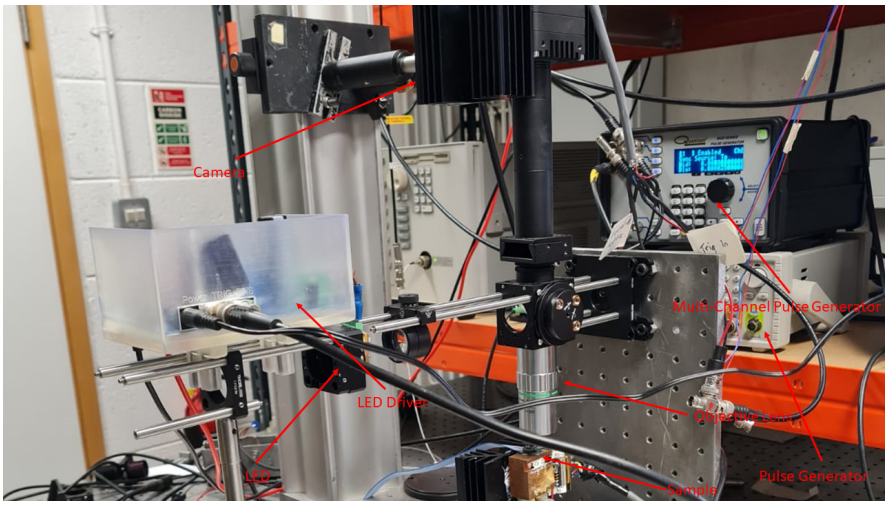

(b)

Figure 5.20: (a) Transient CCD-TR setup schematic. (b) Transient CCD-TR real world setup image.

Typically, scientific grade CCD-TR cameras are limited to frame rates of up to 500 Hz, which then limits the transient behaviour which can be observed. As seen earlier, our lasers exhibit thermal phenomena on the micro/nano-second regime. The solution used for this work is to still use the rather slow scientific camera (ORX-10GS-51S5M-C) in conjunction with

a high power pulsed LED, powered by a custom LED driver. The pulse duration of the LED then effectively acts as a shutter to the camera, thus reducing the exposure time to the pulse duration of the LED. It can then be inferred that by reducing the LED pulse duration, thermal transients could be observed on a much faster time frame. In an ideal scheme of this setup, we would have one pulse to our sample, and one LED pulse per camera frame, with a precisely known phase relationship of each of these components. Then, by adjusting the phase between the LED pulse and the sample pulse, a full transient thermal profile can be acquired. However in our case, the LED is not capable of producing enough light in a single pulse (when LED pulse duration is 2μs) for the camera to be able to see the sample. Hence, instead we use eight LED pulses and eight pulses of the sample at the same phase relationship per one camera frame. This obviously increases the intensity of the light received by the camera eight-fold, and is enough for our sample to be seen. To get our "cold" image, we then run another frame where the sample is not pulsed, but the LED is, at the same time as if the sample was pulsed. Then we can get the change in temperature as per equation 5.4. A timing illustration of this setup is shown in figure 5.21.

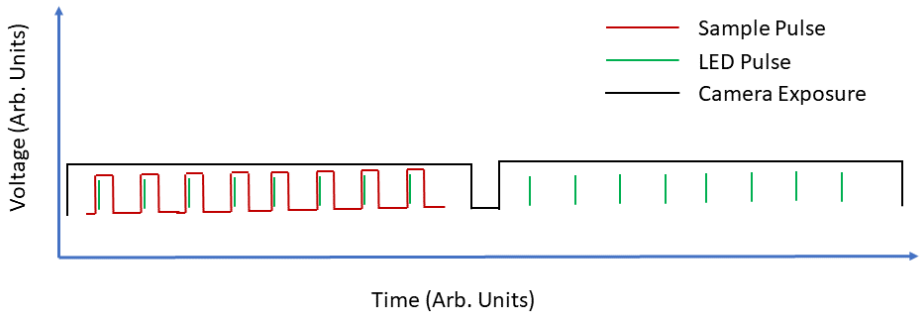

Figure 5.21: Timing schematic for our transient CCD-TR setup.

5.3.2 Results

Then, using the outlined setup, we have conducted several tests. Our laser pulse duration was set to 2 ms, while the currents/voltages were varied. The

LED pulse duration is set at 2 μs and so this is our time resolution. The thermoreflectance constant has been calibrated as -3.4×10^{-4}, with the steady state constant being -1.4×10^{-4} for this setup. This difference in thermoreflectance constant is due to removal of the 514 nm bandpass filter, which would decrease measurement sensitivity due to measuring some of the reflectance away from the thermoreflectance peak, however it was necessary for enough light to be able to reach the camera for the laser to be visible.

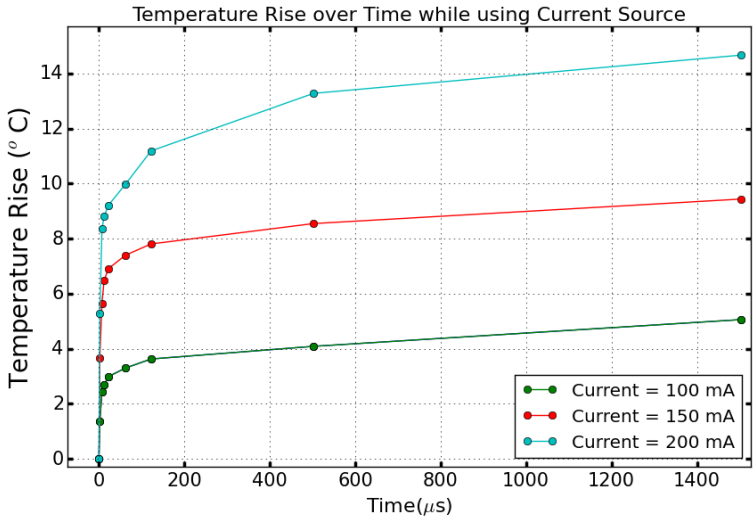

Figure 5.22: Temperature Rise when the entire laser is pulsed using the current source for various currents.

First, we tested the transient thermal dynamics when the laser was pulsed using a current source, similar to section 5.2.2.1. There were three reasons for this. One was that steady state results of our devices were readily available and published [59], then at the end of these long pulses we would expect the temperature values to agree. Secondly, for comparison with the drift values shown in section 5.2.2.1. Thirdly, end results should also agree with the thermal impedance data. The results are shown in figure 5.22, with sample images for some of the heating steps shown in figure 5.23. We see the same behaviour as observed in the wavelength discrimination data, where we observe a sharp rise in surface temperature, accompanied by a slow but steady increase in the long run.

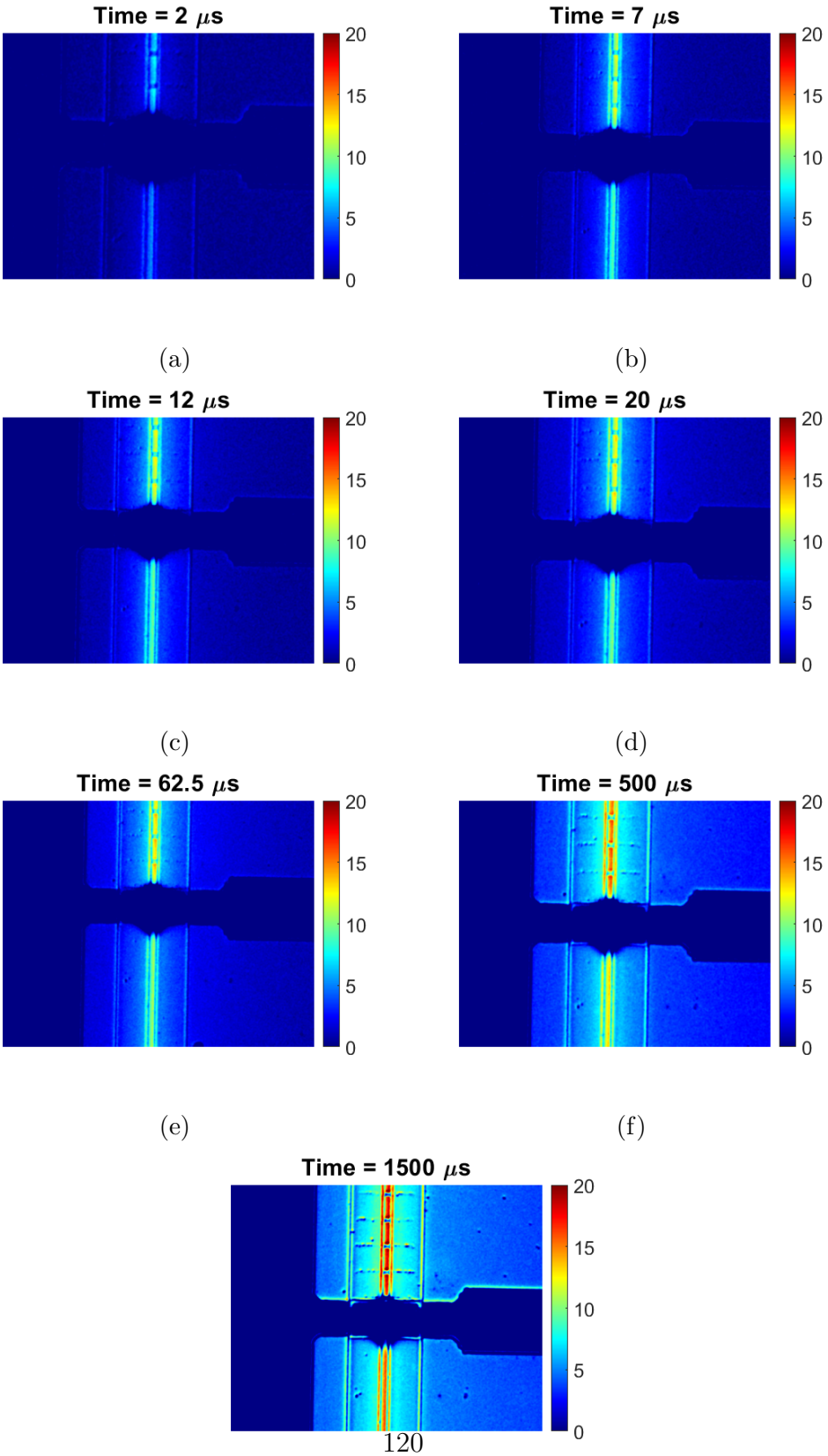

Figure 5.23: Thermal images at different times when the entire laser is pulsed using the current source at 200mA.

Taking the data from 5 μs, the total temperature rise is given in table 5.2, with the conversion to frequency drift included, assuming 12.5 GHz/1 ^oC. Then, comparing this data to the wavelength drift given in section 5.2.2.1, we can see that we achieve a larger amount of heating than seen via the wavelength discrimination method, however, as mentioned in a previous chapter, surface temperatures will be higher than the ones in the bulk of the laser due to a larger voltage drop at the pn-junction, which is closer to the surface, and thus this result could be a consequence of this phenomena. Thermal impedance is also observed to be lower than that given in previous results, however as the temperature has not settled yet, this would likely be remedied by observing longer pulses.

Table 5.2: Temperature Rise and Frequency comparison between wavelength discrimination results for when the entire laser is pulsed using the current source.

Current (mA)	T_{rise} (from 5μs) (^oC)	Frequency Drift (GHz)	TI*L (^{o}C μm/mW)
100	2.63	32.88	26.74
150	3.8	47.5	25.38
200	6.2	77.5	25.77

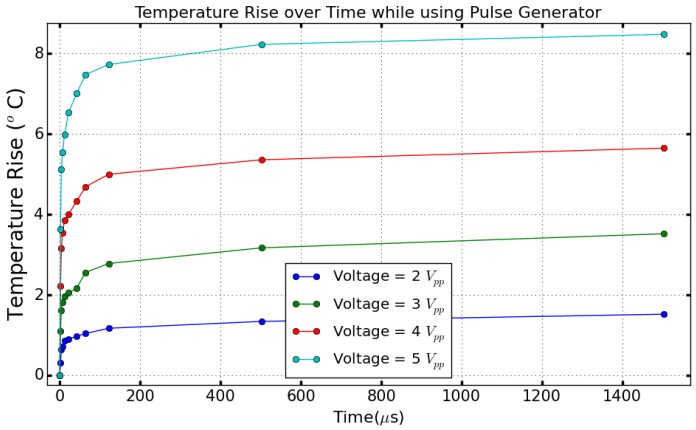

Figure 5.24: Temperature Rise when the entire laser is pulsed using the function generator for various currents.

We then ran comparison measured for the voltage pulse schemes in section 5.2.2.2 for the 700 μm device. As these pulses maintain a rise time of 300 ns, we now instead look at the heating that occurs from the beginning. The data is presented in figure 5.24, with heat-map images of a sample set shown in figure 5.25. The total amount of temperature rise that occurred until 62.5 μs (which was the duration of our pulses in section 5.2.2.2), is tabulated in table 5.3 below for comparison reasons. As observed, the wavelength drift which has been previously documented via the wavelength discrimination technique is shown to be significantly smaller.

Table 5.3: Temperature Rise and Frequency comparison between wavelength discrimination results for when the entire laser is pulsed using the function generator.

Voltage (V_{pp})	T_{rise} (until 62.5μs) (^oC)	Calculated Frequency Drift (GHz)
2	1.04	13
3	2.56	32
4	4.69	58.625
5	7.48	93.5

Particularly for the 5V case. One of the reasons could be due to the aforementioned effect where the surface temperature is observed to be higher than the active region. Another could be that we are including 300 ns of heating which is not shown in the wavelength discrimination method due to the inability to measure wavelength change during the rising portion of pulses, which could be substantial and offset the agreement between the two measurements.

Finally, we draw a comparison between the pulses demonstrated in section 5.2.2.3. These resulted in the least wavelength drift and thus should result in the lowest temperature rise. As the signal is low, it becomes more challenging to separate it from background noise and thus, for this reason, for the 1V case, the transient data has been excluded, as any of the data in the early stages of the pulse is obscured by the noise.

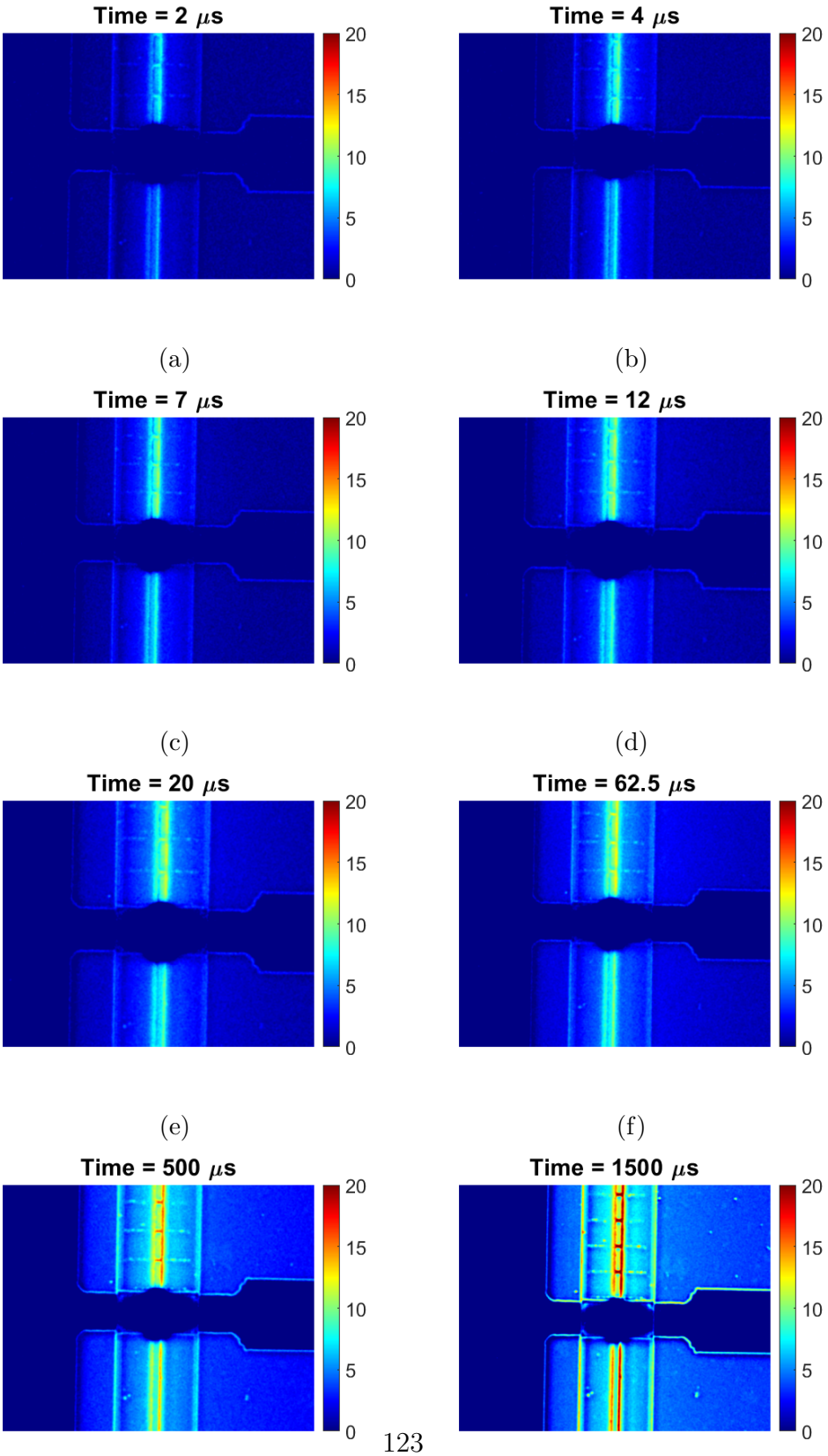

Figure 5.25: Thermal images at different times when the entire laser is pulsed using the function generator for 5 V pulses.

It should be noted that the overall temperature rise for this pulse was recorded at 0.33 ^oC at 1.5 ms, indicating that nearly double the frequency drift occurs in the 62.5 μs to 1.5 ms window. The transient data for the 1.5 and 2 V cases is presented in figure 5.26.

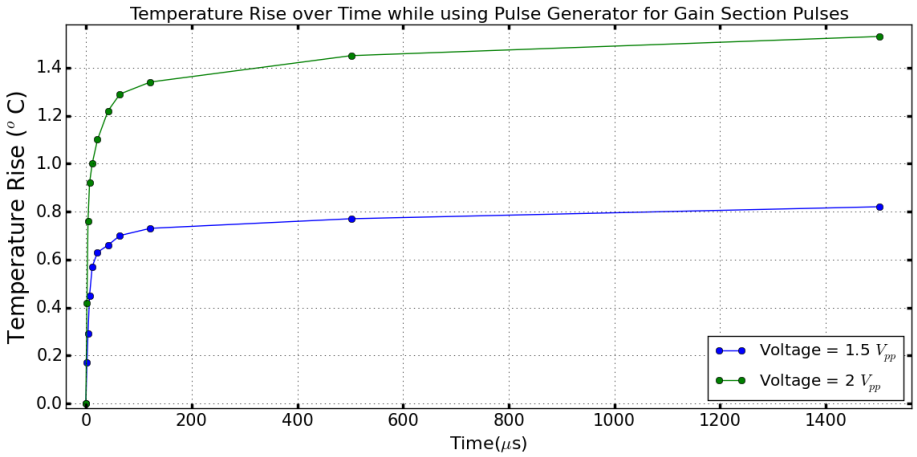

Figure 5.26: Temperature Rise when just the gain section is pulsed using the function generator for various currents.

The temperature change to 62.5 μs, with its equivalent frequency drift is then listed in table 5.4.

Table 5.4: Temperature Rise and Frequency comparison between wavelength discrimination results for when only the gain section is pulsed using the function generator.

Voltage (V_{pp})	T_{rise} (until 62.5μs) (^oC)	Calculated Frequency Drift (GHz)
1.5	0.7	8.75
2	1.29	16.125

Similarly to previous results, we observe some discrepancy when compared to wavelength discrimination data, however this appear to be smaller than in the previous cases, likely due to the shorter rise time, meaning more of the wavelength drift was observed by the wavelength discrimination technique than in the other cases.

Another advantage of this CCD-TR method is that it can be used to not only observe the heating of the laser over an electrical pulse, but it can also be used to observe the cooling, simply by aligning the LED pulse at positions just after the laser pulse. An example result for the gain section 2V pulse is given in figure 5.27.

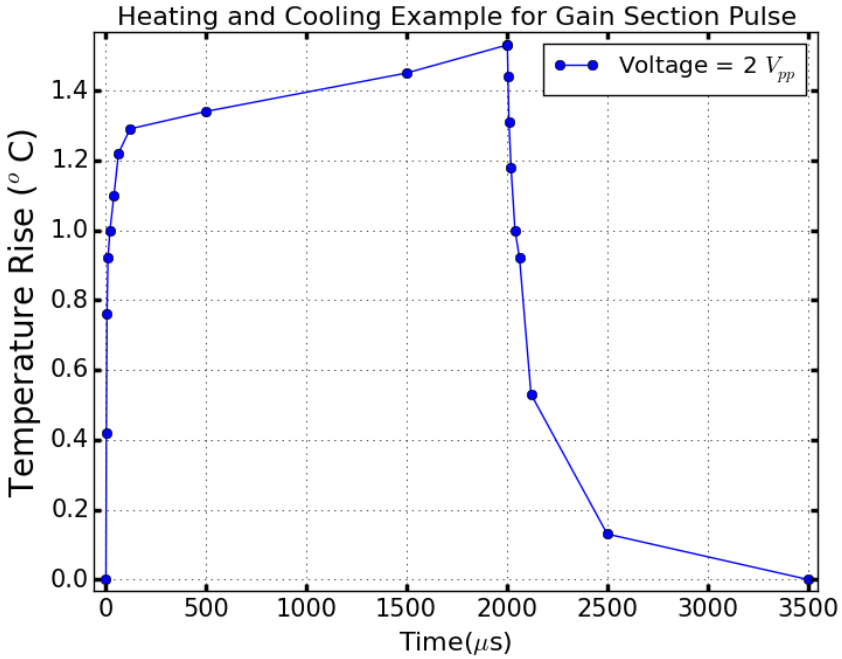

Figure 5.27: Temperature rise and cooling when only the gain section is pulsed using the function generator.

Similarly to the heating, we observe a fast cooling effect. The observance of this effect may be useful in explaining the results in section 5.2.3.2, where we can see a very fast change in frequency with a reduction in voltage, however further investigation would be needed to confirm. Note, the last data point in the graph is a bit ambiguous as the temperature recorded is so low, that the image is dominated by noise, hence it was set to zero.

5.4 Conclusion

In this chapter, we have used the wavelength discrimination method to characterise the transient wavelength dynamics of our lasers under pulsed mode operation. It was determined that pulsing just the gain section, with low pulse amplitudes yielded the best results in terms of frequency stability ($\pm$ 2 GHz). A series of compensation techniques which were previously shown in literature were then tested, and their performance was recorded. Based on these results, a new technique, named exponential decay heating was devised which significantly reduced the frequency settling time of our devices. Transient thermal imaging was then used to image the surface of our lasers and to compare the resulting thermal transients to wavelength discrimination measurements. It was found that there was some discrepancy, however this difference between CCD-TR surface measurements and bulk measurements has been previously reported. Overall, we have demonstrated that our devices are capable transmitters for the emerging TWDM-PON networks, meeting many of the recommendations listed by ITU.

Chapter 6

Conclusions and Future Work

6.1 Conclusions

The ultimate objectives of this thesis were to achieve continuous wide range athermalisation in the steady state and frequency stable pulsed mode operation of ridge-waveguide, all-active surface grating lasers.

To achieve wide range athermalisation, we first needed to decide which devices were most suitable for this purpose. This was done in chapter 3. One of the conclusions from theory derived in chapter 3 was that for wide range athermalisation, devices need to be capable of operating under large current injection at room temperature. Then, single period devices were quickly deemed not suitable due to their FSR-mode hop far outside of the C-band, and thus triple period devices of different lengths were tested. It was observed that 700 μm long devices had optimal performance for this scenario. Another conclusion from theory was that these devices also need to perform well while under relatively low current injection at high ambient temperature. Better performance for gain peak detuned wavelengths at higher ambient temperatures has been previously reported for several parameters, and thus we tested our 700 μm lasers at various wavelengths to determine what the optimal detuning was for high temperature, low current injection operation. It was found that a gain peak detuning of approximately +20 to 25 nm yielded the best results in terms of maintaining optical out-

put power and SMSR. While operating at relatively low currents and high ambient temperature, the laser was operating relatively close to threshold. To maximise the athermalisation range, it is thus of interest to lower laser threshold at higher temperatures as much as possible. While this is one of the consequences of using a gain peak detuned laser, another optimisation can be made. Namely, as both tuning sections have gain, and one of these sections experiences significantly more loss (grating section), there must be an optimal set of currents that would push the device above threshold. Detailed analysis of this two current threshold nature was performed and it was found that the gain section had an almost four time larger impact on device threshold for 700 μm long lasers than the grating section. As a consequence it was then seen that the athermal range would almost always be limited by gain current.

Then, in chapter 4, using the aforementioned results to choose an optimal device, a red-shifted 700 μm laser was then athermalised and a detailed account of its laser parameters along the athermal path was maintained. The operating range achieved was 5 to 106 ^{o}C continuously and to 115 ^{o}C discontinuously while maintaining a wavelength stability of $\pm$0.4 GHz/0.003 nm and SMSR above 30 dB throughout the entirety of the athermal operation. Output power was observed to remain relatively stable until 80 ^{o}C, with an increasingly rapid decline at higher ambient temperatures. Using the SOA, stable output power to within $\pm$ 0.005 dBm could be maintained up to 92 ^{o}C, after which the SOA saturates. This wide range athermal performance was the largest recorded to date. Then, as each laser diode is required to cover several wavelength channels, our device was athermalised over different wavelengths on the ITU grid. Detailed performance of each channel was shown, with bluer channels showing reduced athermal range and increased wall plug efficiency. Finally, as a consequence of athermalisation measurements, a new method to measure thermal impedance of our devices was developed. Using this method, the thermal impedance length product was determined to be 29.3$\pm$2.1 ^{o}C μm/mW for the gain section and 39.33$\pm$2.8 ^{o}C μm/mW for the grating section of the two section single mode lasers.

In addition to good steady state performance, the new optical commu-

nications standard TWDM requires wavelength stable pulsed performance as well. Thus, in chapter 5, our devices were also examined while under pulsed mode operation using the wavelength discrimination technique, with detailed results presented. Different device lengths were revisited for the transient study and it was determined that 700 μm devices could achieve the lowest frequency drift of $\approx$ 2.5 GHz while only the gain section was pulsed with a low voltage square wave. Compensation techniques which have been reported in literature were examined, with sub-threshold heating yielding a 6 GHz improvement for all pulse voltages and accelerated self-heating only yielding improvements in wavelength stabilising time. From the latter result, a new pulsed method, named exponential decay heating was developed which yielded significantly improved wavelength stabilising time which could be useful in laser retuning scenarios or for optical switch purposes. Transient thermal performance of our lasers was also examined using the transient CCD-TR technique, with the thermal results showing a slight discrepancy from the wavelength discrimination results, however this is likely a result of imaging the surface of the laser, rather than the active-region.

6.2 Future Work

6.2.1 Improved Design for Athermal Operation

All of the work performed within this thesis occurred using devices which were not designed for athermal operation and thus it would be of particular interest to redesign these devices with athermal performance in mind. To some extent, this has been performed in the PhD thesis of Michael Wallace [36], however, incorporating the findings within this work should lead to even better designs. A preliminary simulations study using the time domain transfer matrix method (TD-TMM), more details on which can be found in references [35, 36, 88], has shown that by simply shifting the Bragg peak

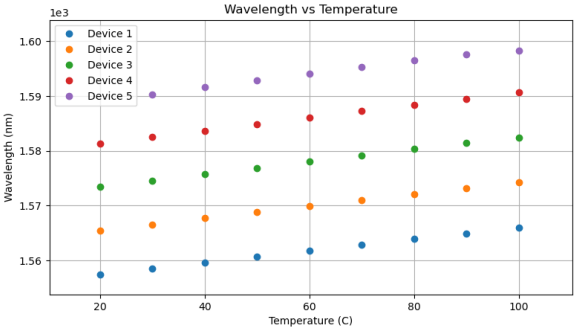

(a)

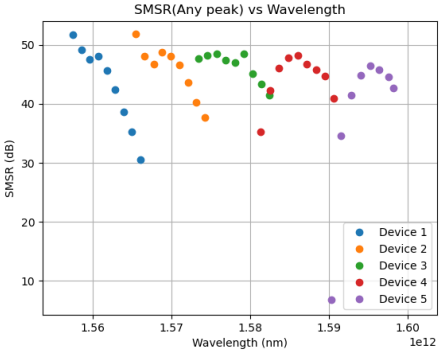

(b)

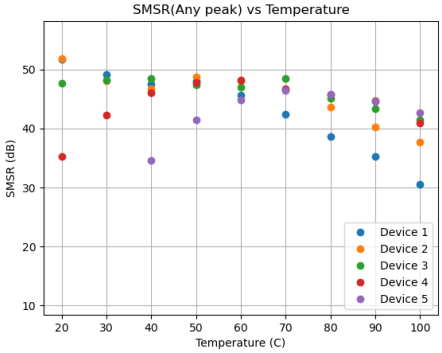

(c)

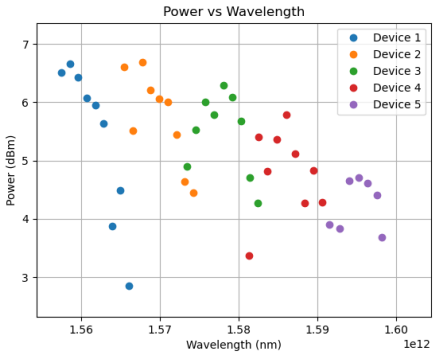

(d)

Figure 6.1: Simulated array of five Bragg-grating shifted lasers with (a) Wavelength (b) SMSR versus wavelength (c) SMSR (d) Power versus wavelength, all while being temperature tuned at 10 ^{o}C steps.

wavelength to the red side of the gain peak for all devices on the array, there is significantly better performance over a wide range of temperatures

than the devices used within this thesis.

The results of this preliminary study, for 700 μm device lengths are shown in figure 6.1. In this case, five devices are capable of covering more than 50 nm, experience less SMSR and power loss and can operate to higher temperatures than the devices operated in this thesis (see section 3.4). Further optimisation using this model could likely yield even more suitable devices for high temperature operation and thus athermal operation.

One other aspect of optimisation for athermal operation could be an investigation into 400 μm devices. Shorter laser devices have many desired attributes, such as operating at lower input powers, higher SMSR and increased modulation response, however our 400 μm devices are not capable of operating past 70 ^{o}C ambient temperature as they fall below threshold for all currents. This is a major issue for athermalisation, and the likely cause is the high loss of the grating combined. Optimisation of the grating structure specifically for the 400 μm devices could potentially yield improved athermalisation results, even when compared to 700 μm devices and thus could be a further study prospect.

6.2.2 Research into O-band devices

The focus of this research focused on operation within mostly the C-band. However, our group has received devices which are capable of operating in the O-band, with the same ridge-waveguide, all-active surface grating design. The grating parameters have been varied to be centred in O-band wavelengths, namely via changes to period length/order. One particular advantage of operating in the O-band (1260 to 1360 nm) is the lack thereof or low chromatic dispersion, allowing directly modulated signals to cover large distances without compensation. Thus, athermalisation and transient research using these devices could be of interest. Some preliminary athermalisation data is shown in figure 6.2. The total athermal range in this preliminary study for a 700 μm long laser is 60 ^{o}C, when operating in the discontinuous tuning regime. An unavoidable mode hop occurs early in the athermal range, and the reason for this is unknown. Further study is required. Furthermore,

the relatively low athermal range is also a point of interest, considering that relatively high currents are used, which are shown in figure 6.3. Perhaps the design is faulty, or the manufacturing process was faulty. A further investigation is needed. In particular, thermal imaging using CCD-TR could identify potential hotspots and heating irregularities which could be the cause of such a mode hop. Scanning electronic microscopy (SEM) could also be another avenue to examine structural damage. If these tests show no abnormalities, further characteristic and simulation studies would be required.

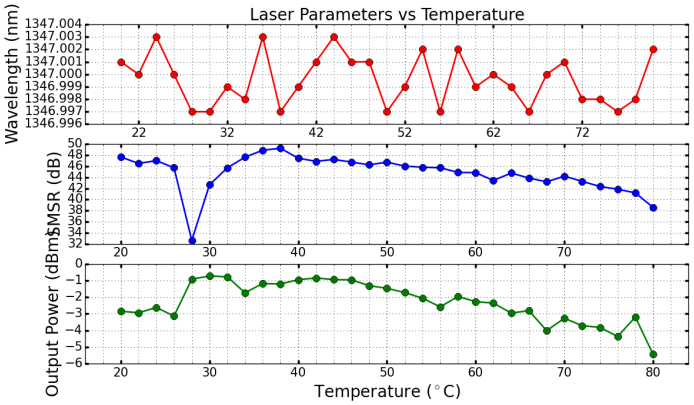

Figure 6.2: Change of laser parameters as the O-band laser is athermalised.

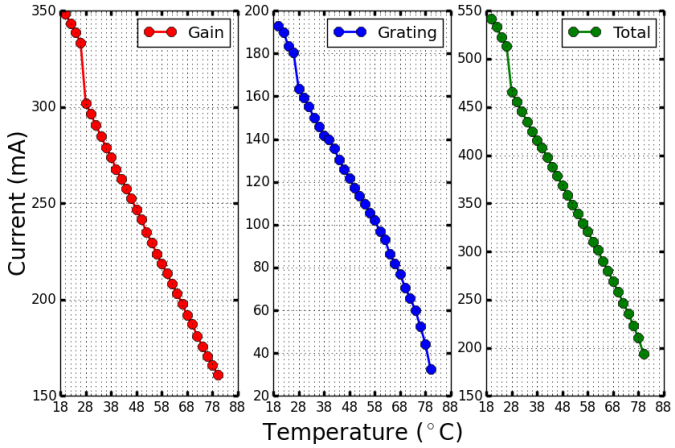

Figure 6.3: Change of current as the O-band laser is athermalised.

6.2.3 Further Transient Characterisation, Technique Development and Transmission

While substantial transient characterisation has been done on the devices in question, it would be of interest to continue and develop more techniques for wavelength stabilisation. As TWDM is the up and coming optical communications standard, another area of research could be athermal pulsed mode operation, which has not been examined here in detail. This can prove to be rather challenging to achieve as differing pulse amplitudes would be required at different ambient temperatures, resulting in varying frequency drift, more than likely outside of the allowed limits. One solution has been proposed in this text, which is to pulse the SOA, however this would require an updated (longer) SOA design due to not having a high enough extinction ratio.

Another area of study for transient characterisation is to develop techniques to look into other properties that can vary over time. For example, within this text, SMSR is assumed to be exactly in line with the steady state SMSR while under pulsed mode operation, which may not be the case, particularly when differing laser sections are not pulsed with equal current density. A method to measure the change of this property over time would be particularly useful.

Further investigation into the transient CCD-TR technique could also be an avenue of interest. Limited study has been provided in this thesis and having a look at the compensation schemes used here using thermal imaging could reveal interesting laser dynamics. Furthermore, it could allow for easy determination of what is a thermal effect and what is a carrier effect.

In a real world scenario, the pulsed mode signals that we have demonstrated would also have data applied to them via either direct or external modulation. If using direct modulation, adiabatic chirp has been shown to be a significant problem requiring compensation techniques or optimised laser structures to solve [89, 90]. This could significantly reduce the signal reach due to chromatic dispersion. A potential pathway of study could be in measuring this chirp, and seeing its effect on transmission distance for these devices, however, this was not carried out for this study as it requires

packaged devices with impedance matching. As for external modulation, preliminary measurements, while pulsing the SOA, were carried out using the setup in figure 6.4.

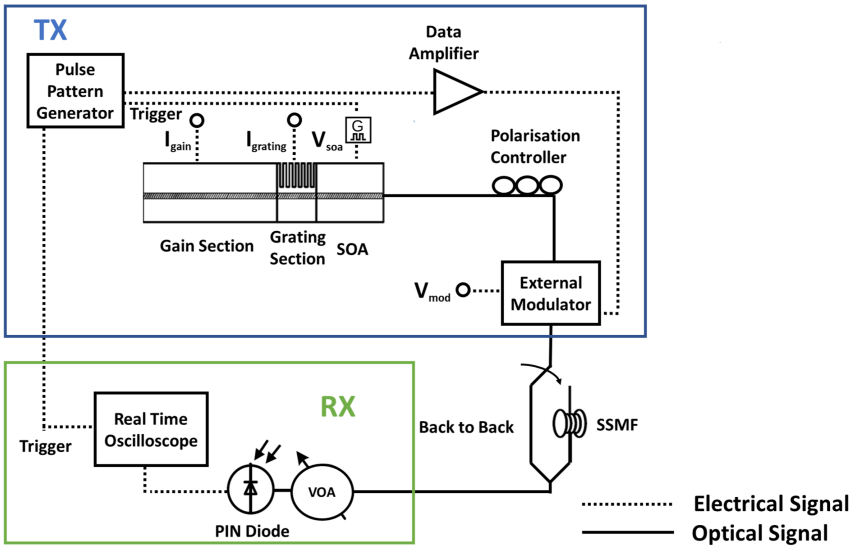

Figure 6.4: Burst mode transmission setup using an external modulator to modulate our light signal. The gain and grating sections remain in steady state operation, with the SOA being pulsed.

The ambient temperature was maintained at 20 ^oC, pulse duration was set to 1.4 μs with the pulse frequency at 8 kHz and pulse amplitude to the SOA set at +2 V with the data modulation signal being applied 70 ns after the forward bias signal is applied to the SOA, for 1.28 μs. This gives us a guard time of 70 ns at the beginning of the burst and no guard time at the end, totalling 1.4 μs when including the 50 ns fall time of the optical pulse. This guard time is well within the 128 ns requirement for TWDM. It should be noted that guard time for TWDM refers to time before modulation is applied to the optical signal, specifically to allow any power fluctuations due to electrical overshoot or rise times to settle down into a steady state. The reduced burst duration was implemented due to equipment limitations resulting in a distorted signal at longer durations due to low frequency cut-off. Then, the light from the laser is collected through a polarization controller, from which it passes into a Mach-Zehnder modulator, within which it is

modulated at 10 Gb/s using the On Off Keying (OOK) modulation format. OOK refers to the most basic amplitude modulation format, for which light which is unaffected by the modulator is referred to as a "1" and light which is destructively interfered and significantly reduced in amplitude is referred to as a "0". The modulated signal is then transmitted either straight to the receiver (back-to-back) or through 25 km of Standard Single Mode Fibre (SSMF). A 10 GHz avalanche photodiode (APD) is used to detect the optical burst and the resulting photocurrent is sampled by a real time oscilloscope operating at 50 GSa/s. The obtained real-time data is then processed offline to access the performance, qualitative analysis is performed by producing eye diagrams and quantitative analysis by calculating the Q-factor from the obtained real-time data. Knowing the Q-factor, the bit error-rate can be calculated. Q-factor and BER formulae are given in equations 6.1 and 6.2 respectively [91],

$$Q = \frac{\mu_1 - \mu_0}{\sigma_1 + \sigma_0} \tag{6.1}$$

$$BER = \frac{1}{2} erfc(\frac{Q}{\sqrt{2}}) \tag{6.2}$$

where μ_1 and μ_0 are the mean values of the 1 and 0 levels respectively, σ_1 and σ_0 are the standard deviation of the 1 and 0 levels respectively and erfc is the complimentary error function. The Bit Error Rate measurements were carried out as a function of received pulse power for both, back-to-back (red circles) and 25 km of SSMF (black squares) scenarios. The observed received peak pulse power for error free (10^{-9}) performance is -11.5 dBm for the back to back and -10.0 dBm for the 25 km of SSMF, which corresponds to -30.5 dBm and -29 dBm of average power respectively. This corresponds to only a 1.5 dB of power penalty after transmission through 25 km of SSMF. This power penalty is due to dispersion. It can be seen in the eye diagrams that are shown as an inset in figure 6.5 that the 1 and 0 amplitudes have a larger deviation, meaning their Q factor will be lower and result in a lower bit error rate.

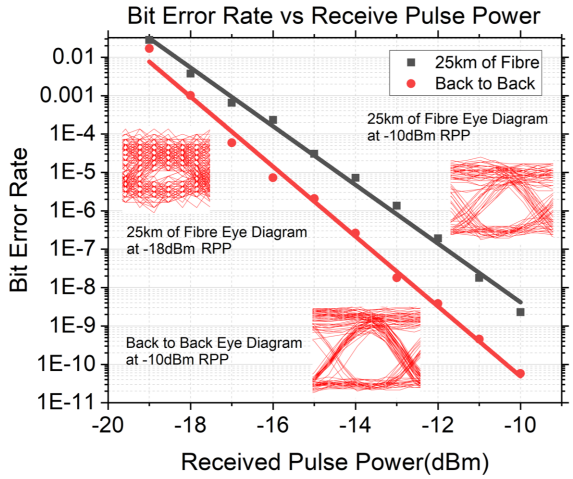

Figure 6.5: Burst mode transmission setup using an external modulator to modulate our light signal. The gain and grating sections remain in steady state operation, with the SOA being pulsed.

Furthermore, peak pulse power when fibre coupled was +5 dBm hence, the power budget in this system is 15 dB. This is relatively low when compared to other systems, however this is caused by a non-sufficiently high swing voltage output by the data amplifier, which was not able to make use of the full modulation characteristic of the modulator and hence yielded a lower extinction ratio between the 1 and 0 bits resulting in suboptimal performance. Then, the natural next step is to replace the data amplifier and repeat these measurements, and not only for the SOA bursting case but for all of the other scenarios described within this thesis. Similarly, other schemes such as pulsed amplitude modulation, 4 level (PAM4) or 8 level (PAM8) could also be tested.

6.3 Final Thoughts

The research work in this thesis shows that there is still much to investigate in semiconductor lasers. The next generation of devices will need to be more energy efficient and therefore will require better understanding of the physics of such devices. A start has been made on this with a new computational model that includes carrier and thermal effects to properly design the lasers.

Bibliography

[1] J. Baggott, "Planck's Derivation of E=hv: The Quantization of Energy," in *The Quantum Cookbook: Mathematical Recipes for the Foundations for Quantum Mechanics* (J. Baggott, ed.), p. 0, Oxford University Press, Jan. 2020.

[2] A. B. Arons and M. B. Peppard, "Einstein's Proposal of the Photon Concept—a Translation of the Annalen der Physik Paper of 1905," *American Journal of Physics*, vol. 33, pp. 367–374, May 1965. Publisher: American Association of Physics Teachers.

[3] J. P. Gordon, H. J. Zeiger, and C. H. Townes, "The Maser—New Type of Microwave Amplifier, Frequency Standard, and Spectrometer," *Physical Review*, vol. 99, pp. 1264–1274, Aug. 1955. Publisher: American Physical Society.

[4] T. H. Maiman, "Stimulated Optical Radiation in Ruby," *Nature*, vol. 187, pp. 493–494, Aug. 1960. Number: 4736 Publisher: Nature Publishing Group.

[5] A. Javan, W. R. Bennett, and D. R. Herriott, "Population Inversion and Continuous Optical Maser Oscillation in a Gas Discharge Containing a He-Ne Mixture," *Physical Review Letters*, vol. 6, pp. 106–110, Feb. 1961. Publisher: American Physical Society.

[6] N. T. Melamed, C. Hirayama, and E. K. Davis, "Laser action in neodymium-doped glass produced through energy transfer," *Applied*

Physics Letters, vol. 7, pp. 170–172, Sept. 1965. Publisher: American Institute of Physics.

[7] J. E. Geusic, H. M. Marcos, and L. G. Van Uitert, "Laser oscillations in Nd-Doped Yttrium Aluminium, Yttrium Gallium and Gadolinium Garnets," *Applied Physics Letters*, vol. 4, pp. 182–184, May 1964. Publisher: American Institute of Physics.

[8] R. N. Hall, G. E. Fenner, J. D. Kingsley, T. J. Soltys, and R. O. Carlson, "Coherent Light Emission From GaAs Junctions," *Physical Review Letters*, vol. 9, pp. 366–368, Nov. 1962. Publisher: American Physical Society.

[9] Z. I. and R. F. Kazarinov, "Semiconductor laser with electric pumping," Inventor's Certificate 181737 [In Russian], Appli. 950840, 1963.

[10] H. Kroemer, "Semiconductor laser with electric pumping," U.S. Patent 3 309 553, (Filed Aug. 16, 1963), 1967.

[11] Z. I. Alferov, "Electroluminescence of heavily-doped heterojunctions pAlxGa1-xAs-nGaAs," *Journal of Luminescence*, vol. 1-2, pp. 869–884, Jan. 1970.

[12] R. D. Dupuis, P. D. Dapkus, N. Holonyak, E. A. Rezek, and R. Chin, "Room-temperature laser operation of quantum-well Ga(1-x)AlxAs-GaAs laser diodes grown by metalorganic chemical vapor deposition," *Applied Physics Letters*, vol. 32, pp. 295–297, Mar. 1978. Publisher: American Institute of Physics.

[13] A. R. Adams, "Band-structure engineering for low-threshold high-efficiency semiconductor lasers," *Electronics Letters*, vol. 22, pp. 249–250, Feb. 1986. Publisher: IET Digital Library.

[14] K. Kao and G. Hockham, "Dielectric-fibre surface waveguides for optical frequencies," in *Proceedings of the Institution of Electrical Engineers*, vol. 113, pp. 1151–1158, July 1966. ISSN: 0020-3270, 2053-7891 Issue: 7.

[15] R. I. Laming, W. L. Barnes, L. Reekie, P. R. Morkel, D. N. Payne, and R. S. Vodhanel, "Erbium Doped Fibre Lasers And Amplifiers," (Boston), p. 82, Feb. 1990.

[16] R. J. Mears, L. Reekie, I. M. Jauncey, and D. N. Payne, "Low-noise erbium-doped fibre amplifier operating at 1.54μm," *Electronics Letters*, vol. 23, p. 1026, Jan. 1987. ADS Bibcode: 1987ElL....23.1026M.

[17] G. P. Agrawal, "Fiber-Optic Communication Systems, 4th Edition | Wiley."

[18] T. Mizuno and Y. Miyamoto, "High-capacity dense space division multiplexing transmission," *Optical Fiber Technology*, vol. 35, pp. 108–117, Feb. 2017.

[19] V. Vujicic, *Optical multicarrier sources for spectrally efficient optical networks*. doctoral, Dublin City University, Mar. 2016.

[20] K. Wang, J. Zhang, M. Zhao, W. Zhou, L. Zhao, and J. Yu, "High-Speed PS-PAM8 Transmission in a Four-Lane IM/DD System Using SOA at O-Band for 800G DCI," *IEEE Photonics Technology Letters*, vol. 32, pp. 293–296, Mar. 2020. Conference Name: IEEE Photonics Technology Letters.

[21] I. Kang, "Phase-shift-keying and on-off-keying with improved performances using electroabsorption modulators with interferometric effects," *Optics Express*, vol. 15, pp. 1467–1473, Feb. 2007. Publisher: Optica Publishing Group.

[22] M. Tan, L. Zhang, and S. He, "The Implementation of 16QAM Modulation and Demodulation and Performance Comparison," in *2009 5th International Conference on Wireless Communications, Networking and Mobile Computing*, pp. 1–4, Sept. 2009. ISSN: 2161-9654.

[23] M. Roser, H. Ritchie, and E. Ortiz-Ospina, "Internet," *Our World in Data*, 2015. https://ourworldindata.org/internet.

[24] S. Niu, Y. Song, L. Zhang, Y. Chen, L. Liang, Y. Wang, L. Qin, P. Jia, C. Qiu, Y. Lei, Y. Wang, Y. Ning, and L. Wang, "Research Progress of Monolithic Integrated DFB Laser Arrays for Optical Communication," *Crystals*, vol. 12, p. 1006, July 2022. Number: 7 Publisher: Multidisciplinary Digital Publishing Institute.

[25] J. J. Xu, L. S. Han, L. P. Hou, S. Liang, J. H. Marsh, Y. G. Huang, and H. L. Zhu, "EAM modulated DBR laser array for TWDM-PON applications," in *2016 IEEE Photonics Conference (IPC)*, pp. 1–2, Oct. 2016.

[26] P. Ma, A. Liu, F. Dong, M. Wang, and W. Zheng, "Single-mode semiconductor lasers fabricated by standard photolithography for direct modulation," *Optics Express*, vol. 27, pp. 5502–5511, Feb. 2019. Publisher: Optica Publishing Group.

[27] B. Corbett and D. McDonald, "Single longitudinal mode ridge waveguide 1.3µm Fabry-Perot laser by modal perturbation," *Electronics Letters*, vol. 31, pp. 2181–2182, Dec. 1995. Publisher: IET Digital Library.

[28] J. Donegan, Q. Lu, and W.-H. Guo, "Discretely Tunable Semiconductor Lasers Suitable for Photonic Integration," 2009. Accepted: 2009-09-21T15:14:41Z.

[29] A. Abdullaev, Q. Lu, W. Guo, M. J. Wallace, M. Nawrocka, F. Bello, A. Benson, J. O'Callaghan, and J. F. Donegan, "Improved performance of tunable single-mode laser array based on high-order slotted surface grating," *Optics Express*, vol. 23, pp. 12072–12078, May 2015.

[30] J. J. Lee, H. S. Kang, and J. S. Koh, "Prediction of TEC power consumption for cooled laser diode module," in *The 17th Annual Meeting of the IEEELasers and Electro-Optics Society, 2004. LEOS 2004.*, vol. 2, pp. 657–658 Vol.2, Nov. 2004.

[31] J. Gao, X. Han, X. Lei, and Y. Yu, "TEC power consumption in laser array packaging," *Optical and Quantum Electronics*, vol. 49, p. 139, Mar. 2017.

[32] S. P. Sim, "The reliability of laser diodes and laser transmitter modules," *Microelectronics Reliability*, vol. 33, pp. 1011–1030, May 1993.

[33] G. Jain, M. J. Wallace, R. McKenna, K. Brazel, F. Bello, Q. Lu, W. Guo, and J. F. Donegan, "Design Optimization for Semiconductor Lasers With High-Order Surface Gratings Having Multiple Periods," *Journal of Lightwave Technology*, vol. 36, pp. 5121–5129, Nov. 2018.

[34] M. Nawrocka, *Design and characterization of widely tunable semiconductor lasers based on etched slots*. thesis, Trinity College (Dublin, Ireland). School of Physics, 2015. Accepted: 2017-06-27T09:46:21Z.

[35] M. J. Wallace, R. O. Meehan, R. Enright, F. Bello, D. McCloskey, B. Barabadi, E. N. Wang, and J. F. Donegan, "Athermal operation of multi-section slotted tunable lasers," *Optics Express*, vol. 25, pp. 14414–14426, June 2017.

[36] M. J. Wallace, *Characterization, Simulation and Optimization of Surface Etched Slotted Tunable Laser Diodes*. Thesis, Trinity College Dublin. School of Physics. Discipline of Physics, 2018. Accepted: 2018-10-25T09:31:28Z.

[37] G. Jain, M. J. Wallace, M. D. G. Pascual, R. McKenna, F. Smyth, J. Braddell, P. M. Anandarajah, and J. F. Donegan, "Athermal Operation of Multi-Section PIC," in *2019 Conference on Lasers and Electro-Optics (CLEO)*, pp. 1–2, May 2019. ISSN: 2160-8989.

[38] H. Debrégeas, R. Borkowski, R. Bonk, R. Brenot, J.-G. Provost, S. Barbet, and T. Pfeiffer, "TWDM-PON Burst Mode Lasers With Reduced Thermal Frequency Shift," *Journal of Lightwave Technology*, vol. 36, pp. 128–134, Jan. 2018. Publisher: IEEE.

[39] S. Y. Siew, B. Li, F. Gao, H. Y. Zheng, W. Zhang, P. Guo, S. W. Xie, A. Song, B. Dong, L. W. Luo, C. Li, X. Luo, and G.-Q. Lo, "Review of Silicon Photonics Technology and Platform Development," *Journal of Lightwave Technology*, vol. 39, pp. 4374–4389, July 2021. Publisher: IEEE.

[40] L. A. Coldren, S. W. Corzine, and M. L. Mašanović, *Diode Lasers and Photonic Integrated Circuits*. 2012.

[41] A. R. Adams, "Strained-Layer Quantum-Well Lasers," *IEEE Journal of Selected Topics in Quantum Electronics*, vol. 17, pp. 1364–1373, Sept. 2011. Conference Name: IEEE Journal of Selected Topics in Quantum Electronics.

[42] G. Thompson and P. Kirkby, "(GaAl)As lasers with a heterostructure for optical confinement and additional heterojunctions for extreme carrier confinement," *IEEE Journal of Quantum Electronics*, vol. 9, pp. 311–318, Feb. 1973. Conference Name: IEEE Journal of Quantum Electronics.

[43] J. Buus, M. C. Amann, and D. J. Blumenthal, *Tunable laser diodes and related optical sources, second edition*. 2005.

[44] B. Bennett, R. Soref, and J. Del Alamo, "Carrier-induced change in refractive index of InP, GaAs and InGaAsP," *IEEE Journal of Quantum Electronics*, vol. 26, pp. 113–122, Jan. 1990. Conference Name: IEEE Journal of Quantum Electronics.

[45] M. Pantouvaki, C. C. Renaud, P. Cannard, M. J. Robertson, R. Gwilliam, and A. J. Seeds, "Fast Tuneable InGaAsP DBR Laser Using Quantum-Confined Stark-Effect-Induced Refractive Index Change," *IEEE Journal of Selected Topics in Quantum Electronics*, vol. 13, no. 5, p. 1112, 2007.

[46] J. E. Zucker, I. Bar-Joseph, B. I. Miller, U. Koren, and D. S. Chemla, "Quaternary quantum wells for electro-optic intensity and phase modulation at 1.3 and 1.55 μm," *Applied Physics Letters*, vol. 54, pp. 10–12, Jan. 1989. Publisher: American Institute of Physics.

[47] N. Cherroret, A. Chakravarty, and A. Kar, "Temperature-dependent refractive index of semiconductors," *Journal of Materials Science*, vol. 43, pp. 1795–1801, Mar. 2008.

[48] X. Han, J. Gao, H. Wang, and Y. Yu, "Thermal analysis of an SOA integrated in SG-DBR laser module," in *2015 International Conference on Numerical Simulation of Optoelectronic Devices (NUSOD)*, pp. 107–108, Sept. 2015. ISSN: 2158-3242.

[49] L. D. Westbrook, A. W. Nelson, P. J. Fiddyment, and J. V. Collins, "Monolithic 1.5 μm hybrid DFB/DBR lasers with 5 nm tuning range," *Electronics Letters*, vol. 20, pp. 957–959, Nov. 1984. Publisher: IET Digital Library.

[50] S. Srinivasan, A. W. Fang, D. Liang, J. Peters, B. Kaye, and J. E. Bowers, "Design of phase-shifted hybrid silicon distributed feedback lasers," *Optics Express*, vol. 19, pp. 9255–9261, May 2011.

[51] R. Lammert, J. Hughes, S. Roh, M. Osowski, A. Jones, and J. Coleman, "Low-threshold narrow-linewidth InGaAs-GaAs ridge-waveguide DBR lasers with first-order surface gratings," *IEEE Photonics Technology Letters*, vol. 9, pp. 149–151, Feb. 1997. Conference Name: IEEE Photonics Technology Letters.

[52] P. Bienstman, *Rigorous and efficient modelling of wavelenght scale photonic components / Peter Bienstman.* dissertation, Ghent University, 2001.

[53] Q. Y. Lu, W. H. Guo, R. Phelan, D. Byrne, J. F. Donegan, P. Lambkin, and B. Corbett, "Analysis of Slot Characteristics in Slotted Single-Mode Semiconductor Lasers Using the 2-D Scattering Matrix Method," *IEEE Photonics Technology Letters*, vol. 18, pp. 2605–2607, Dec. 2006.

[54] N. Kumazaki, Y. Takagi, M. Ishihara, K. Kasahara, A. Sugiyama, N. Akikusa, and T. Edamura, "Detuning characteristics of the linewidth enhancement factor of a midinfrared quantum cascade laser," *Applied Physics Letters*, vol. 92, p. 121104, Mar. 2008. Publisher: American Institute of Physics.

[55] Y. Nishimoto, H. Yagi, K. Miura, D. Plumwongrot, K. Ohira, T. Maruyama, and S. Arai, "High T0 Operation of 1590 nm

GaInAsP/InP Quantum-Wire Distributed Feedback Lasers by Bragg Wavelength Detuning," *Japanese Journal of Applied Physics*, vol. 46, p. L411, Apr. 2007.

[56] F. Xie, C. Caneau, H. P. Leblanc, S. Coleman, M.-T. Ho, C. A. Page, L. C. Hughes, and C.-E. Zah, "Impact of Wavelength Detuning on the Performance of Mid-IR Distributed Feedback Quantum Cascade Lasers," *IEEE Journal of Selected Topics in Quantum Electronics*, vol. 19, pp. 1200508–1200508, July 2013.

[57] ITU-T, "ITU-T Recommendation G.989.1 40-Gigabit-capable passive optical networks (NG-PON2): General requirements," *Itu-T G-Series Recommendations*, 2013.

[58] D. Mickus, G. Jain, S. Naimi, R. McKenna, C. Murphy, and J. F. Donegan, "Athermal Operation of Multi-Section Surface Grating Lasers for Applications Including Burst-Mode for TWDM-PONs," in *2020 Conference on Lasers and Electro-Optics (CLEO)*, pp. 1–2, May 2020. ISSN: 2160-8989.

[59] R. McKenna, D. Mickus, S. Naimi, C. Murphy, M. McDermott, S. Corbett, D. McCloskey, D. McCloskey, D. McCloskey, D. McCloskey, J. F. Donegan, J. F. Donegan, J. F. Donegan, and J. F. Donegan, "Spatially resolved self-heating and thermal impedance of laser diodes using CCD-TR imaging," *OSA Continuum*, vol. 4, pp. 1271–1281, Apr. 2021.

[60] D. Mickus, R. Mckenna, C. Murphy, and J. F. Donegan, "Wide range thermal and athermal operation of slotted surface grating lasers," *Optics Express*, vol. 29, pp. 16893–16903, May 2021. Publisher: Optica Publishing Group.

[61] T. Paoli, "A new technique for measuring the thermal impedance of junction lasers," *IEEE Journal of Quantum Electronics*, vol. 11, pp. 498–503, July 1975. Conference Name: IEEE Journal of Quantum Electronics.

[62] J. Brown, P. K. Footner, and B. P. Richards, "Failure analysis of plastic encapsulated components—the advantages of IR microscopy*," *Journal of Microscopy*, vol. 148, no. 2, pp. 179–194, 1987. _eprint: https://onlinelibrary.wiley.com/doi/pdf/10.1111/j.1365-2818.1987.tb02865.x.

[63] J. Christofferson, K. Maize, Y. Ezzahri, J. Shabani, X. Wang, and A. Shakouri, "Microscale and Nanoscale Thermal Characterization Techniques," *Journal of Electronic Packaging*, vol. 130, Nov. 2008.

[64] S. Wang, C. Xu, F. Duan, B. Wen, S. M. S. Rassel, M. C. Tam, Z. Wasilewski, L. Wei, and D. Ban, "Thermal dynamic imaging of mid-infrared quantum cascade lasers with high temporal–spatial resolution," *Journal of Applied Physics*, vol. 128, p. 083106, Aug. 2020. Publisher: American Institute of Physics.

[65] D. Pierścińska, K. Pierściński, M. Morawiec, P. Karbownik, P. Gutowski, and M. Bugajski, "CCD thermoreflectance spectroscopy as a tool for thermal characterization of quantum cascade lasers," *Semiconductor Science and Technology*, vol. 31, p. 115006, Sept. 2016. Publisher: IOP Publishing.

[66] D. Pierścińska, "Thermoreflectance spectroscopy—Analysis of thermal processes in semiconductor lasers," *Journal of Physics D: Applied Physics*, vol. 51, p. 013001, Nov. 2017. Publisher: IOP Publishing.

[67] I. Mathews, A. Abdullaev, S. Lei, R. Enright, M. J. Wallace, and J. F. Donegan, "Reducing thermal crosstalk in ten-channel tunable slotted-laser arrays," *Optics Express*, vol. 23, pp. 23380–23393, Sept. 2015. Publisher: Optical Society of America.

[68] H. Shalom, A. Zadok, M. Tur, P. Legg, W. Cornwell, and I. Andonovic, "On the various time constants of wavelength changes of a DFB laser under direct modulation," *IEEE Journal of Quantum Electronics*, vol. 34, pp. 1816–1822, Oct. 1998. Conference Name: IEEE Journal of Quantum Electronics.

[69] V. Houtsma, D. v. Veen, S. Porto, S. Porto, N. Basavanhally, C. Bolle, and H. Schmuck, "Investigation of 100G (4x25G) NG-PON2 Upgrade using a Burst Mode Laser based on a Multi-Electrode Laser to enable 100 GHz Wavelength Grid," in *Optical Fiber Communication Conference (2018), paper M1B.3*, p. M1B.3, Optica Publishing Group, Mar. 2018.

[70] W. Poehlmann, D. van Veen, R. Farah, T. Pfeiffer, and P. Vetter, "Wavelength drift of burst-mode DML for TWDM-PON [invited]," *Journal of Optical Communications and Networking*, vol. 7, pp. A44–A51, Jan. 2015. Conference Name: Journal of Optical Communications and Networking.

[71] T. Kawanaka, T. Ashida, S. Yoshima, M. Noda, and K. Motoshima, "Experimental Investigation into Burst-Mode Wavelength Drift of a Mass-Produced 10 Gbit/s EML for TWDM-PON," in *2017 European Conference on Optical Communication (ECOC)*, pp. 1–3, Sept. 2017.

[72] D. van Veen, W. Pöhlmann, B. Farah, T. Pfeiffer, and P. Vetter, "Measurement and mitigation of wavelength drift due to self-heating of tunable burst-mode DML for TWDM-PON," in *OFC 2014*, pp. 1–3, Mar. 2014.

[73] G. Simon, F. Saliou, P. Chanclou, L. Anet Neto, and D. Erasme, "Experimental Demonstration of Low Cost Wavelength Drift Mitigation for TWDM Systems," in *ECOC 2016; 42nd European Conference on Optical Communication*, pp. 1–3, Sept. 2016.

[74] R. Borkowski, W. Poehlmann, and T. Pfeiffer, "TWDM PON Preamble Engineering for Burst-Mode Frequency Drift Reduction Through Mitigation of a DFB Turn-On Blue Shift," in *2017 European Conference on Optical Communication (ECOC)*, pp. 1–3, Sept. 2017.

[75] G. Simon, F. Saliou, P. Chanclou, B. L. Guyader, L. Guillo, J. Konopacki, F. Bourgart, and D. Erasme, "Focus on Time-Dependent Wavelength Drift of DMLs Under Burst-Mode Operation for NG-

PON2," *Journal of Lightwave Technology*, vol. 34, pp. 3148–3154, July 2016. Conference Name: Journal of Lightwave Technology.

[76] A. Sharma, M. N. Hammad, A. Kaszubowska-Anandarajah, G. Jain, M. Wallace, J. Braddell, F. Smyth, and P. M. Anandarajah, "A six-section photonic integrated transmitter with chirp control for transmission reach extension," in *2021 27th International Semiconductor Laser Conference (ISLC)*, pp. 1–2, Oct. 2021. ISSN: 1947-6981.

[77] W. Poehlmann, R. Bonk, H. Schmuck, and T. Pfeiffer, "Cross-talk analysis & mitigation for TWDM-PON upstream path," in *2014 The European Conference on Optical Communication (ECOC)*, pp. 1–3, Sept. 2014. ISSN: 1550-381X.

[78] S. Yoo, J. K. Lee, and K. Kim, "Suppression of thermal wavelength drift in widely tunable DS-DBR laser for fast channel-to-channel switching," *Optics Express*, vol. 25, pp. 30406–30417, Nov. 2017. Publisher: Optical Society of America.

[79] K. Taguchi, K. Asaka, S. Kimura, K.-I. Suzuki, and A. Otaka, "Reverse bias voltage controlled burst-mode booster SOA in λ-tunable ONU transmitter for high-split-number TWDM-PON," *Journal of Optical Communications and Networking*, vol. 10, pp. 431–439, Apr. 2018. Conference Name: Journal of Optical Communications and Networking.

[80] M. Farzaneh, K. Maize, D. Lüerßen, J. A. Summers, P. M. Mayer, P. E. Raad, K. P. Pipe, A. Shakouri, R. J. Ram, and J. A. Hudgings, "CCD-based thermoreflectance microscopy: principles and applications," *Journal of Physics D: Applied Physics*, vol. 42, p. 143001, June 2009.

[81] K. Maize, J. Christofferson, and A. Shakouri, "Transient Thermal Imaging Using Thermoreflectance," in *2008 Twenty-fourth Annual IEEE Semiconductor Thermal Measurement and Management Symposium*, pp. 55–58, Mar. 2008. ISSN: 1065-2221.

[82] S. Wang, C. Xu, F. Duan, B. Wen, S. M. S. Rassel, Z. Wasilewski, L. Wei, and D. Ban, "Time-Resolved Thermoreflectance Imaging for

Mid-Infrared Quantum Cascade Laser," in *2020 Conference on Lasers and Electro-Optics (CLEO)*, pp. 1–2, May 2020. ISSN: 2160-8989.

[83] M. Farzaneh, D. Luerssen, and J. A. Hudgings, "Thermal profiling of photonic integrated circuits by thermoreflectance microscopy," in *2006 Conference on Lasers and Electro-Optics and 2006 Quantum Electronics and Laser Science Conference*, pp. 1–2, May 2006. ISSN: 2160-9004.

[84] J. A. Summers, M. Farzaneh, R. J. Ram, and J. A. Hudgings, "Thermal and Optical Characterization of Photonic Integrated Circuits by Thermoreflectance Microscopy," *IEEE Journal of Quantum Electronics*, vol. 46, pp. 3–10, Jan. 2010. Conference Name: IEEE Journal of Quantum Electronics.

[85] K. J. Greenberg, J. A. Summers, M. Farzaneh, and J. A. Hudgings, "Spatially-resolved thermal coupling in VCSEL arrays using thermoreflectance microscopy," in *2008 Conference on Lasers and Electro-Optics and 2008 Conference on Quantum Electronics and Laser Science*, pp. 1–2, May 2008.

[86] R. McKenna, S. Corbett, S. T. Naimi, D. Mickus, D. McCloskey, and J. F. Donegan, "Thermoreflectance Imaging of Semiconductor Lasers With a Numerical Thermal Model," *IEEE Journal of Selected Topics in Quantum Electronics*, vol. 28, pp. 1–6, Jan. 2022. Conference Name: IEEE Journal of Selected Topics in Quantum Electronics.

[87] F. Rossi, "Fundamentals of Semiconductor Materials and Devices," in *Theory of Semiconductor Quantum Devices: Microscopic Modeling and Simulation Strategies* (F. Rossi, ed.), NanoScience and Technology, pp. 1–51, Berlin, Heidelberg: Springer, 2011.

[88] M. Davis and R. O'Dowd, "A new large-signal dynamic model for multielectrode DFB lasers based on the transfer matrix method," *IEEE Photonics Technology Letters*, vol. 4, pp. 838–840, Aug. 1992. Conference Name: IEEE Photonics Technology Letters.

[89] Y. Matsui, W. Li, H. Roberts, H. Bulthuis, H. Deng, L. Lin, and C. Roxlo, "Transceiver for NG-PON2: Wavelength tunablity for burst mode TWDM and point-to-point WDM," in *2016 Optical Fiber Communications Conference and Exhibition (OFC)*, pp. 1–3, Mar. 2016.

[90] G. Jain, D. Gutierrez-Pascual, S. O'Duill, P. M. Anandarajah, A. Kaszubowska, F. Smyth, L. P. Barry, J. F. Donegan, and J. Braddell, "Directly modulated photonic integrated multi-section laser for next generation TWDM access networks," in *45th European Conference on Optical Communication (ECOC 2019)*, pp. 1–4, Sept. 2019.

[91] A. Gumaste and T. Antony, "DWDM Network Designs and Engineering Solutions," Dec. 2002.